

**Kinematic Models of Interseismic Deformation  
in Southern California**

by

Brendan J. Meade

B.A. Earth and Planetary Sciences and History of Science, Medicine and Technology  
Johns Hopkins University, 1998

Submitted to the Department of Earth, Atmospheric and Planetary Sciences  
in partial fulfillment of the requirements for the degree of

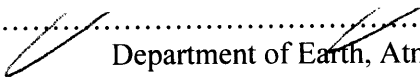
Doctor of Philosophy

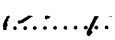
at the

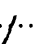
MASSACHUSETTS INSTITUTE OF TECHNOLOGY

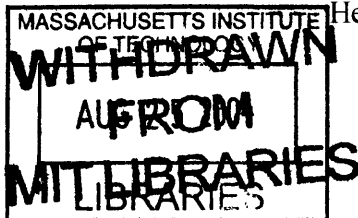
FEBRUARY 2004

© Massachusetts Institute of Technology 2004. All rights reserved.

Signature of Author.....  
Department of Earth, Atmospheric and Planetary Sciences  
January 9, 2004

Certified by.....  
Bradford H. Hager  
Cecil and Ida Green Professor of Earth Sciences  
Thesis Supervisor

Accepted by.....  
Maria T. Zuber  
E. A. Griswold Professor of Geophysics  
Head, Department of Earth, Atmospheric and Planetary Sciences



LINDGREN



## Kinematic Models of Interseismic Deformation in Southern California

by

Brendan Meade

Submitted to the Department of Earth, Atmospheric and Planetary Sciences  
on January 9, 2004 in partial fulfillment of the  
requirements for the degree of  
Doctor of Philosophy

### Abstract

We develop a framework for interpreting geodetic measurements of interseismic deformation and geologic slip rate estimates in terms of block motions. This method accounts for the effects of block rotations and interseismic strain accumulation from active faults. We find that the San Andreas Fault slips close to its Holocene rate in the Carrizo Plain ( $35.6 \pm 0.5$  mm/yr) but is five times slower near San Bernadino ( $6.6 \pm 2.7$  mm/yr). Thrust faults underneath Los Angeles, the Ventura Basin, and the San Gabriel range front all exhibit active shortening from 0.5 to 13.5 mm/yr. We suggest that differences between paleoseismic and block model slip rate estimates may be explained by changes in fault slip rates through the Holocene.

The viscoelastic rheology of the non-brittle upper lithosphere may give rise to time dependent surface deformation through the seismic cycle. We extend a classic theory from periodic to temporally clustered earthquakes by superposing several out of phase earthquake cycles. This new model displays a much wider range of behaviors than does the periodic earthquake cycle model and provides a mechanism to explain apparent discrepancies between geologic and geodetic slip rate estimates.

The potential for large earthquakes in an active fault system is determined by the balance between coseismic moment release and interseismic moment accumulation. We identify regions of local moment deficit in Southern California by comparing historical earthquake catalogs with the fault slip rate catalogs derived from both geologic and geodetic data. Large moment release deficits are localized in the northern Mojave Desert, San Jacinto fault, San Andreas fault, and the greater Los Angeles area. We estimate the minimum size earthquake sources ( $M > 7$ ) required to relieve these deficits.

Thesis supervisor: Bradford H. Hager  
Title: Cecil and Ida Green Professor of Earth Science



### **Acknowledgements**

Brad Hager has been a terrific advisor and is a model of scientific creativity and rigor. He unselfishly shared many great scientific ideas and gave me the opportunity to pursue interesting new projects. I hope that I have adequately represented his tremendous contributions to this present work and my education.

Tom Herring, Leigh Royden, and John Shaw all agreed to be on my thesis committee and provided a number of constructive comments and helpful suggestions. I thank Kelin Whipple for introducing me to geomorphology. Simon McClusky kept me entertained at all times, and answered countless questions about geodesy and computing. Rob Reilinger opened my eyes to the coupling between academic tectonics and earthquake hazard research. I thank Bob King for his patience and kindness as he helped me to learn about geodetic data. Tom Herring introduced me to inverse methods and instilled in me a deep appreciation for the power of statistical analysis.

Meghan Miller and Roland Burgmann were wonderful officemates during their sabbatical years at MIT. Over the last four years, Eric Hetland shared an office with me, taught me much about the natural world, and always kept me laughing. Terri McCloon, Jane Shapiro, Linda Menke, Clint Conrad, Katy Quinn, Jeff McGuire, Liangjun Chen, An Nguyen, Shawn Lawrence, and Monica Aponte, have been sources of warm conversation and stimulating ideas.

I thank the Southern California Earthquake Center, National Science Foundation, National Aeronautic and Space Administration, and the Department of Earth, Atmospheric and Planetary Sciences Grayce B. Kerr Fellowship for financial support.



## Table of contents

<b>Introduction</b> .....	<b>10</b>
<b>Chapter 1</b> .....	<b>17</b>
<b>Block Models of the Present Day Deformation of Southern California Constrained by Geodetic Measurements</b> .....	<b>17</b>
1. Introduction.....	18
2. Relative deformation due to small and large earthquakes .....	23
3. Simple models of the earthquake cycle .....	25
4. Block modeling.....	30
5. Geodetic data .....	38
6. Southern California block geometry.....	43
7. Results and Interpretation .....	47
7.1. Locking depth variations.....	47
7.2. Fit to data .....	51
7.3. Pacific-North America Euler Pole .....	54
7.4. Estimated slip rates .....	55
7.5. The San Andreas Fault system.....	59
7.6. Shortening across Transverse Ranges and Los Angeles Basin.....	60
7.7. Eastern California Shear Zone .....	63
8. Discussion .....	65
9. Conclusions.....	73
Appendix A. Elastic models of viscoelastic data.....	76
Appendix B: Observed velocities .....	80
Appendix C. Southern California block geometry .....	91
<b>Chapter 2</b> .....	<b>103</b>
<b>Viscoelastic Deformation for a Clustered Earthquake Cycle</b> .....	<b>103</b>
1. Introduction.....	103
2. An idealized clustered earthquake cycle.....	105
3. Variations with $\tau_0$ and $\Delta T / T$ .....	111
4. Discussion .....	113
5. Conclusions.....	117

<b>Chapter 3 .....</b>	<b>121</b>
<b>Spatial Localization of Moment Deficits in Southern California .....</b>	<b>121</b>
1. Introduction.....	121
2. Moment accumulation, release and balance .....	122
3. Earthquake catalogs .....	124
4. Fault slip rate catalogs .....	127
5. Regional moment balance.....	129
Reference .....	132
6. Spatial localization of moment deficit .....	135
7. Minimum earthquake source estimates.....	144
7.1. Source estimation method.....	144
7.2. Southern San Andreas and San Jacinto Faults.....	149
7.3. Northern Mojave.....	152
7.4. Los Angeles .....	154
8. Discussion.....	155
9. Conclusions.....	157
<b>Appendix A.....</b>	<b>165</b>
<b>Software philosophy, design and some interesting algorithms.....</b>	<b>165</b>
1. Introduction.....	165
2. Lineage and early work.....	166
3. Philosophy.....	167
4. Block model software structure .....	169
5. Some interesting algorithms .....	169
5.1. Block closure and labeling.....	170
5.2. Fault labeling and east - west determination.....	171
5.3. Station labeling .....	171
5.4. Okada with an automatic optimal map projection .....	172





## **Introduction**

The goal of this work is a quantitative description of the distribution of deformation across the Southern California fault system in order to estimate present day slip rates that are compatible with GPS observations of interseismic deformation. If most deformation occurs along faults, then slip rates provide a kinematic description of plate boundary zone deformation and provide the basis for both earthquake cycle and tectonic models. Slip rates estimated from geodetic measurements are not necessarily the same as long-term geologically determined slip rates. By comparing geodetic and geologic slip rate estimates, we can assess whether or not a fault system is at steady state and, if not, estimate the time scale over which slip rates evolve.

Over the last two decades, geodetic monitoring techniques, especially using the Global Positioning System (GPS), have matured to allow the measurement of interseismic deformation with a precision better than 1 mm/yr. In addition to increased precision, the number of campaign and continuous stations in regional networks has grown from 10's to 100's. With these rich data sets, we can pursue geometrically and temporally complex models of fault slip rates, seismic hazard potential and crust/upper mantle rheology.

The Southern California Earthquake Center (SCEC) Crustal Motion Map (CMM) version 3.0<sup>1</sup> is the largest source of interseismic velocity estimates (~800) in Southern California. We augment this data set with velocities in the Eastern California Shear Zone from *McClusky et al.* (2001), the Pacific Plate from *Steblov et al.* (2003), and the northern Sierra Block (BARD network<sup>2</sup>). Figure 1 shows the combined velocity field in a mean Southern California reference frame. The most striking feature of the GPS velocity field is the ~50 mm/yr of relative motion between the North American (top) and Pacific Plates (bottom).

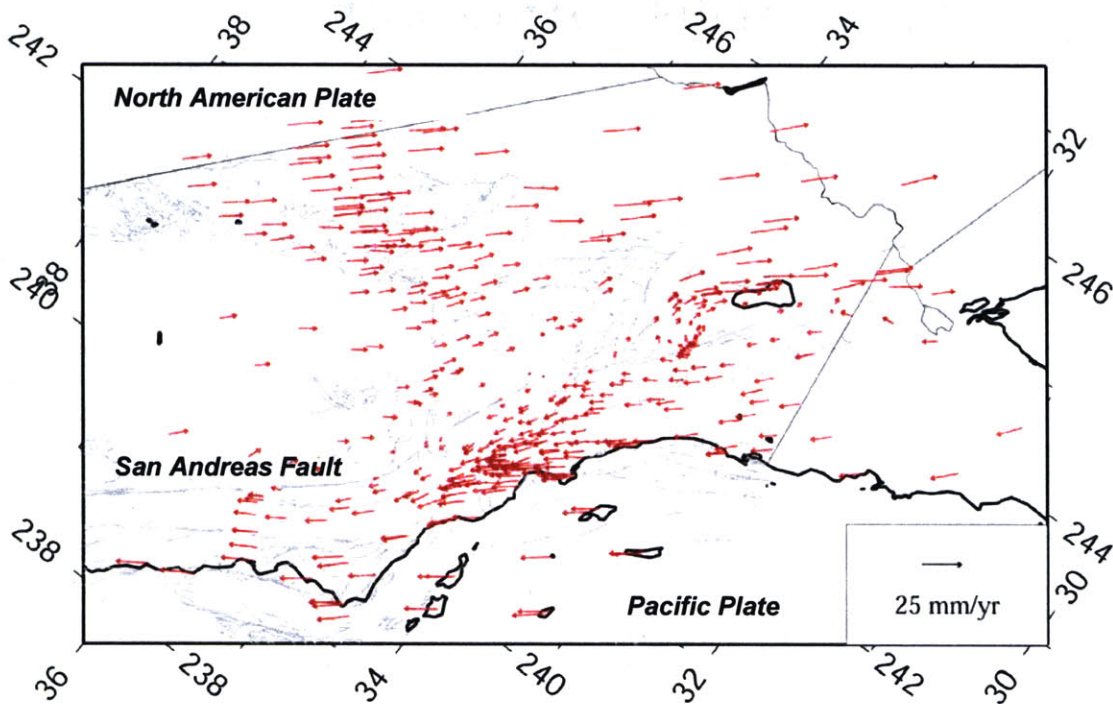


**Figure 1.** Interseismic GPS velocities in Southern California.

<sup>1</sup> <http://epicenter.usc.edu/cmm3>

<sup>2</sup> <http://quake.geo.berkeley.edu/bard/bard.html>

The velocity transition between the two plates is not a simple step function across a single transform structure, but instead varies smoothly across the ~200 km wide fault system. The largest velocity gradients are associated with the San Andreas fault, which strikes from northwest to southeast, and accommodates approximately 60% of the relative plate motion. Interseismic deformation reflects the effects of both plate (block) motion and seismic cycle processes. Fault creep, viscoelastic relaxation of seismically induced stresses and interseismic strain accumulation are the primary near-fault processes. Elastic dislocation theory is typically used to describe steady state interseismic strain accumulation and can be considered a high viscosity approximation of a viscoelastic seismic cycle model. Because the width of an interseismic velocity gradient is a function not only of the slip rate, but also of the fault geometry, we can estimate apparent locking depths. These may represent true locking depths, proxies for complex elastic structure in the upper crust, or long-term postseismic viscoelastic effects. Any model of interseismic deformation in an active plate boundary zone must account for these effects.

In addition to contributing to interseismic GPS velocities, elastic strain accumulation stores the energy that is later released by earthquakes. The potential for large earthquakes is typically quantified by one of three methods: 1) estimating the area of potential rupture sources, 2) extrapolating Gutenberg-Richter statistics to large magnitude events, and 3) comparing the rates of moment accumulation and release. This last method is an approximate statement of conservation of energy for seismic cycle processes. An accurate fault slip rate catalog compatible with geodetic observations of

interseismic deformation provides the basis for calculating the rate at which moment is accumulating over the last 5-15 years. In contrast, geologic slip rate catalogs tend to estimate slip rates over 5000 to 5 million year intervals. For the purposes of seismic hazard assessment, a geodetic slip rate catalog is preferable to a geologic catalog in the sense that it constraints information about the strain we can observe accumulating today. Moment release rates can be estimated using epicenter and magnitude information from historical earthquake catalogs. If coseismic deformation has not kept up with interseismic strain accumulation, there is a moment deficit that may be relieved by future earthquakes. With a moment accumulation model that is consistent with fault system geometry and reasonably accurate historical epicenter estimates, we can localize moment deficits along specific fault zones.

Previous attempts to integrate geodetic data into seismic hazard assessment have been based on simplified models of regional strain that do not reflect the geometry of potential earthquake sources or seismic cycle processes. The observed surface strain is not necessarily an indicator of interseismic strain accumulation. For example, high strain rates are observed around the creeping section of the San Andreas Fault north of Parkfield. However, this section is not a potential source of large earthquakes as there is no significant interseismic strain accumulation. This highlights the necessity of modeling observed interseismic velocities with a model that reflects the geometry of the fault system and accounts for interseismic strain accumulation.

This thesis is organized into three chapters and an appendix. Chapter 1 presents the block-modeling framework and applies it to Southern California using interseismic

GPS measurements as constraints. This study focuses on estimating slip rates of major faults and includes a comparative analysis of geodetically and geologically determined slip rates, with an emphasis on the branching aspects of the southern San Andreas fault system. We find that the strike-slip rate on the San Andreas fault varies by a factor of four. This result requires us to reconsider the long-term tectonic role of, and the seismic hazard potential associated with the southern SAF. In chapter 2, we develop a new model for interseismic deformation through a clustered earthquake cycle by extending the viscoelastic models of *Savage and Prescott (1978)* and *Savage (2000)*. A clustered earthquake cycle is defined and interseismic velocities are predicted. Using previous paleoseismic and geodetic studies, we consider applications in Southern California and the Wasatch Range, Utah. Chapter 3 is devoted to assessing seismic hazard potential in Southern California using moment balance principles. This work reexamines the basic and critical question: To what extent is the moment release associated with large earthquakes balanced by the moment accumulation due to interseismic strain accumulation? We find that there is substantial evidence for a 50% moment deficit at the regional scale and that it is localized in three regions: the southern San Andreas fault system, the northern Mojave Desert and the greater Los Angeles area. The Appendix provides an overview of the philosophy and design principles that were used to guide the creation of software necessary to perform the calculations detailed in Chapter 1. We also review some of the more interesting geometry management algorithms that allow for the efficient handling of three-dimensional fault geometry on a sphere.

**References**

McClusky, S. C., S. C. Bjornstad, B. H. Hager, R. W. King, B. J. Meade, M. M. Miller, F. C. Monastero, and B. J. Souter, Present Day Kinematics of the Eastern California Shear Zone from a Geodetically Constrained Block Model, *Geophys. Res. Lett.*, 28, 3339 - 3372, 2001.

Savage, J. C., Viscoelastic coupling model for the earthquake cycle driven from below, *J. Geophys. Res.*, 105, 25,525 - 25,532, 2000.

Savage, J. C., and W. H. Prescott, Asthenosphere readjustment and the earthquake cycle, *J. Geophys. Res.*, 83, 3369 - 3376, 1978.

Steblov G. M., M. G. Kogan, R. W. King, C. H. Scholz, R. Bürgmann, D. I. Frolov, Imprint of the North American plate in Siberia revealed by GPS, *Geophys. Res. Lett.*, 30 (18), 1924, doi:10.1029/2003GL017805, 2003.





## Chapter 1

# Block Models of the Present Day Deformation of Southern California Constrained by Geodetic Measurements<sup>3</sup>

**Abstract.** We estimate present-day slip rates on major active structures in Southern California using block models of the interseismic velocities based on geodetic data, primarily the SCEC 3.0 Crustal Motion Map. The block model approach accounts for elastic coupling between blocks and yields kinematically consistent slip rates. Approximately 69% of the residual velocity magnitudes are smaller than their estimated 1- $\sigma$  values. Formal fault slip rate uncertainties calculated by covariance propagation range from 0.4 to 3.1 mm/yr. The string of faults from Oak Ridge and San Cayetano in the west, running toward the Sierra Madre fault, along the San Gabriel range front to the Cucamonga fault near the San Andreas Fault (SAF), all show high dip slip rates up to 13.5 mm/yr. Just to the southeast of these faults, the Puente Hills Thrust shows  $\sim 2$  mm/yr of shortening. The San Bernadino segment of the SAF has a surprisingly low right lateral slip rate of  $6.6 \pm 0.9$  mm/yr. This low slip rate may account for the long recurrence interval observed in the paleoseismic record there and may act as an impediment to large SAF earthquakes rupturing all the way through the Big Bend. We find a 25 km locking depth for the portion of the SAF that broke during the 1857 Ft. Tejon earthquake. We propose that the Eastern California Shear Zone may be rapidly evolving and that geodetically estimated slip rates indicate that the Owens Valley and Blackwater faults are currently more active than they have been in the recent geologic past. The success of our model seems to support the steady-state model as a valuable tool to determine fault system kinematics. Its success may support the validity of the assumption of a high viscosity lower crust/upper mantle ( $\eta > 10^{19}$  Pa·s), or simply averaging across earthquakes in different parts of the seismic cycle.

---

<sup>3</sup> This work is being prepared for publication with Brad Hager

## 1. Introduction

Southern California lies at the active plate boundary between the Pacific and North American Plates, where these plates move past each other at approximately 50 mm/yr (e.g., *DeMets et al.* 1990, *DeMets and Dixon*, 1999). The relative motion between the two plates manifests itself primarily through strike slip faulting (*Atwater*, 1970). At the latitude of the Carrizo plain, approximately 70% of the relative motion between the two plates is localized as right lateral motion on the San Andreas Fault (SAF) (e.g., *Minster and Jordan*, 1987, *Sieh and Jahns*, 1984, *Argus and Gordon*, 2001). However, the Southern California fault system (SCFS) consists of a large number of interconnected faults with a wide range of deformation styles (e.g., *Jennings et al.*, 1994). In addition to the significant right lateral motion on the SAF system, the geologic record provides ample evidence for left lateral motion along the Garlock (e.g., *McGill and Sieh*, 1993, *McGill and Rockwell*, 1998), Pinto Mountain (*Jennings*, 1994, *Petersen and Wesnousky*, 1994), and Raymond Hill faults (*Weaver and Dolan*, 2000). The SAF system itself becomes complicated south of the Mojave segment, where the SAF splits away from, and then rejoins the active San Jacinto Fault (SJF) to the west. The Eastern California Shear Zone (ECSZ) splays to the east from the SAF at about the same latitude and accommodates at least 12 mm/yr of right lateral motion (e.g., *Sauber et al.*, 1994). In short, the relative motion between the Pacific and North American Plates is accommodated across the entire SCFS through various faulting styles.

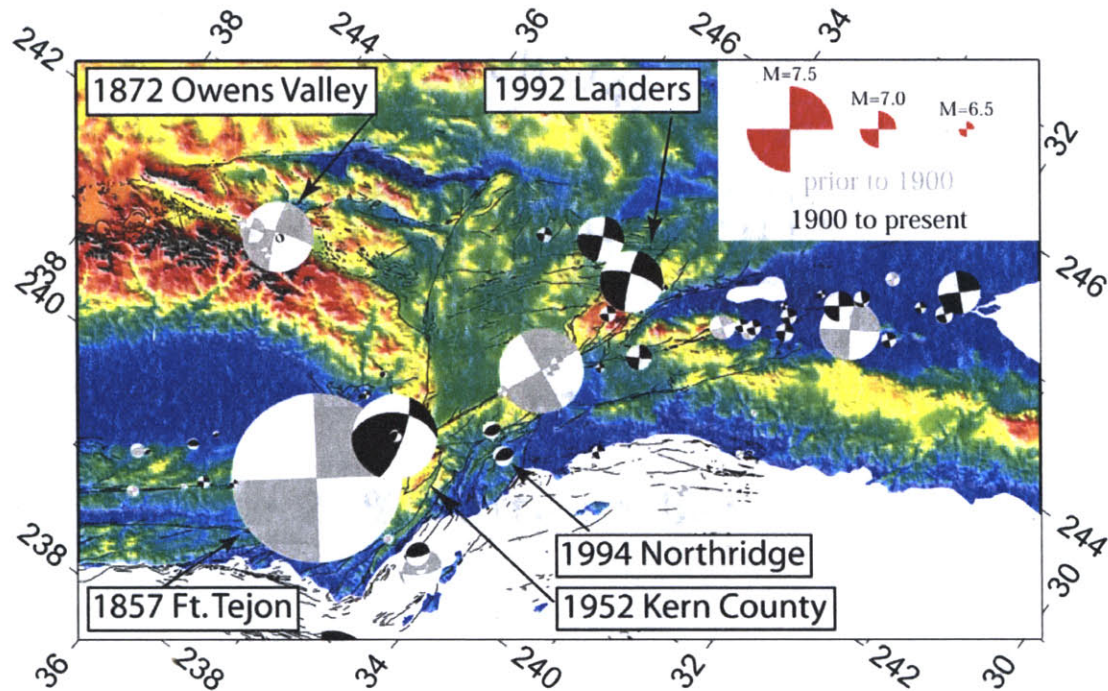


**Figure 1.** Focal mechanisms for large earthquakes (*Kagan, 2002*) in Southern California overlaid on topography (GTOPO30) and fault traces (*Jennings, 1994*). The area of each focal mechanism is proportional to its scalar seismic moment. The darker quadrants are compressional. Focal mechanisms with gray compressional quadrants are those from 1807-1900 and those with black compressional quadrants are from 1900-present. The largest focal mechanism is associated with 1857 Ft. Tejon earthquake along the San Andreas Fault.

Earthquake focal mechanism estimates show a similar variation in orientation and sense of slip (Figure 1.) Some of the largest events (summarized by *Ellsworth, 1990, Stein and Hanks, 1998, Kagan, 2002*) are consistent with right lateral rupture along the SAF and sub-parallel structures (e.g., 1857 Ft. Tejon and 1872 Owens Valley earthquakes). Other focal mechanisms from the instrumental era show significant thrust components (1952 Kern County, 1994 Northridge) associated with compression across the Big Bend of the SAF and shortening in the Ventura Basin. The earthquake focal

mechanisms complement the geologic slip rate data and provide ample evidence that the SCFS is more complicated than a simple strike slip zone.

How is deformation partitioned across the SCFS? If we assume that all deformation on major fault structures is elastic and that earthquakes relieve all of the accumulated strain, then fault slip rates will completely describe the kinematics of the plate boundary zone. Fault slip rates can be estimated from both geologic and geodetic data. Geologic data (offset marker units and initiation dates) provide average slip rates over thousands to millions of years. In contrast, high quality geodetic data (velocities and strain rates) typically only provide information about the last 10-20 years of crustal deformation. Thus, slip rate estimates from geologic and geodetic data are comparable only in the case where the two data sets represent the same time averaged behavior.

There has been great interest in determining the distribution of present day deformation in Southern California in order to provide an estimate of where strain is accumulating most rapidly and, thus, where earthquakes will most likely occur. At the regional scale, *Minster and Jordan* (1987) quantified the “San Andreas deficit” using an early plate motion model. *Bird and Rosenstock* (1984) developed a detailed, hand fit block model of the region in an effort to combine geologically estimated slip rates in a kinematically consistent manner. *Weldon and Humphreys* (1986) carried out a related study, summing the slip rates from a small set of faults and looking for deviations from a path integral constraint to assess slip rate compatibility.

With the development of high quality Very Long Baseline Interferometry (VLBI) and Global Positioning System (GPS) measurements in the late 1980’s (combined with

older EDM data), it became clear that the effects of interseismic strain accumulation should be modeled and that fault slip rates and locking depths could be estimated directly from geodetic data. Using trilateration data, *Cheng et al.* (1987) developed a block model of the northern Transverse Ranges and found a low slip rate on the SAF. *Saucier and Humphreys* (1993) combined geologic slip rate estimates with VLBI velocity estimates to estimate the horizontal velocity field using a thin elastic sheet finite element model. *Feigl et al.* (1993) used an *a priori* deep dislocation model that included the San Andreas, San Jacinto, Elsinore, and Garlock Faults in an attempt to explain early GPS observations. *Bird and Kong* (1994) revisited the block model geometry presented by *Bird and Rosenstock* (1984) and used it to minimize the difference between strains from a thin elastic sheet finite element model and the strains estimated from EDM and VLBI data. A block model approach was used again by *Souter* (1998) to assess the compatibility of geologic estimates of fault slip rates with each other and with observed GPS velocities

Geodetic data have also been used in an attempt to resolve slip rates on a more local scale. *Bennett et al.* (1996) and *Johnson et al.* (1994) estimated the strike slip rate on the southern SAF near the Salton Sea. *Savage and Lisowski* (1998) used a 2D viscoelastic model to estimate not only the slip rate but also the time within the earthquake cycle for the Mojave SAF. The central SAF was studied by *Argus and Gordon* (2001), who attempted to resolve the fault normal and fault parallel components of motion. *Segall* (2002) used a Bayesian framework to combine geologic and geodetic

data to estimate the slip rate, locking depth and recurrence intervals for the Carrizo segment of the SAF.

*Sauber et al.* (1986) and *Savage et al.* (1990) drew attention to the Mojave portion of the ECSZ, a substantial step toward resolving the San Andreas deficit problem (*Minster and Jordan*, 1987). More recently, *Savage et al.* (2001) and *Peltzer et al.* (2001) have provided revised estimates of the slip distribution in the Mojave Desert. The ECSZ north of the Garlock fault has also attracted considerable attention, as authors have attempted to estimate the partitioning of slip across the Owens Valley, Panamint Valley, and Death Valley fault zones (e.g., *Bennett et al.*, 1997, *Hearn et al.*, 1998, *Dixon et al.*, 2000, *Gan et al.*, 2000, *Miller et al.*, 2001, *McClusky et al.*, 2001, *Dixon et al.*, 2003).

Thrust faulting in and around the Transverse Ranges represents a potential source of earthquake hazard near large population centers. *Feigl et al.* (1990) made an effort to quantify the shortening rate in the Santa Maria fold and thrust belt and *Walls et al.* (1998) carried out a similar effort for the Los Angeles basin. Neither of these efforts incorporated modeling of interseismic strain accumulation. *Donnellan et al.* (1993a, 1993b) and *Hager et al.* (1999) used 2D models to estimate shortening rates and seismic hazard across the Ventura Basin. For the LA Basin, both *Argus et al.* (1999) and *Bawden et al.* (2001) reached substantially different conclusions than *Walls et al.* (1998) by including *a priori* models for the strain accumulation associated with the SAF.

The block model approach we present provides a unified framework for combining geologic and geodetic data into a model that includes the effects of block rotation and interseismic strain accumulation. The block model formulation implicitly

enforces a path integral constraint that ensures that the relative plate motion is accommodated everywhere along the length of the plate boundary zone. By estimating slip rates of all faults simultaneously, we arrive at a slip model for the faults affecting the Los Angeles Basin that is free of most of the *a priori* assumptions that have been necessary in previous studies (e.g., *Argus et al.*, 1999, *Bawden et al.*, 2001).

## 2. Relative deformation due to small and large earthquakes

During the time that the geodetic measurements were being made, thousands of earthquakes were recorded. We demonstrate that, except for the effects of a few large earthquakes, most surface deformation is associated with interseismic strain accumulation, not the coseismic strain release associated with small earthquakes. The displacements associated with the Landers (1992), Northridge (1994) and Hector Mine (1999) earthquakes were extensively studied (e.g., *Hudnut et al.*, 1994, *Hudnut et al.*, 1996, *Kaverina et al.*, 2002), but the displacements and moment release from the vast number of smaller earthquakes have received little attention. We show that if strain accumulation is balanced by strain release in great earthquakes, then small earthquakes (e.g., those less than three magnitude units smaller than the maximum size event) do not contribute significantly to an observed interseismic deformation field.

The Gutenberg - Richter magnitude - frequency distribution is given by  $\log_{10} N = a - bM_w$ , where  $N$  is the cumulative number of earthquakes in a year with magnitude greater than  $M_w$ , the moment magnitude, and both  $a$  and  $b$  are constants.

The scalar moment release from each earthquake is given by

$$M_0 = 10^{\alpha(M_0 + \beta)} \quad (1)$$

where  $\alpha = 0.67$ ,  $\beta = 10.7$  (cgs units),  $\mu$  is the shear modulus, and  $A$  is the area of the coseismic rupture (*Hanks and Kanamori, 1979*). The total yearly moment release,  $\Delta$ , due to all earthquakes up to magnitude  $M_w$  is given by the summation over all magnitudes multiplied by the magnitude frequency

$$\Delta(M_w) = \int_0^{M_w} M_0(M'_w)N(M'_w)dM'_w \quad (2)$$

We can compare the moment release due to small events (still in the geodetically observed the velocity field) with the moment accumulation for larger events. All of the earthquakes less than or equal to  $M_w$  account for the fraction of total moment release given by

$$\lambda(M_w, M_w^{\max}) = \frac{\Delta(M_w)}{\Delta(M_w^{\max}) - \Delta(M_w)} = \frac{10^{cM_w}}{10^{cM_w^{\max}} - 10^{cM_w}} \quad (3)$$

where  $M_w^{\max}$  is the largest event size in the region. Other than the size of the largest earthquake, the fraction of deformation,  $\lambda$ , depends only on the constant,  $c$ , which is a function of the slope coefficients from the moment - magnitude ( $\alpha$ ), Gutenberg-Richter



(b), and the size of the largest earthquake. For Southern California, we take the maximum size earthquake to be  $M_w^{\max} = 8.0$ , a little larger than the 1857 Ft. Tejon event. If the largest “little” earthquake remaining in the velocity field is  $M_w = 5.0$ , then this contributes about  $\lambda(5.0, 8.0) = 0.003$  or 3% of the total moment balance. If moment release is balanced by moment accumulation, then all of the faults that are locked and accumulating strain account for 97% of the present day observed deformation. This means that, over the last ten years, there have been a huge number of small earthquake whose effects we have not accounted for, they have not contributed significantly much more moment has been accumulated than has been released. *Ward* (1998) reached much the same conclusion through a similar analysis.

### 3. Simple models of the earthquake cycle

The two components of a simple model of the seismic cycle are the interseismic strain accumulation and the coseismic strain release (e.g., *Reid*, 1910). Interseismic deformation accumulates between large earthquakes; the fault is locked and deformation is driven either from below or from the sides. The basic concepts of interseismic deformation are well illustrated by 2D models that allow us to isolate the effects of rheology.

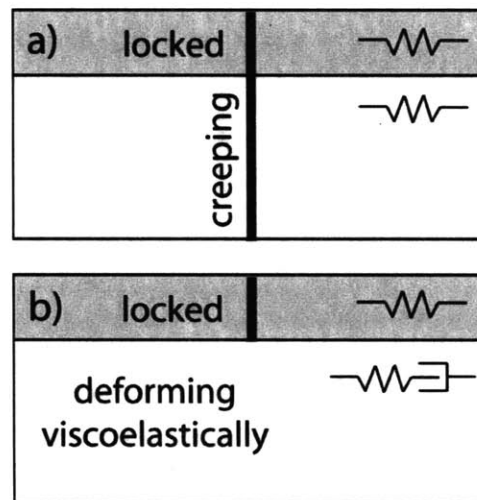


**Figure 2.** Vertical cross sections showing simple layered crustal rheology models. The upper gray layer is elastic (spring element). The dark vertical line in this region is the seismogenic part of the fault zone. A) The elastic rheology was used by *Savage and Burford* (1973) and is used for the block model presented in this paper. During the interseismic part of the seismic cycle, the down-dip extension of the fault (dark vertical line below the seismogenic layer) creeps at a steady rate equal to the geologic rate. B) An elastic layer over a Maxwell viscoelastic layer (spring and dashpot elements in series). This layered rheology was used for the time-dependent seismic cycle models presented in *Savage and Prescott* (1978) and *Savage* (2000).

*Savage and Burford* (1973) proposed an interseismic deformation model for a homogeneous elastic halfspace. In their model, the coseismic layer is locked and a down-dip extension of the fault zone creeps at a steady slip rate equal to the geologic rate (figure 2).

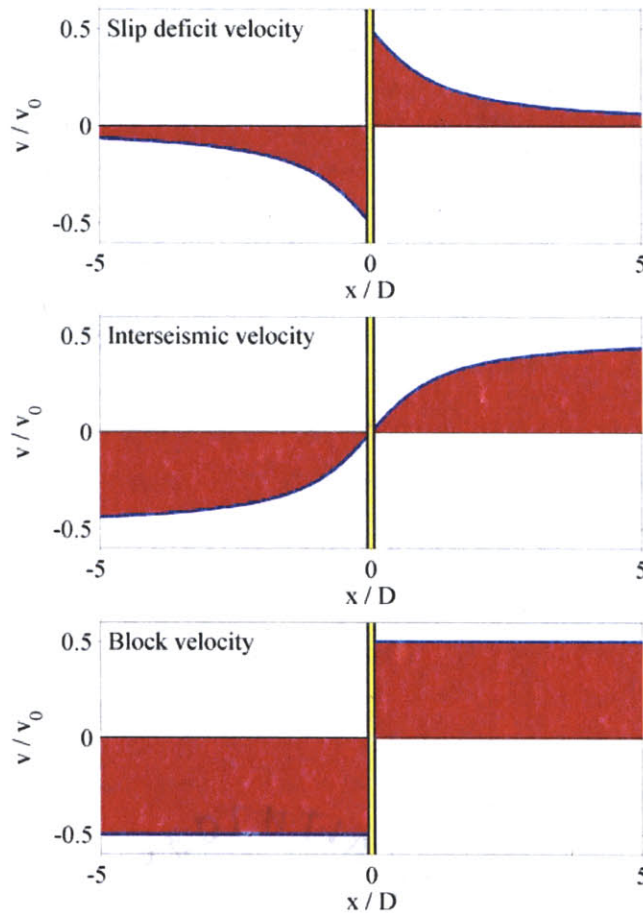


**Figure 3.** Three velocity profiles across an infinitely long fault, after *Savage and Burford (1973)*. The upper panel shows the slip deficit. This is the elastic contribution to the long-term velocity field. The sum of the slip deficit velocity and the interseismic velocity is the long-term block velocity. The striped line in each panel is the fault trace. The shaded areas indicate the areas swept through by the respective velocities. This is the simple case where the blocks on either side of the fault are translating past each other with only strike slip motion on the fault. In this case, the interseismic velocity profile is given by  $v = v_0 \pi^{-1} \tan^{-1}(x/D)$ .

In this model, there is no dependence of the deformation on the shear modulus and the fault parallel velocity profile is given (for a screw dislocation) by  $v = v_0 \pi^{-1} \tan^{-1}(x/D)$ , where  $v_0$  is the deep steady slip rate,  $x$  is the distance from the fault trace, and  $D$  is the

elastic locking depth. The velocity profile is characterized by a smooth transition across the fault zone, in contrast to the coseismic and long-term geologic profiles, both of which are discontinuous at the fault (figure 3). This model has been the basis for many interpretations of geodetically determined velocities and strain rates (e.g., *Savage and Burford, 1973, Bennett et al., 1997*).

A model with a more complex layered rheology is shown in figure 2b. Here a Maxwell viscoelastic layer lies underneath an elastic layer that ruptures coseismically. *Nur and Mavko (1974)* initially developed an approximate solution for a dip slip fault in order to model time dependent velocities in Japan. *Savage and Prescott (1978)* developed an analytic model for an infinitely long, vertical, strike slip fault and *Savage (2000)* restated their solution in a more concise form. In contrast to the steady elastic model, the viscoelastic model depends on the material properties (shear modulus, dynamic viscosity) and the time through the earthquake cycle. The parameter that governs the time evolution is  $\tau_0 = \mu T / 2\eta$ , where  $\mu$  is the shear modulus,  $T$  is the length of the earthquake cycle (recurrence interval) and  $\eta$  is the dynamic viscosity of the viscoelastic layer. Though the explicit description of the time dependence is rather complex, it is straightforward to characterize the velocity profile evolution on the basis of  $\tau_0$ . For large values of  $\tau_0$  ( $\tau_0 > 1$ ) there are significant variations in the velocity profile through the seismic cycle (figure 4). Immediately after an earthquake, the near field velocities are fast relative to the elastic halfspace (steady state) values; just prior to an earthquake, the near field velocities are slower than the steady state value. In all cases, the far field velocity is the same for the elastic and viscoelastic cases. The time

dependent profiles nearly collapse onto the steady state profiles approximately  $2/5^{\text{th}}$  of the way through an earthquake cycle. Recently, *Savage and Lisowski* (1998), *Segall* (2002) and *Dixon et al.* (2003) have used this model to interpret measurements of interseismic deformation in Southern California.

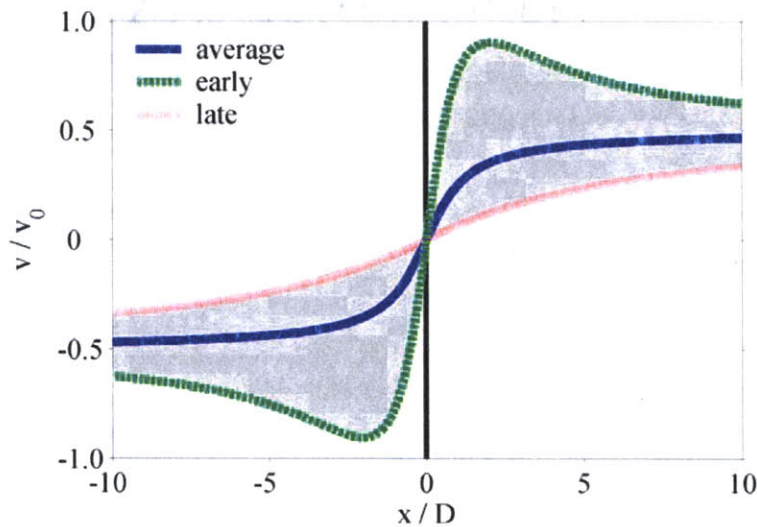


**Figure 4.** Fault parallel velocities at different times in the seismic cycle following *Savage and Prescott* (1978). The shaded region indicates the area swept out through the seismic cycle. The light dashed green, solid blue and finely dashed red curves are the velocity profiles immediately after a model earthquake, an average over the interseismic period, and immediately prior to the next event. The time variation of these curves depends on the parameter  $\tau_0 = \mu T / 2\eta \approx 5$ .

Large values of  $\tau_0$  may be due to either long repeat times or relatively low viscosities. However, for short repeat times ( $T < 300$  years) and large viscosities ( $\eta > 3 \times 10^{20}$ )  $\tau_0$  is small ( $\tau_0 < 0.5$ ). In this case, there is very little variation through the seismic cycle and the Maxwell viscoelastic model is indistinguishable from the elastic model (figure 4). We invoke this high viscosity (low  $\tau_0$ ) limit implicitly, assuming that

the deformation of the viscoelastic Earth is adequately approximated by that of an elastic halfspace model. We evaluate the applicability of this assumption later in this paper.

*Savage* (2000) developed a related model for an elastic layer overlaying a Maxwell viscoelastic channel. The results were qualitatively similar to the semi-infinite viscoelastic halfspace case, although the time-dependant variation becomes more localized around the fault zone, with smaller deviations from steady state.

If viscoelastic effects do contribute to an observed velocity field, they may be mapped into an elastic model as variations in slip rate and locking depth. Early in the earthquake cycle, near-fault velocities are relatively high and map into an elastic model as a fast slip rate and a shallow locking depth. Conversely, late in the earthquake cycle, the elastic interpretation would include a slower slip rate and a deeper locking depth (see appendix A for details). If far-field velocities were available early in the earthquake cycle, then the viscoelastic effect would be quite evident, as the velocity gradient would reverse near the fault zone.

#### **4. Block modeling**

We divide our study region (Southern California) into blocks bounded by faults. To relate block motions and fault slip rates to geodetic observations of interseismic deformation we start with the approach first detailed by *Savage and Burford* (1973). We extend and generalize this formulation to allow for the effects of block rotation on a

sphere, dipping faults, finite length faults, and multiple blocks. For the two-dimensional case, the total block displacement over an earthquake cycle of length  $T$  is defined as the sum of integrated interseismic displacement,  $T\bar{v}_I$ , and coseismic deformation contributions (figure 3),

$$T\bar{v}_B = T\bar{v}_I(\bar{x}_S) + \bar{f}(\bar{d}, \bar{x}_S, \bar{x}_F) \quad (4)$$

where  $\bar{d}$  is the coseismic slip vector,  $\bar{x}_S$  specifies station coordinates, and  $\bar{x}_F$  contains the fault geometry. For an infinitely long strike-slip fault, the coseismic term is given by an arctangent function that depends on the distance from the fault and the elastic locking depth (figure 3). If we divide equation 4 by  $T$  and assume that  $\bar{f}$  is linear in  $\bar{d}$ , then we can pull the earthquake displacement out of the function  $\bar{f}$ . We can then write interseismic velocity as the difference between the block velocity and the yearly coseismic slip deficit (CSD) velocity,

$$\bar{v}_I = \bar{v}_B(\bar{x}_S) - \bar{s}g(\bar{x}_S, \bar{x}_F) = \bar{v}_B(\bar{x}_S) - \bar{v}_{CSD}(\bar{x}_S, \bar{x}_F) \quad (5)$$

The geodetic data set we are modeling can be considered to represent interseismic deformation, primarily showing strain accumulation, with negligible coseismic strain release.

Several studies have extended this argument from a single infinitely long fault to multiple finite faults in a planar formulation (e.g., *Matsu'ura and Jackson, 1986, McCaffrey et al. 1996, Souter, 1998*). We move to a spherical framework where we can directly estimate rotation vectors  $\vec{\Omega} = (\Omega_x, \Omega_y, \Omega_z)$  for each block. *Murray and Segall (2001)* used a similar approach, but ignoring fault-normal motion, for Northern California and the Basin and Range province. Equation 5 gives a general representation of interseismic deformation. We can write both  $\vec{v}_B$  and  $\vec{v}_{CSD}$  in terms of rotation vectors  $\vec{\Omega}$ . The block motion contribution to the interseismic velocity field is straightforward and is given by

$$\vec{v}_B(\vec{x}_S) = \vec{\Omega} \times \vec{x}_S = \mathbf{R}_B(\vec{x}_S)\vec{\Omega} \quad (6)$$

where  $\mathbf{R}_B(\vec{x}_S)$  is a linear cross product operator that is a function of station coordinates,  $\vec{x}_S$ . One of the great advantages of the block motion formulation over the traditional deep slip model is immediately clear from equations 5 and 6. That is, the effects of block rotations on the interseismic velocity field can be included. Even in two dimensions, this may significantly modify the traditional arctangent profile such that the total far field velocity is less than the fault slip rate (e.g., *Meade et al., 2001*).

To calculate the elastic (or coseismic slip deficit) contribution to the velocity field, we use the dislocation solutions presented by *Okada (1985)* for the surface deformation due to an arbitrarily inclined dislocation in a uniform elastic half space. In



order to use these formulas, we project the fault geometry and station positions from spherical to planar geometry. While the spatial distortion due a reasonable conformal projection over an area the size of southern California is <1%, our desire to incorporate far-field velocities (e.g. in the interiors of the Pacific and North American plates) motivated us to take a different approach to the “flattening” problem. Every fault segment is divided into small pieces no longer than 10 km. For each small segment, we want to model the elastic deformation accurately in the immediate vicinity of the fault, where the velocity gradients are largest. To do this we use a local projection for each small fault segment, compute the elastic contribution, and then rotate all of the velocities back into an east, north, up frame. A locally tangent oblique Mercator projection allows us to flatten the geometry in such a way that the fault trace is approximated as a great circle path between its two endpoints. Combining these transformations, we can write the slip deficit velocity as,

$$\vec{v}_{CSD} = \mathbf{R}_{X \rightarrow E}(\vec{x}_S) \mathbf{R}_P(\vec{x}_S, \vec{x}_F) \mathbf{R}_O(\vec{x}_S, \vec{x}_F) \vec{s} \quad (7)$$

where  $\mathbf{R}_{X \rightarrow E}$  transforms XYZ velocities to an ENU (east, north, up) frame,  $\mathbf{R}_P$  projects the station and fault positions into planar space from their spherical coordinates and  $\mathbf{R}_O$  contains the partial derivatives of *Okada's* (1985) elastic Green's functions with respect to slip rate. Most of the matrices ( $\mathbf{R}$ ) are written to emphasize that they are functions of station ( $\vec{x}_S$ ) and/or fault ( $\vec{x}_F$ ) coordinates. The fault slip rates are linearly related to the rotation vectors as well,

$$\bar{s} = \mathbf{R}_F(\bar{x}_F)\mathbf{R}_{\Delta v}(\bar{x}_F)\bar{\Omega} \quad (8)$$

where  $\mathbf{R}_{\Delta v}$  projects the rotation vectors into a relative velocity at the fault midpoint. Thus, for a given set of rotation vectors,  $\mathbf{R}_{\Delta v}\bar{\Omega}$  gives the two components of the relative velocity vector  $\Delta\bar{v} = (\Delta v_{\parallel}, \Delta v_{\perp})$ .  $\mathbf{R}_F$  projects the relative velocity onto the fault plane. While a dislocation (fault) can have three components of slip (strike, dip, and tensile, alternatively  $s_{\parallel}$ ,  $s_{\delta}$  and  $s_{\perp}$ ), we only allow two components of slip for each fault. The strike slip component of all faults is equal to the projection of the relative velocity vector along the fault azimuth. In addition, vertical faults have a tensile slip component equal to the convergence rate. Faults with dips other than  $90^{\circ}$  have no tensile slip (opening or closing) but instead, have a non - zero dip slip component that depends on the dip of the fault. For a given convergence rate, the dip slip rate on a non - vertical fault increases with dip. The relationship between the fault-normal components of the relative block velocity vector to the non-strike slip rates is

$$\Delta v_{\perp} = \begin{cases} s_{\perp} & \text{if } \delta = 90^{\circ} \\ s_{\delta} \cos \delta & \text{if } \delta \neq 90^{\circ} \end{cases} \quad (9)$$

As the fault slip rates are just projections of relative block motion vectors, the fault slip rates are internally consistent and the surface velocity field implicitly satisfies the path integral constraint on both geodetic and geologic time scales:

$$\oint v_{(B,C,I)}^{(E,N)} dl = 0 \quad (10)$$

where  $(E, N)$  indicates either the east or north components of the velocity field and  $dl$  is a differential line element along the integration path. The subscripts  $(B, C, I)$  indicate the block, coseismic slip deficit, and interseismic field respectively. In other words, the path integral constraint states that the relative motion between any two points does not depend on the path between them. This constraint is an implicit feature of the block model and ensures that we generate internally consistent slip rate estimates.

We substitute equations (6), (7) and (8) into (5) to write the interseismic velocities in terms a single multiplication,  $\vec{v}_I = (\mathbf{R}_B - \mathbf{R}_C)\vec{\Omega}$  where  $\mathbf{R}_C$  is a combination of all of the other  $\mathbf{R}$  matrices in equations (7) and (8). While our study is primarily concerned with inverting geodetic data for block motions, the method presented above also affords the possibility to include both *a priori* slip rate and plate motion estimates into the same inversion. We can write the forward problem as a system of equations as follows:

$$\begin{pmatrix} \vec{v}_I \\ \vec{s} \\ \vec{\Omega} \end{pmatrix} = \begin{pmatrix} \mathbf{R}_B - \mathbf{R}_C \\ \mathbf{R}_F \mathbf{R}_{\Delta v} \\ \mathbf{I} \end{pmatrix} \vec{\Omega} \quad (11)$$

We are interested in the inverse problem where we have to estimate  $\bar{\Omega}_{\text{est}}$ . If we write (11) as  $\mathbf{R}\bar{\Omega} = \bar{d}$  (where  $\bar{d}$  represents all of the data and  $\mathbf{R}$  is a compilation of all of the  $\mathbf{R}$ 's) then we can estimate a set of rotation vectors by minimization of the sum of weighted least squares

$$\bar{\Omega}_{\text{est}} = (\mathbf{R}^T \mathbf{W} \mathbf{R})^{-1} \mathbf{R}^T \mathbf{W} \bar{d} \quad (12)$$

where  $\mathbf{W}$  is the combined weighting matrix. This matrix contains the weights for each of the data sets (observed velocities, slip rates, *a priori* block motions),

$$\mathbf{W} = \begin{pmatrix} \beta_G \mathbf{W}_G & 0 & 0 \\ 0 & \beta_s \mathbf{W}_s & 0 \\ 0 & 0 & \beta_\Omega \mathbf{W}_\Omega \end{pmatrix} \quad (13)$$

where each of the  $\mathbf{W}$ 's on the right hand side of (13) is the inverse of the covariance matrix associated with each data set. We treat covariance matrices as diagonal, with the exception of the east - north velocity correlations at each station. We do not currently use the full covariance for the geodetic data. Each of the  $\beta$ 's in equation (13) is a coefficient that sets the relative weights for each data set. These parameters are useful when there is an imbalance between the number of equations representing geodetic data and the number of *a priori* slip rate estimates. In addition to the estimated rotation vectors, we

can obtain the estimated slip rates,  $\vec{s}_{\text{est}}$ , by substituting  $\vec{\Omega}_{\text{est}}$  into equation (8). Formal slip rate uncertainties are calculated by propagating the estimated rotation vector uncertainties through equation (8). The Euler pole location and rotation rate uncertainties are calculated by Monte Carlo propagation so that we do not have to linearize the conversion from rotation vector to Euler pole space.

As previously discussed, we can also include *a priori* plate motion or slip rate estimates into the inversion. Although this provides us with a convenient framework for performing joint inversions of geologic and geodetic data, we decided to focus on the geodetic data in this paper. However, we have used some kinematic constraints to eliminate “checker board” deformation. This behavior consists of an alternating pattern of large amounts of convergence and divergence along what are thought to be predominantly strike slip faults. While the magnitude of normal motion may be large on any one of these faults, the sum across the system is small. We find that “checker boarding” occurs along the faults bounding a series of long, thin blocks, such as those south of Los Angeles and in the Eastern California Shear Zone. To minimize this artifact of the inversion, we have added several constraints that limit the normal motion on faults that would otherwise show “checker board” behavior. In the common deep-slip approach to modelling interseismic deformation (e.g., *Hubert-Ferrari et al.*, 2000, *Segall*, 2002) there is a strong covariance between locking depth and slip rate. The block model approach reduces this covariance by reducing the number of correlated model parameters (faults vs. blocks) and thus reduces fault slip rate uncertainties (*Meade et al.*, 2002).

## 5. Geodetic data

The SCEC3.0 Crustal Motion Map<sup>4</sup> provides the best published estimate of interseismic deformation at the regional scale in Southern California. Included in the velocity field are data from both survey mode and continuous Global Positioning System (GPS), from Very Long Baseline Interferometry (VLBI), and from Electronic Distance Measurement (EDM) measurements. Most of the data are survey-mode GPS, with some of the older stations having time series that span nearly ten years. During the period of GPS observations, there have been three large earthquakes in Southern California: the 1992 Landers earthquake ( $M_w = 7.3$ ) in the southern Mojave Desert, the  $M_w = 6.7$  Northridge (1994) event on a previously unrecognized blind thrust fault in the Ventura Basin, and the  $M_w = 7.1$  Hector Mine (1999) earthquake, which ruptured about 100 km to the east-northeast of the Landers rupture. Coseismic and postseismic deformation from these earthquakes has made it more difficult to evaluate some of the longer time series for interseismic deformation. An effort was made in the development of the SCEC3.0 CMM to cut out both the coseismic signal and the  $< 1.5$ -year postseismic signals associated with these events<sup>5</sup>. There may be additional long-term relaxation effects in the geodetic data. We discuss this possibility later in the context of the block model results.

---

<sup>4</sup> <http://epicenter.usc.edu/cmm3>

<sup>5</sup> <http://epicenter.usc.edu/cmm3/summan.html>

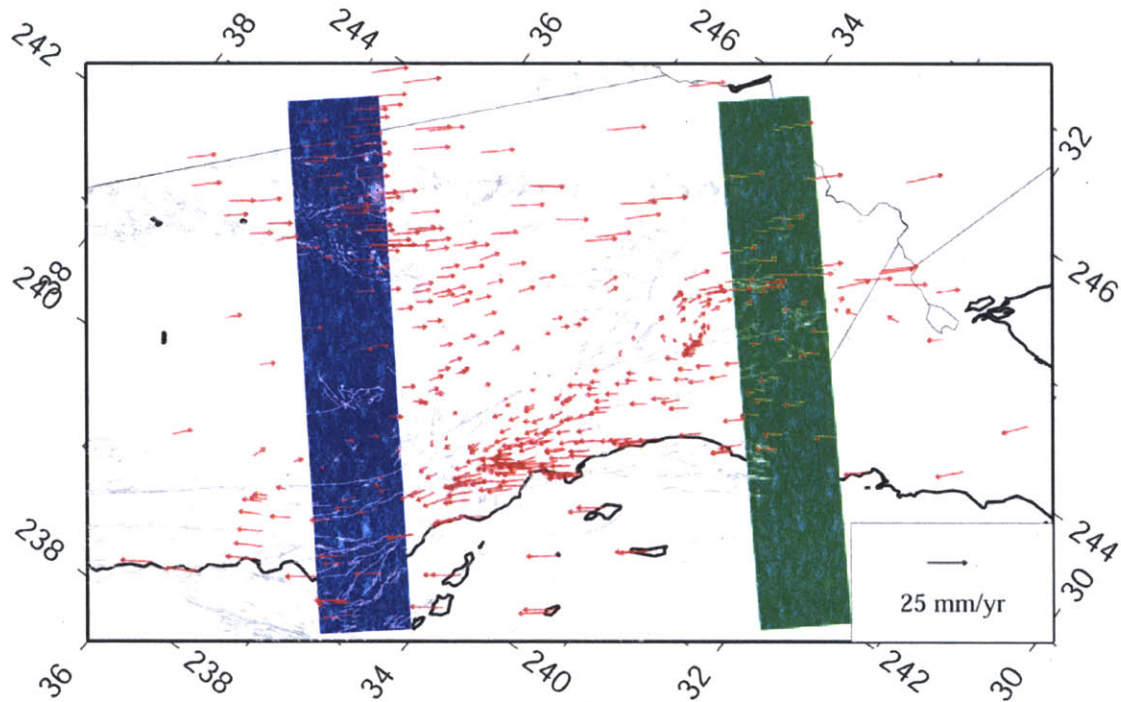


**Figure 5.** Here we show the observed velocity field in Southern California that we used to estimate block motions. No confidence ellipses are shown in order to reduce clutter. The velocities are a combination of the SCEC3.0 field and an update of *McClusky et al. (2001)*. The map projection is a locally tangent oblique Mercator with the azimuth oriented approximately parallel to the SAF. The Pacific Ocean is at the bottom of the figure and North America is at the top. (This projection is used for many of the other geographic figures in this paper.) The velocities are in a mean Southern California reference frame to highlight the dynamic range of the data. The shaded swaths indicate the areas over which stations are included in the profiles shown in figure 6. The light gray lines are fault traces from *Jennings et al. (1994)*.

The SCEC3.0 Crustal Motion Map contains estimated velocities for more than 840 stations with observations through 2001. To ensure that we model the Pacific Plate motion adequately, we combined the SCEC velocities with the far-field velocities reported by *Steblov et al. (2003)*. We added four stations from the BARD network that lie

on the northern extension of the Sierra Block (UCD1, SUTB, QUIN, and ORVB)<sup>6</sup>; this was required to produce a robust estimate of the Sierra Block motion and thus the San Andreas Fault slip rate. To increase data coverage in the Eastern California Shear Zone (ECSZ), we used an update of the station velocities of *McClusky et al.* (2001). The combination was done by solving for the rotation vector that minimized the difference in velocities at common stations. *McClusky's* analysis (including longer time series) yields smaller uncertainties than most of the campaign-mode data in the SCEC3.0 velocity field. To put the velocity fields on an equal footing we increased the McClusky uncertainty estimates by  $\sim 0.4$  mm/yr so that these two data sets shared the same median uncertainty. For the small number of far field stations we use the reported velocities uncertainty estimates.

We also removed a large number of sites. First, we discarded all velocities with uncertainties larger than 1.5 mm/yr in the east or north component. Such large uncertainties complicate the evaluation of the models without contributing substantially to providing constraints in the weighted least squares inversion. The 1992 Landers earthquake interrupts some of the longer time series and is the source of many challenges. For many stations installed after Landers, rapid postseismic deformation is evident for at least two years following the event; such sites were eliminated. We chose not to use the EDM velocities in the SCEC3.0 field because the network tie relationships were not readily available; the EDM residual velocities in preliminary models showed coherent patterns relative to nearby GPS sites that are probably related to network tie problems but

---

<sup>6</sup> <http://quake.geo.berkeley.edu/bard/bard.html>



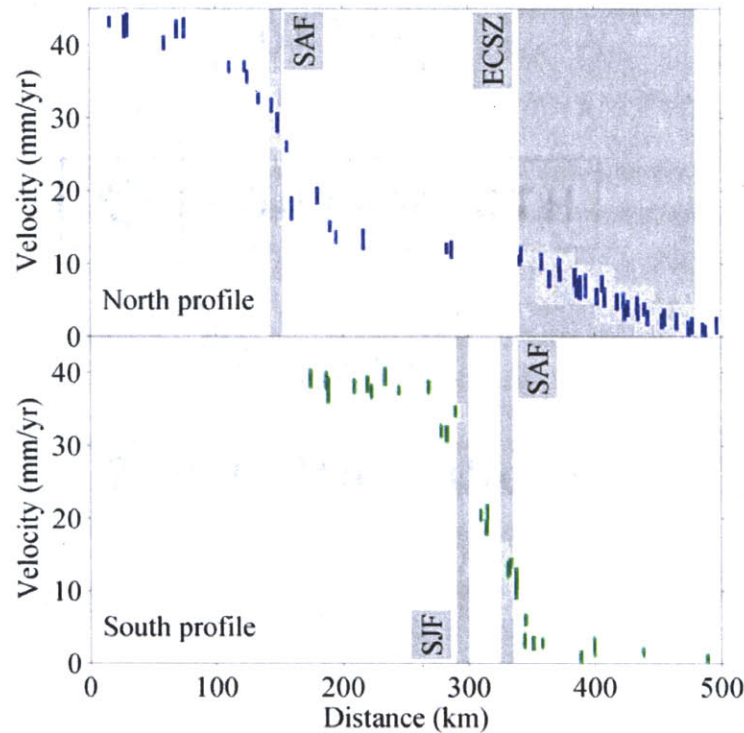
were easy to confuse with block motions. Some of the older VLBI sites have small formal uncertainties, but their velocities often depart significantly from collocated GPS stations, leading us to eliminate all VLBI sites in favor of a uniform data set. Many velocities are also affected by non-tectonic signals, such as anthropogenic subsidence (e.g., *Bawden et al.* 2001). *Bawden's* web site<sup>7</sup> provides a map of regions and station names identified as having complicated time series. Stations in the immediate vicinity of Parkfield were eliminated as the fault behavior there is dominated by complex partially creeping behavior (e.g., *Murray and Segall*, 2002). We also eliminated stations in complicated regions that were outside of our study area, such as those in the San Francisco area and the Basin and Range Province. In the ECSZ, we eliminated stations near the COSO geothermal field and stations that we suspected of demonstrating significant postseismic motion from the Landers and Hector Mine earthquakes. We also eliminated stations that are commonly thought to have local site effects (AGUE, 0501). The last step in the reducing the velocity field was an iterative cleaning procedure. This involved looking at the residuals from the block model and identifying stations that had residual velocities that were anomalous compared with their immediate neighbors. After this procedure, our combined velocity field has 447 stations.

Figure 5 shows the resulting velocity field in a Southern California reference frame. Stations in the top half move toward the southeast while those at the bottom move toward the northwest at about half of the Pacific plate velocity. The velocity vectors near the San Andreas and San Jacinto Faults are the smallest and mark the major boundary

---

<sup>7</sup> <http://quake.wr.usgs.gov/research/deformation/modeling/socal/la/index.html>

between the Pacific and North American plates. Across the Southern California fault system the observed velocities do not jump abruptly across the SAF, but instead vary smoothly. The fault parallel velocities in figure 6 show this more clearly. The fault parallel velocities and uncertainties (from the two shaded swaths in figure 5) are shown in figure 6. The gradual transitions across the fault zones are similar to the simple interseismic velocity model shown in figure 3. In the southernmost profile it is difficult to separate the effects of the SAF and SJF. Note that while each of the profiles shows approximately the same velocity change ( $\sim 40$  mm/yr) from the Pacific to the North American plates, the distributions are different. In the north, the fault-parallel velocity drops by about  $\sim 30$  mm/yr across the SAF. Further to the east, the velocity gradient flattens out before dropping  $\sim 12$  mm/yr across the Eastern California Shear Zone. In contrast, the southern profile shows no intermediate flattening and the total velocity drop occurs across a distance that is about 50% that in the northern profile. This reflects the difference in the fault system geometry from north to south. The flat portion of the northern profile reflects the relative stability of the  $\sim 200$  km wide Sierra Block, with the actively deforming central SAF to the west and ECSZ to the east. In contrast, approximately 80% of the relative plate motion is accommodated across the SAF and SJF, separated by only  $\sim 40$  km.



**Figure 6.** Fault parallel velocities from the northern and southern swaths, respectively shown in figure 5. The vertical lines give the  $1\sigma$  fault parallel velocity uncertainty estimates. The heavy shaded areas show the locations of various fault zones (SAF: San Andreas Fault, ECSZ: Eastern California Shear Zone, SJF: San Jacinto Fault.) The total change in velocity across both profiles is about 40 mm/yr but the transition occurs over a distance about half as wide in the south. This is due to the close spacing of the SJF and SAF in the compared to the distance between the SAF and ECSZ in the north. The Sierra block separates these two zones of deformation. Notice the similarities between these profiles and the simple theoretical one shown in the middle panel of figure 3.

## 6. Southern California block geometry

The number of faults in Southern California results in a geometrically complex block model compared with other major continental transform boundaries such as the North Anatolian Fault zone (e.g., *Meade et al.*, 2002). We adopt a model with twenty-two blocks (figure 7).

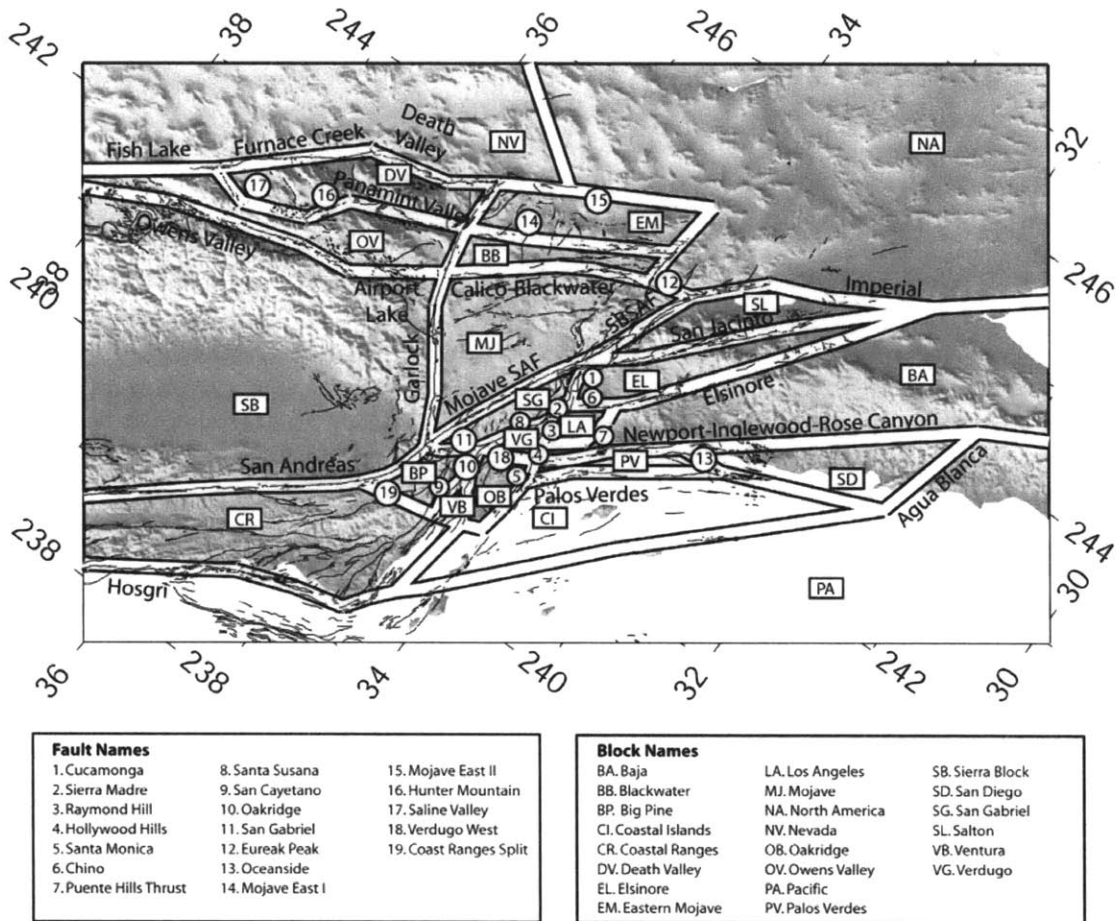


**Figure 7.** Topography (GTOPO30), fault traces (*Jennings*, 1994, thin black lines) and model block boundaries (thick lines) in and around Southern California. The map projection allows the San Andreas Fault to run left to right outside of the Big Bend. North is towards the upper left corner. The 22 blocks in our preferred model are labeled (rectangles): Baja (BA), Blackwater (BB), Big Pine (BP), Coast Islands (CI), Coastal Ranges (CR), Death Valley (DV), Elsinore (EL), Eastern Mojave (EM), Los Angeles (LA), Mojave (MJ), North America (NA), Oakridge (OB), Owens Valley (OV), Nevada (NV), Pacific (PA), Palos Verdes (PV), Sierra (SB), San Diego (SD), San Gabriel (SG), Salton (SL), Ventura Basin (VB), Verdugo (VG). The block labels are given the box in the lower right corner. Selected fault names are labeled either directly on the fault or by reference. Circled numbers refer to faults and their names are given in the box in the lower left corner.

These blocks range in size from very large (i.e., the plate-scale Pacific and North American blocks) to blocks like the Ventura block (figure 8), which have an area of only a couple of hundred square kilometers. Our block boundaries often represent coarsely structures that are much more complicated in the real world. In these cases, the model faults are idealizations. We arrived at this preferred model by an iterative procedure, starting with the *Jennings* (1994) fault map and the work of previous authors (e.g., *Bird and Rosenstock*, 1984, *Bird and Kong*, 1994, *Bennett et al.*, 1996, and *Souter*, 1998). We then modified the fault system geometry to accommodate the observed velocities and some of our geologic prejudices. This allowed us to develop a model that is compatible with much of the mapped fault system geometry and the observations of interseismic deformation. However, we were forced to introduce some features that have no direct geologic analog (e.g., the split between the Coastal Ranges and Big Pine block, as well as the split between the Oakridge and Verdugo blocks). Without the division between the Coastal Ranges and Big Pine block, the residual velocity field north of the Ventura basin and west of the central San Andreas fault have a coherent southerly and northerly velocities respectively. With the structure that separates the Coastal Ranges and Big Pine blocks (figure 7, structure 19) the residuals are minimized and we can recover both substantial shortening along the northern edge of the Ventura Basin and a right lateral strike slip rate greater than 30 mm/yr on the Central San Andreas fault. We included the north south trending structure that runs from the Northridge rupture to the northern edge of the Los Angeles basin (figure 7, structure 18) to allow model residual velocities around the Northridge rupture zone.

The number of blocks was limited not by computational concerns but by our ability to invert for a reasonable model. As the blocks became smaller, the correlations between model parameters increase and “checker boarding” becomes more problematic. We are unable to separate the compound effects of faults that are very close to each other (e.g., San Jose and Sierra Madre fault zones near the San Gabriel range front). However, St. Venant’s principle (e.g., *Malvern*, 1969) assures that the elastic effects further away from the fault zone are not sensitive to the details of the locked geometry. For this reason, our block boundaries are smoother than the corresponding faults on the *Jennings* (1994) map. The residual velocities and GPS uncertainty estimates suggest that our block model has a reasonable number of parameters from a statistical point of view.

Our preferred model includes the following twenty two blocks: Baja (BA), Blackwater (BB), Big Pine (BP), Coast Islands (CI), Coast Ranges (CR), Death Valley (DV), Elsinore (EL), Eastern Mojave (EM), Los Angeles (LA), Mojave (MJ), Nevada (NV), North America (NA), Oak Ridge (OB), Owens Valley (OV), Pacific (PA), Palos Verdes (PV), Sierra Block (SB), San Diego (SD), San Gabriel (SG), Salton (SL), Ventura (VB) and Verdugo (VG).

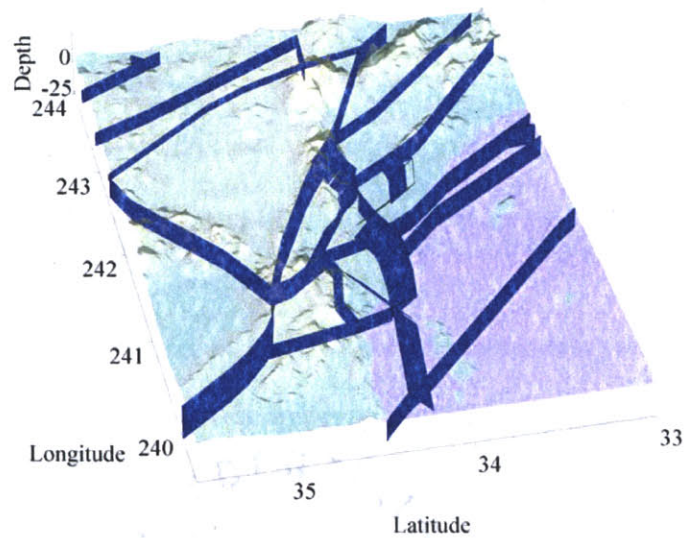


**Figure 8.** A three dimensional view, with topography (GTOPO30), of the fault geometry of our preferred model focused on the Los Angeles region. The view is from the west - northwest. The Mojave segment of the SAF is difficult so see as it is almost aligned with the look direction. The same is true for the Oakridge and Puente Hills Thrust fault systems, which appear nearly edge on. All of the non-vertical faults dip at  $45^\circ$ .

## 7. Results and Interpretation

### 7.1. Locking depth variations

The third dimension of the fault system geometry is the fault locking depth. With elastic dislocation models, deeper locking depths lead to wider zones of strain accumulation. In general, the locking depths of faults are unknown. Recent work detailing precise micro-earthquake locations provides information regarding the location of asperities (e.g., *Shaff et al.* 2002) and, possibly, the depth of the brittle ductile transition. As this technique is applied at a larger scale, it may become a valuable resource to help constrain down-dip fault geometry and be a useful proxy for locking

depth. Given that we don't know the locking depths *a priori*, and that our rheologic assumptions (i.e., purely elastic) may be too crude to incorporate them properly, we decided to estimate the locking depths of some critical fault segments. This also allows us to interpret locking depths in terms of a viscoelastic earthquake cycle (see appendix A).

Our preferred model has substantial locking depth variations, from 0-25 km. For those faults where slip rates are high enough and coverage is dense enough, we estimated locking depths. For the remainder, we used results of previous studies, where available, or a default value of 15 km. *Peltzer et al.*, (2001) estimated a very shallow locking depth (~5 km) for the Blackwater fault, and we use the same value for consistency. For the rest of the ECSZ we use a 10 km locking depth as suggested by *McClusky et al.* (2001). We allow the Imperial Fault (southern SAF) to creep. We also recognized that in the Ventura basin the Northridge earthquake ruptured to a depth of 16 km, thus providing us with an objective estimate for the local locking depth. However, *Donnellan et al.* (1993a, b) found that a 5 km locking depth could best fit two-dimensional profiles of fault normal velocities in this same region. *Hager et al.* (1999) demonstrated that this shallow locking depth mimics the effects of the lateral shear modulus variations in the Ventura Basin. We use a 5 km locking depth in our model, but interpret it as a deep locking depth in the Earth.

To estimate locking depths, we used a grid search, as the model velocities are non-linear with respect to these parameters. In contrast to *Lyons and Sandwell* (2003), we find that the SAF just to the east of the Salton Sea is fit best by a 15 km locking depth.



This may reflect a bias in the data, for example, the inclusion of velocities affected by transient postseismic deformation following the Landers and/or Hector Mine earthquakes. The fault locking depths that bear most directly on both the fit to the data and the estimated fault slip rates are those of the Mojave and Carrizo segments of the SAF. This is the same section that ruptured in the 1857 Ft. Tejon earthquake (e.g., *Sieh*, 1978). Figure 9 shows how the geodetic data fit the model for FTSAF locking depths ranging from 0 to 40 km. These statistics were calculated by doing separate inversions for each locking depth. The fit is best at approximately 25 km, with shallower locking depths fitting the data very poorly ( $\chi^2(d=0) = 2.1\chi^2(d=25)$ ). The dashed curve in figure 9 shows how the strike slip rate along the Carrizo segment of the SAF varies with locking depth. For the best-fit locking depth, the SAF slips at  $35.7 \pm 0.6$  mm/yr. Shallower locking depths severely underestimate the fault slip rate. The formal slip rate uncertainties grow as a function of locking depth. This is because the relative block motions become more coupled as the locking depth increases. In the end member case, where all the faults have zero locking depth, there is no coupling between the blocks, and the only contribution to the slip rate uncertainties is from the data uncertainties.

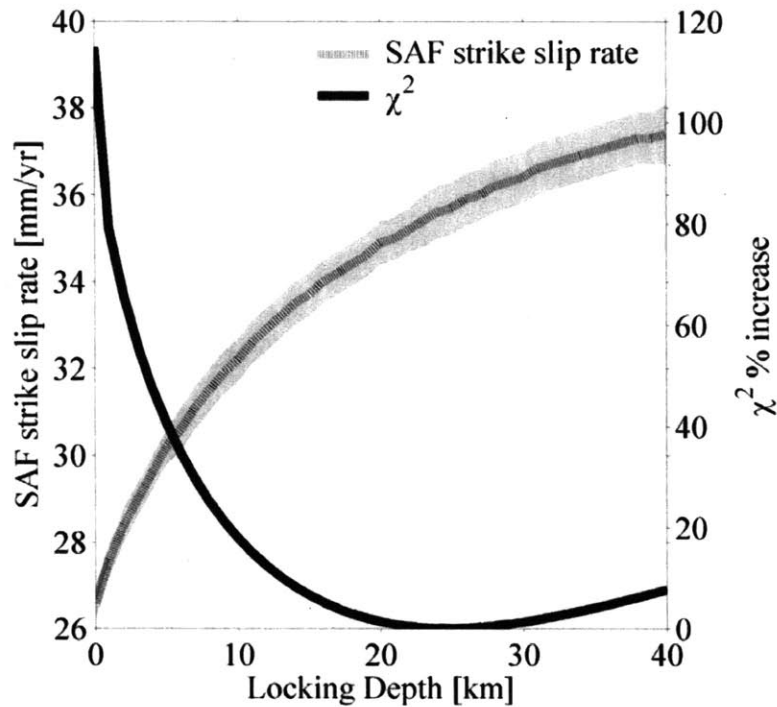


**Figure 9.** The fit to the data and slip rate on the Carrizo segment of the SAF are shown as a function of the locking depth of the segment of the SAF that ruptured in the 1857 Ft. Tejon earthquake (FTSAF). The solid black line shows the fit ( $\chi^2$ ) as a function of FTSAF locking depth, with a minimum at 25 km. The monotonically increasing dashed-dot curved shows the Carrizo plain strike slip rate as a function of FTSAF locking depth. Surrounding this curve, the shaded region indicates the slip rate uncertainty at each locking depth. The uncertainties become larger with increasing locking depths because the elastic deformation zone broadens around the fault and the correlation between the estimated model parameters (rotation vectors) increases. Our preferred slip rate for the Carrizo segment of the SAF is the slip rate at the locking depth that minimizes the  $\chi^2$ . This corresponds to  $35.7 \pm 0.6$  mm/yr at a FTSAF locking depth of 25 km.

We discuss possible interpretations of this locking depth in a later section. Experiments with synthetic data and 2D models show that the asymmetry in the  $\chi^2(d)$  curve is due to the decrease in the sensitivity to locking depth ( $\partial v/\partial d$ ) with depth. Thus, our locking depth estimate is consistent with what we would expect from an optimal estimate.

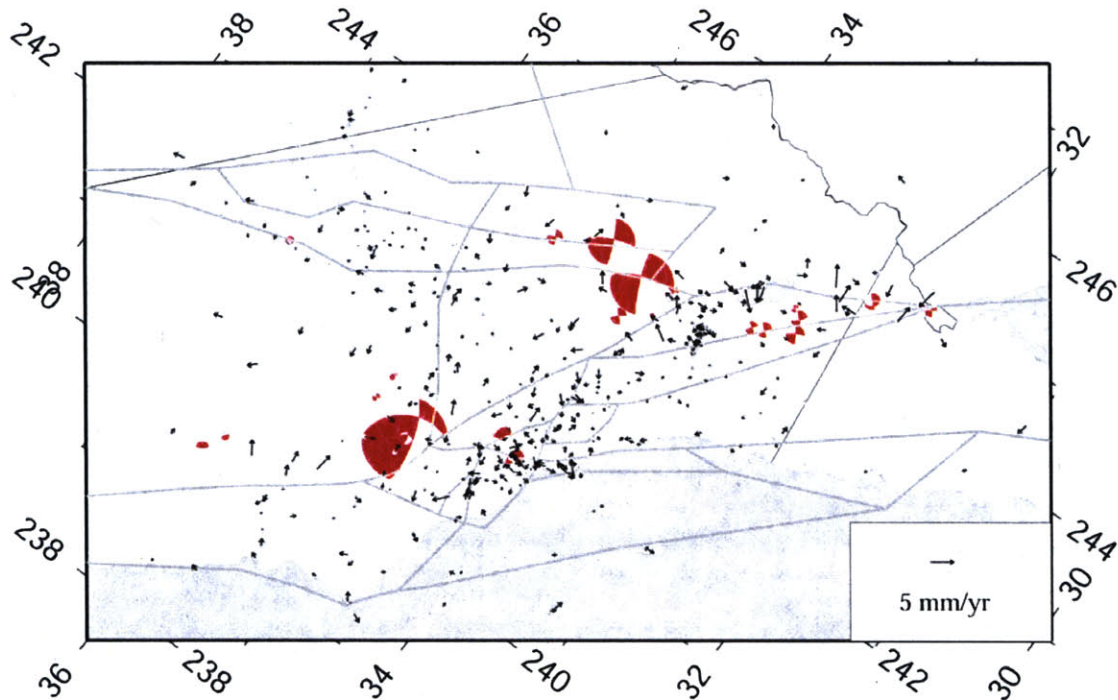


**Figure 10.** Residual (observed - model) velocities. The gray lines show the block model geometry, focal mechanisms are those since 1940 (*Kagan, 2002*) and the small circles indicate the base of each velocity vector. Note that the velocity vectors on this figure are drawn at a scale that is three times larger than the observed velocity vectors shown in figure 5. The 5 mm/yr scale vector in the lower right hand corner has 1 mm/yr uncertainties and is shown with a 95% confidence ellipse. This uncertainty is just smaller than the mean of the combined observations. 69% of the residuals are typically smaller than their associated  $1\text{-}\sigma$  uncertainty estimates.

## 7.2. Fit to data

Our preferred model is able to account for most of the features in the observed velocity field, with a mean residual magnitude of 1.3 mm/yr. The  $\chi_s^2 / \text{DOF} = 1.2$ , and 69% of the residual velocity components are smaller than their  $1\text{-}\sigma$  uncertainty estimates.



the minimization criterion. The correlation between elastic contribution and residual velocity is  $0.18 \pm 0.04$  at the 67% confidence level.

Some coherent residuals may be explained by co- or postseismic motions. Given that coseismic displacement models are generally not accurate to the cm level within a few rupture depths of the epicenter, we have reason to be suspect of coherent residuals in the immediate vicinity of an earthquake with station time series that span the event. Rapid postseismic deformation following large earthquakes may persist at the mm/yr level for more than two years after the coseismic rupture (e.g., *Pollitz et al.*, 2000). The SCEC3.0 CMM only eliminates about 1.5 years of data following the Landers earthquake, and this from only about 30 near-field stations. For both Landers and Northridge, the velocities in the immediate vicinity of the fault are based on the fits to the time series after the events. There is currently no correction for postseismic deformation at Northridge. Either of these explanations may account for the small systematic residuals near the Landers and Northridge earthquakes. It is interesting to note that the residual velocities in both of these regions share the same sense of motion as the coseismic displacements (figures 10, 14). Given the sensitivity to coseismic models and the length of the excluded time series, we abstain from speculating on coherent residual velocities that are in the immediate vicinity of the either the Landers or Northridge rupture zones.

### 7.3. Pacific-North America Euler Pole

The most basic measure of the deformation between the Pacific and North American plates is the relative Euler pole between them (table 1). Our Euler pole location is east of some recent estimates. This is likely due to the inclusion of many more stations on the North American Plate compared with previous studies (e.g., *Sella et al.*, 2002). The difference in Euler Pole location and rotation rate can account for  $\sim 3$  mm/yr of differential motion across the Southern California Fault System. We also estimated the PA-NA Euler pole using a traditional plate model with no elastic deformation and only those stations in the centers of the Pacific and North American Plates. With no elastic deformation and fewer stations, the Euler pole longitude shifts  $3^\circ$  eastward; closer to previous estimates (e.g., *DeMets and Dixon*, 1999, *Sella et al.*, 2001)

Source	Longitude (deg)	Latitude (deg)	Rotation rate (deg/Myr)
NUVEL-1A	$-78.2 \pm 1.3$	$48.7 \pm 1.2$	$0.750 \pm 0.010$
<i>DeMets and Dixon</i> (1999)	$-73.7 \pm 2.0$	$51.5 \pm 1.0$	$0.765 \pm 0.016$
<i>Sella et al.</i> (2001)	$-72.1 \pm 0.6$	$50.4 \pm 0.4$	$0.755 \pm 0.004$
This paper (block model)	$-78.6 \pm 0.4$	$50.7 \pm 0.3$	$0.783 \pm 0.003$
This paper (plate)	$-75.5 \pm 0.3$	$50.4 \pm 0.2$	$0.791 \pm 0.003$

**Table 1.** A compilation of estimated Pacific-North America Euler pole locations and rotation rates, including the estimate from our block model. Our uncertainty estimates were calculated using a Monte Carlo method to convert from rotation vector covariance (directly estimated in the inversion) to a set of Euler Pole locations and rotation rates. This approach tends to reduce the rotation rate uncertainty and increase the pole location uncertainties compared with the linear propagation. The block model estimate includes many stations on the North American Plate in Southern California that are affected by the elastic strain accumulation model. In contrast, the plate motion estimate from this paper includes no elastic deformation and only those stations far from the boundaries of the Pacific and North American Plates.

#### 7.4. Estimated slip rates

In our block model formulation, slip rates are derived parameters, linearly related to the estimated rotation vectors. Figures 12 and 13 show the strike-slip and “fault-normal” slip rates respectively. The “fault-normal” components are tensile if the fault is vertical and dip slip otherwise, with negative values indicating opening or normal faulting. In all cases, the reported slip rates have been calculated at the nearest segment midpoint. Formal uncertainties range from 0.4 to 3.1 mm/yr (table 2). Faults bounded by large blocks tend to have smaller uncertainties (e.g., central SAF). The uncertainties have been calculated after rescaling the model covariance matrix by the mean squared error. This has the effect of increasing uncertainties by a factor of about 1.5. However, experience with a range of models has shown that the uncertainties due to variations in fault system geometry are larger than those associated with the velocity uncertainties. In practice, the reported slip rate uncertainties should be scaled upwards to reflect the effects of different fault system geometries. Empirical evidence suggests that  $\pm 3$  mm/yr is an appropriate uncertainty for most individual faults.

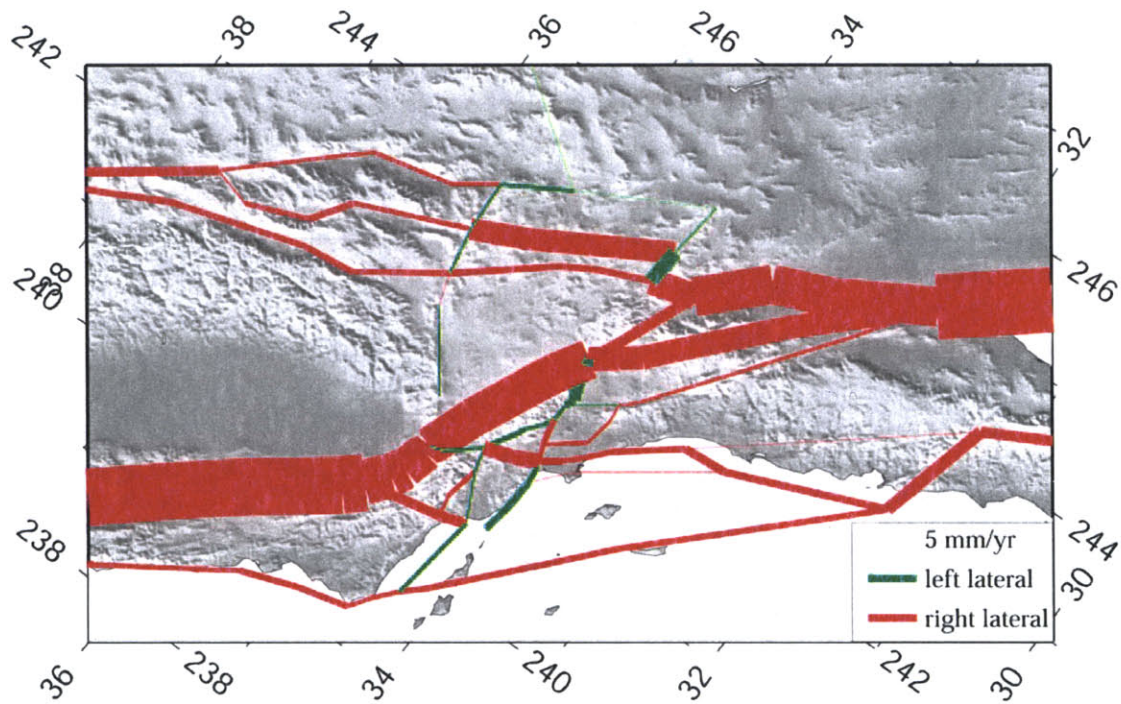


**Figure 12.** The estimated strike slip rates from our preferred block model. Red and green lines indicate right and left lateral motion respectively. Wider lines indicate faster slip rates. The thickest lines represent the San Andreas – San Jacinto Fault system where more than 50% of the relative plate motion is accommodated.



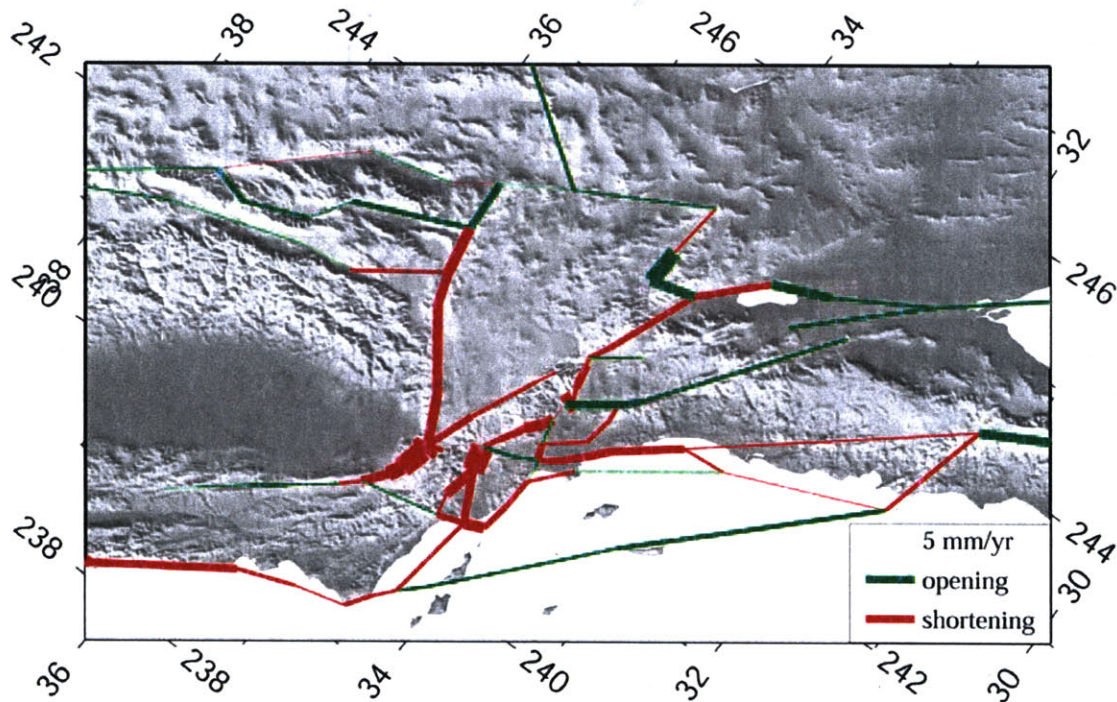


**Figure 13.** The estimated dip and tensile slip rates from our preferred block model. Red and green lines indicate closing and opening respectively. Wider lines indicate faster slip rates. Slip rates are tensile for vertical faults and dip slip for dipping faults. The only faults that dip are those around the Los Angeles area (see figure 8 and table 2). Dip slip faults along the San Gabriel range front and those at the northern edge of the Ventura basin range between 0.5 and 13.5 mm/yr.

<b>Fault name</b>	<b>Strike slip rate</b>	<b>Dip slip rate</b>	<b>Tensile slip rate</b>
SAF (Parkfield)	35.8 ± 0.4	--	-0.9 ± 0.4
SAF (Carrizo)	35.7 ± 0.6	--	2.0 ± 0.4
SAF (Mojave)	24.4 ± 1.0	--	2.3 ± 1.4
SAF (San Bernadino)	6.6 ± 0.9	--	3.7 ± 0.6
SAF (Salton Sea)	24.5 ± 0.4	--	-5.6 ± 0.4
SAF (Imperial)	24.7 ± 0.8	--	-2.2 ± 0.5
SAF (Cerro Prieto)	41.0 ± 1.5	--	-2.2 ± 0.4
Eureka Peak	16.3 ± 0.4	--	-5.9 ± 0.5
Pinto Mountain	-9.3 ± 0.6	--	-9.7 ± 1.0
San Jacinto	14.5 ± 1.0	--	0.0 ± 0.6
Elsinore	2.0 ± 1.9	--	-2.2 ± 0.7
Rose Canyon	0.2 ± 1.9	--	1.1 ± 1.4
Oceanside	5.4 ± 2.7	--	1.7 ± 3.1
Coronado Bank	4.6 ± 3.1	--	0.6 ± 1.9
San Clemente	4.0 ± 1.9	--	-2.0 ± 1.0
Hosgri	4.0 ± 0.0	--	0.9 ± 0.6
Agua Blanca	7.7 ± 2.5	--	2.3 ± 1.4
Newport – Inglewood	3.5 ± 2.3	--	4.9 ± 1.4
Palos Verdes	0.4 ± 1.9	--	1.9 ± 1.6
Raymond Hill	3.6 ± 1.6	--	-1.3 ± 2.4
Whittier	0.9 ± 1.0	2.2 ± 1.3	--
Chino	-0.8 ± 1.3	--	-5.2 ± 0.9
Puente Hills Thrust	1.5 ± 1.0	2.5 ± 0.9	--
Cucamonga	-7.1 ± 1.2	4.7 ± 1.3	--
Hollywood Hills	3.6 ± 1.7	3.9 ± 2.4	--
Santa Monica Mountains	-3.1 ± 1.7	-0.5 ± 2.2	--
Verdugo West	8.8 ± 2.5	--	-2.2 ± 1.5
Sierra Madre (north)	-2.5 ± 1.7	6.6 ± 2.7	--
Sierra Madre (south)	-1.9 ± 1.2	0.5 ± 2.0	--
Santa Susana	-3.2 ± 1.6	3.0 ± 2.7	--
San Cayetano	2.8 ± 1.3	6.0 ± 2.1	--
Oakridge	-1.6 ± 1.4	4.7 ± 2.8	--
Coastal Ranges Split	6.1 ± 1.4	--	-1.1 ± 1.0
San Gabriel	-1.7 ± 2.2	---	2.9 ± 1.5
Western Garlock	-1.2 ± 0.4	--	5.8 ± 0.7
Central Garlock (Searle's Lake)	-1.8 ± 1.2	--	6.3 ± 0.9
Eastern Garlock	-1.7 ± 1.7	--	-4.8 ± 1.3
Blackwater-Landers	4.0 ± 0.8	--	0.0 ± 0.8
Eastern Mojave (1)	13.7 ± 0.8	--	0.0 ± 1.4
Eastern Mojave (2)	-0.5 ± 0.6	--	-1.7 ± 0.7
Nevada Split	-0.5 ± 0.6	--	-2.4 ± 0.6
Airport Lake	3.8 ± 0.6	--	-0.5 ± 0.5
Owens Valley	3.8 ± 0.8	--	-0.6 ± 0.7
Panamint Valley	3.0 ± 1.3	--	-3.2 ± 1.2
Death Valley	2.3 ± 1.2	--	-0.8 ± 0.9
Fish Lake	5.8 ± 2.0	--	-1.1 ± 1.0

**Table 2.** Selected fault slip rates from our preferred block model. All rates are given in mm/yr. Positive and negative strike slip rates give right and left lateral motion respectively. Positive and negative dip slip rates give thrust and normal motion respectively. Positive and negative tensile rates give closing and opening motion respectively. In all cases the slip rate is evaluated at the middle of the segment. SAF is used as an abbreviation for the San Andreas Fault.

### 7.5. The San Andreas Fault system

The SAF shows up clearly in figure 12, with the northernmost (Parkfield) and southernmost (Cerro Prieto) sections moving at  $35.7 \pm 0.6$  and  $41.0 \pm 1.5$  mm/yr, respectively. The SAF transfers 2 mm/yr of strike slip motion to the Elsinore fault and  $14.5 \pm 1.0$  mm/yr to the San Jacinto fault to the south of the Salton Sea. To the northwest, the SAF slows as it feeds  $16.3 \pm 0.4$  mm/yr of strike slip motion into the ECSZ through the Hidden Spring and Eureka Valley faults. This series of fault intersections along the southern SAF leaves only  $6.6 \pm 0.9$  mm/yr of right lateral motion at the San Bernadino segment near the San Gorgonio Pass. The implications of this low slip rate for the evolution of the fault system and seismic hazard are discussed below. Shortening ( $3.7 \pm 0.6$  mm/yr) along the San Bernadino segment of the San Andreas Fault is a consequence of the Salton block impinging upon the southern edge of the Mojave block. Along the Mojave segment, the SAF slips at  $24.4 \pm 1.0$  mm/yr, due to rejoining with the SJF. As the SAF hooks to the north and emerges out of the Big Bend, a 25 mm/yr right lateral strike slip rate is complemented by  $\sim 5$  mm/yr of shortening. This is due to Big Pine block impinging on the southern boundary of the Sierra Block. The

White Wolf Fault may accommodate some of this shortening. At the northern edge of our model the SAF has straightened out and runs through Parkfield at  $35.8 \pm 0.4$  mm/yr.

### 7.6. Shortening across Transverse Ranges and Los Angeles Basin

Our model shows substantial shortening across the Transverse Ranges. The string of thrust faults that runs from the Cucamonga in the east, through the Sierra Madre, Santa Susana, San Cayetano, to Oak Ridge in the west, accommodates between 0.5 and 13.5 mm/yr of dip slip motion. The lowest slip rates are on the southern Sierra Madre Fault and the highest slip rates are found just to the north of the Northridge rupture between the Big Pine and Oakridge blocks. Shortening rates vary along the San Gabriel Range front decreasing southward from the San Gabriel Fault to the Sierra Madre Fault ( $2.9 \pm 1.5 - 6.6 \pm 2.7$  mm/yr).

We find between 1 and 6 mm/yr on both the northern and southern edges of the Ventura basin. These rates are comparable to the convergence rates estimated by *Donnellan et al.* (1993a, b) and *Hager et al.* (1999). Convergence rates on the northern boundary decrease to the west, consistent with counterclockwise rotation relative to the Big Pine block. We are unable to constrain the seaward extent of the active Ventura basin due to the lack of offshore geodetic observations.

Counter clockwise rotation of the Oakridge block leads to a small amount of normal motion ( $0.5 \pm 2.2$  mm/yr) on the model Santa Monica Mountains fault. The same rotation drives shortening at the boundary with the Big Pine Fault, shortening on the

Malibu Hills fault, and 5 mm/yr right lateral strike slip motion on the structure separating the Verdugo and Oakridge blocks. In contrast to geologic estimates of left lateral motion (e.g., *Weaver and Dolan, 2000*), we find  $3.6 \pm 1.6$  mm/yr of right lateral motion on the model Raymond Hill fault.

In the Los Angeles Basin, we find both shortening and right lateral motion on the Puente Hills Thrust (2 mm/yr dip slip) and the Newport-Inglewood Fault (4 mm/yr shortening) in addition to right lateral motion. In contrast to *Bawden et al. (2001)*, our experiments suggest that there is no significant shortening across the Elysian Park Thrust (EPT). Residual velocities from models with an EPT structure replacing the PHT clearly indicate the need for shortening across the PHT. The residual velocities in figure 14 show no indication of unmodeled deformation normal to the EPT. We agree with both *Bawden et al. (2001)* and *Argus et al. (1999)* that the regional geodetic data are most compatible with active shortening in the Los Angeles Basin. Like *Bawden et al. (2001)* and *Argus et al. (1999)*, we disagree with the *Walls et al. (1998)* interpretation of GPS velocities. They argued for escape tectonics, where conjugate strike slip faulting accommodates the north-south shortening of the basin. Our model shows little evidence for the left lateral slip that the *Walls et al. (1998)* model requires. This difference is not unexpected, as *Walls et al. (1998)* did not account for any interseismic strain accumulation. Our model treats the PHT as a blind thrust, with the upper end of the locked portion terminating at 5 kilometers depth. (*Shaw et al., 2002*). *Dolan et al. (2003)* suggested that the PHT related folds above the blind thrust likely grow coseismically,

however, in our model the fit is improved if they are allowed to creep and grow interseismically.

Further to the south, the counterclockwise rotation of the Palos Verdes block relative to the San Diego block leads to shortening across the Oceanside structure. This is an interesting kinematic result, as a right step in a right lateral fault system would necessarily be extensional if there were no rotation.

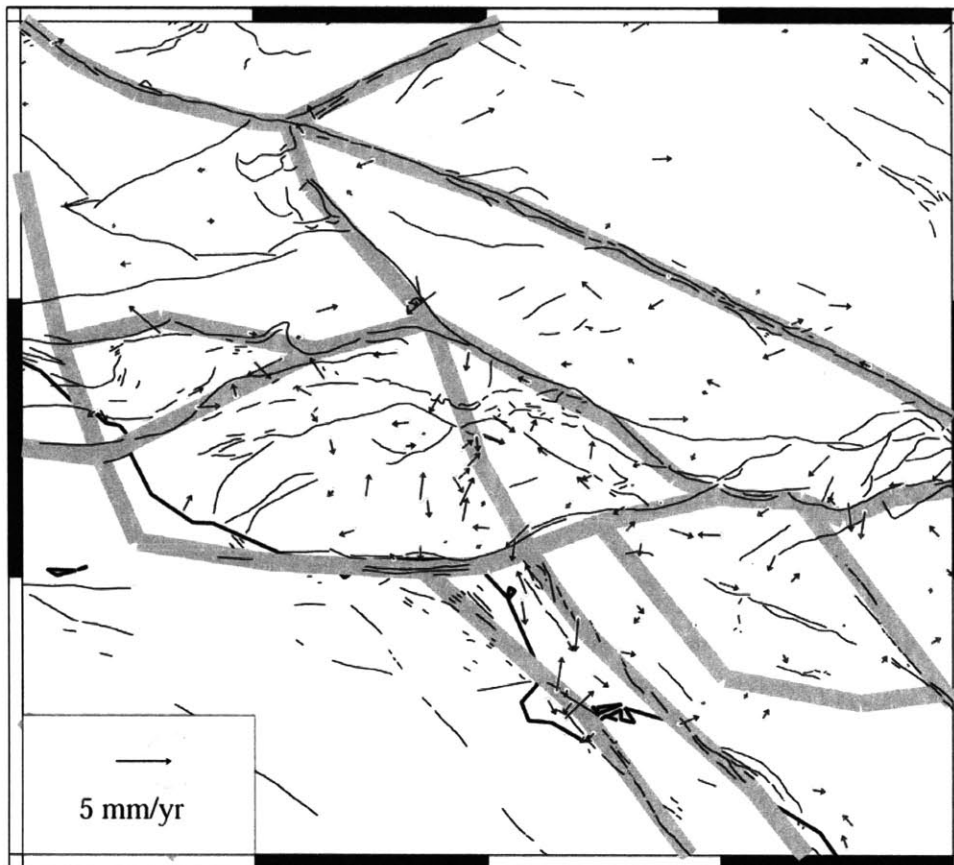


**Figure 14.** Residual velocities in a region centered on the Los Angeles basin. The block boundaries are shown in gray while the fault traces from *Jennings* (1994) are thin black lines.

### 7.7. Eastern California Shear Zone

In the ECSZ, north of the Garlock Fault (GF), our results are similar to those of *McClusky et al.* (2001). The Airport Lake - Owens Valley fault system carries about 4 mm/yr of right lateral motion, and the Panamint Valley - Hunter fault system, to the east, carries ~3 mm/yr. The Owens Valley Fault zone to the north of the Airport Lake fault moves at  $3.8 \pm 0.8$  mm/yr in a right lateral sense. This slip rate agrees with *McClusky et al.* (2001) within the stated uncertainties but it is higher than the Holocene geologic estimate by *Beanland and Clark* (1994).

*Dixon et al.* (2003) presented a 2D viscoelastic model for the Owens, Panamint, and Death Valley faults. They argued that the apparently high slip rate on the Owens Valley Fault was due to postseismic relaxation following the 1872 Owens Valley earthquake. Their model also required that the Death Valley fault zone slips at a geologic rate more than 8 mm/yr, but is very late in its earthquake cycle. Our block model shows that the high Owens Valley slip rate is not localized along the 1872 rupture zone. Instead, it extends along the entire Sierra Nevada range front. In order for postseismic relaxation to be responsible for this fast slip rate, there would have to be some 3D postseismic relaxation phenomena that can cause velocity gradients to localize along strike several fault lengths away from the coseismic rupture zone. An alternate explanation is that the present day slip rate is faster than the Holocene average.

Our slip rate estimate for the Calico - Blackwater - Landers structure is  $4.0 \pm 0.8$  mm/yr. This is not significantly lower than *Peltzer et al.'s* (2001) estimate of  $7 \pm 3$  mm/yr, and far above *Oskin's* (2002) estimate based on the offset of Pliocene lava flows. Thus, two different studies using different types of geodetic data and modelling approaches both suggest that the present day slip rate is greater than the 2 Myr average. It is hard to argue that postseismic deformation following the 1992 Landers earthquake is responsible for the apparently fast slip rate, as *Sauber et al.* (1994) found roughly the same total slip budget prior the coseismic rupture. *Rockwell et al.* (2000) estimated Holocene slip rates on the major structures near the Landers rupture and estimated that no single fault had a slip rate in excess of 1 mm/yr. However, many parallel geologic structures in the Mojave Desert may accommodate a small amount of deformation (e.g., *Petersen and Wesnousky*, 1994). While the InSAR data set used by *Peltzer et al.* (2001) is spatially dense enough to rule out this possibility, GPS data in the region are insufficient to do so.

In contrast to *Peltzer et al.* (2001), we find a very high slip rate on the Goldstone Fault to the east of the Blackwater ( $13.7 \pm 0.8$  mm/yr). GPS coverage in this area is exceedingly sparse and likely influenced by postseismic deformation following the 1999 Hector Mine earthquake. However, these caveats do not eliminate the need to accommodate more than 12 mm/yr of deformation across the Mojave. In our model, we chose to recognize the limits of the data coverage and simplify the geometry in this region by using three north-south trending vertical structures to accommodate all deformation.



The southern end of the ECSZ is defined by the Pinto Mountain fault. Our model shows left lateral slip and opening across most of its width. The  $9.7 \pm 1.0$  mm/yr opening rate is a result of the fast motion of the Goldstone fault to the north. It might be possible to minimize the amount of opening here by introducing a new connection from the ECSZ to the southern San Andreas Fault along a structure like the Hidden Springs Fault.

## 8. Discussion

For the segment of the SAF that ruptured during the 1857 Ft. Tejon earthquake (FTSAF), we find not only a variation in slip rate from 25 to 35 mm/yr but also a 25 km locking depth. The constraints on the locking depth are weak as FTSAF locking depths from 15-40 km fit the data well (figure 9). However, experiments with 2D models and synthetic data show that our FTSAF result is consistent with estimates from idealized experiments. There are three obvious interpretations of this rather deep locking depth. First is that it represents the actual seismogenic depth. This is consistent with the locking depths estimated by solving for the rupture depth necessary to yield the correct moment given the mapped surface slip distribution (*Sieh, 1978*). However, 25 km is well below the predicted depth of the brittle ductile transition (8 – 15 km) for a typical geotherm (e.g., *Kohlstedt et al., 1995*) and below the bottom of the seismogenic region inferred from seismicity for this fault (*Hauksson, 2000*). A second explanation would be that the locking depth is actually much shallower, but that variation in the elastic structure broadens the strain accumulation signal (e.g., *Hager et al., 1999*). For this to be the case

the shear modulus would have decrease with depth, the opposite of the behavior predicted by pressure effects and seismic observations. The third hypothesis is that this deep locking depth is indicative of viscoelastic deformation through the earthquake cycle (see appendix A). Specifically, the broad zone of deformation late in the earthquake cycle is manifest as a deep locking depth in our block model formulation, which implicitly assumes purely elastic strain accumulation driven by creep on down-dip extensions of the faults. *Savage and Lisowski (1998)* estimated a similarly deep locking depth on the Mojave segment of the SAF in a study of trilateration data. However, they also estimated that the slip rate across the SAF was in excess of 30 mm/yr. We find that the Mojave segment of the SAF is at least 5 mm/yr slower. These two results may be reconciled by noting that *Savage and Lisowski (1998)* only considered the SAF, and ignored the effects of deformation along the San Gabriel range front to the southwest. We estimate ~5 mm/yr on this structure and suggest that both this study and *Savage and Lisowski (1998)* found the correct total amount of relative motion across the San Gabriel transect. Though there are differences in the slip rate magnitudes, both studies agree that the inferred deep locking depth on the SAF suggests that it is late in its earthquake cycle. *Sieh et al., (1989)* estimated mean recurrence intervals of 200-300 years. Approximately 150 years have passed since the last major FTSAF earthquake so, in the absence of clustering, we are likely in the latter half of the FTSAF earthquake cycle. Our results suggest that the entire FTSAF is fit best by a 25 km locking depth, not just the Mojave segment.

Despite the fact that there is some indication of postseismic deformation, the success with which we have modeled the GPS velocities with an elastic model suggests

that the high viscosity (low  $\tau_0$ ) assumption may be appropriate. If the mean recurrence time for the SAF is 200-300 years (e.g., *Sieh et al.*, 1989), then for  $\tau_0 = 0.5$  we would estimate that the viscosity of the lower crust/upper mantle should be greater than  $2-3 \times 10^{19}$  Pa·s. It is possible that the Southern California velocity field looks like a steady state velocity field not because of the absence of viscoelastic deformation but because we are seeing the effects of averaging across all of the different rupture areas. This is not inconsistent with the observation that the viscoelastic seismic cycle model (e.g., *Savage*, 2000) looks very similar to steady state profiles approximately 40% of the way between events (figure 4). If this were the case, it would support the interpretation of our preferred 25 km locking depth, as physically realistic and not representative of viscoelastic deformation. Thus, we cannot reject the steady state assumption. It may be the case that only great earthquakes (e.g. Ft. Tejon) rupture to sufficient depths to generate a postseismic response (e.g., *Savage and Prescott*, 1978).

Our slip rate model for the Los Angeles and Ventura Basins differs from previous estimates for three reasons: data, geometry, and assumptions. First, we use a far larger data set than any previous study of the Transverse Ranges. However, we have also tried to follow *Bawden et al.* (2001) by being selective about what velocities are included near areas of known subsidence or uplift<sup>8</sup>. The three dimensional aspects of fault system geometry are also important. We include aspects of the three-dimensional fault system geometry, such as the effects of multiple dipping and interacting fault zones. In addition, the blocks rotate, introducing a component of motion absent from previous studies.

---

<sup>8</sup> <http://quake.wr.usgs.gov/research/deformation/modeling/socal/la.html>

Further, the block model uses both far and near field velocities to estimate fault slip rates. This is necessary near Los Angeles where so many blocks abut each other, making it difficult to deconvolve the overlapping effects of strain accumulation without a model. The far field velocities can help to sort out the superposition of strain rates and allow us to estimate fault slip rates more reliably. The most important reason that our results differ from previous studies is that we do not make *a priori* assumptions about the behavior of the rest of the Southern California Fault System. We estimate the slip rates on all of the structures in Southern California simultaneously. This allows us to produce an internally consistent slip rate model where the same type of data has been used to estimate the fault slip rates everywhere. In summary, our models of the Los Angeles and Ventura Basins differ from previous efforts by virtue of more accurate data, the addition of 3D fault system structure, and a reduction in *a priori* assumptions regarding slip rates.

Both the Owens Valley and Blackwater Faults have geodetically determined slip rates that are higher than previous geologic estimates. While some authors have suggested post seismic relaxation to explain the fast slip rate north of the Garlock (e.g., *Dixon et al.*, 2003) others have suggested that the Mojave Desert may currently be rapidly evolving (*Nur et al.* 1993a, b). The fact that present day slip rates appear relatively fast along the entire line of faults suggests that this fault system reorganization has not been localized to the Mojave but has propagated north through Owens Valley.

To the east of the Blackwater and Airport Lake Faults, we find that the Garlock moves left laterally at  $\sim 2$  mm/yr. Part of this segment cuts past Searle's Lake where *McGill and Sieh* (1993) estimated a slip rate of  $7 \pm 2$  mm/yr over the last 60,000 years.

It may be somewhat fortuitous that we recover left lateral motion on these segments of the Garlock. While the blocks to the north are well constrained by dense station coverage, there are far fewer stations to the south. Not only is the station density lower but there is also the possibility that a nontrivial amount of rapid postseismic deformation has been included in the station velocity estimates due to their proximity to the Landers and Hector Mine rupture zones. Our models suggest, like *Peltzer et al. (2001)*, that the Blackwater and Garlock faults are more and less active, respectively, than they have been in the recent past.

The low slip rate estimate on the San Bernadino segment of the SAF (SBSAF,  $6.6 \pm 0.9$  mm/yr.) is one of the more interesting block model results. Again, we're not the first to see this feature in geodetic data. *Bird and Rosenstock (1994)* as well as *Bird and Kong (1984)* found a low rate, though they preferred a rather high upper bound. *Potter (1997)* suggested that geologic slip rate estimates were too high to accurately model the geodetic data there.

Our low slip rate estimate differs from the geologic estimate of  $25 \pm 4$  mm/yr at the  $3\text{-}\sigma$  level (*Weldon and Sieh, 1985*). This remarkable difference is worth exploring. There are four possible arguments regarding the compatibility of these two slip rate estimates. Two of these question the validity of either slip rate estimate, while the other two entertain the possibility that both of the estimates are compatible with each other.

The first and second arguments are that either the block model or the geologic slip rate estimates are wrong. By testing the block model with higher slip rates forced on the San Bernadino segment, we can demonstrate that a high slip rate is grossly incompatible

with the geodetic data (figure 15). The residual velocities are larger with a resulting increase in the misfit criteria by 86%, even after minimizing the residual velocities as before. Further, the forced motion of the Mojave block leads to a Mojave SAF slip rate in excess of 45 mm/yr. Thus, a fast SBSAF is incompatible with the geodetic observations. The proximity of this area to the location of the 1992 Landers earthquake raises the question of whether or not the data in this area may not represent steady interseismic velocities. For this to be the effect controlling the slip rate results, the rapid postseismic decay would have to extend across the Mojave and Salton blocks, a distance of more than 150 km from the rupture zone. In total, the possibility of seismic cycle variations causing this result seems remote. *Weldon and Sieh's* (1985) slip rate estimate is robust, which leads us to the arguments for the compatibility of the two slip rate estimates.

The most obvious way in which the two rates could be compatible is if they are in different places. *Weldon and Sieh's* (1985) study area is Cajon Creek. We have chosen not to elongate the northern part of the Salton block into a small sliver that runs between the Mojave Desert and the San Gabriel Mountains. If the San Jacinto Fault reconnects with the SAF to the south of Cajon Creek then we get about the same slip rate as *Weldon and Sieh* (1985) but on the Mojave SAF. This would not eliminate the low slip rate area between the northern intersection of the SJF and SAF and the westernmost connection between the ECSZ and the SAF through the Eureka Peak fault

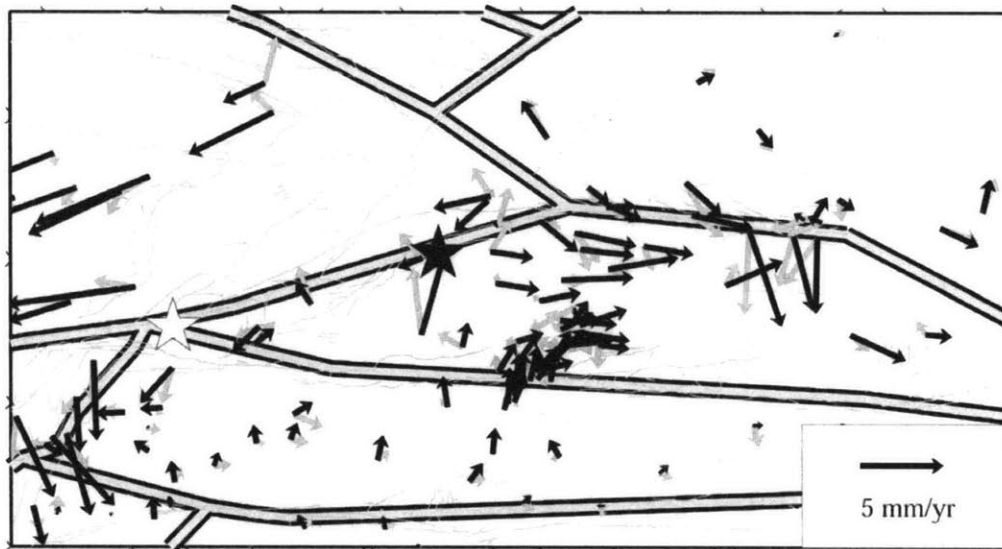


**Figure 15.** Residual velocities and fault system geometry along the San Bernardino segment of the San Andreas (SBSAF). The gray arrows are the residuals for our preferred model where there are no constraints on the SBSAF and the estimated right lateral slip rate is  $6.6 \pm 0.9$  mm/yr. The black arrows are the residuals when the SBSAF is forced to slip at 25 mm/yr. In the immediate vicinity of the fault, station density is low, and it is hard to evaluate the difference between the two models. Beyond the immediate vicinity of the SBSAF, the residual velocities near bordering segments are much larger (factor of 1-4) for the higher slip rate. The white and gray stars are the study areas from *Weldon and Sieh (1985)* and *Yule and Sieh (2000)*.

The other possibility that would permit the two geologic and geodetic estimates to be compatible with each other is that the slip rates in this area are changing rapidly enough to be different over the time scales that we are comparing. That is, the slip rate for the ten years that geodetic data have been gathered may be different from 14,000 year geologic rate. This would require that the SBSAF has decelerated over the last 5000 years. If the SBSAF were slowing down, it would require that another structure accelerate to accommodate the total slip budget across the SCFS. *Sharp (1980)*

suggested that the San Jacinto fault showed evidence not only for a 12 mm/yr slip rate through the latter half of the Quaternary, but also for acceleration in the latter half of the Holocene. If the both the SJF to the west and the faults in the ECSZ to the east were accelerating over the last 5000 years, then this could balance the deceleration of the SBSAF.

If the San Bernadino segment of the San Andreas Fault is moving at less than 10 mm/yr, there are direct implications for seismic hazard potential. The slower a fault slips, the longer it will take to accumulate a given amount of elastic strain. If earthquakes occur quasi-periodically, this would imply a longer recurrence interval. *Yule and Sieh* (2000) reported ~330 year long interevent times here, and suggested that this may be evidence for very large earthquakes. We suggest that the low slip rate provides an alternate explanation for the long interevent times. Using a simple characteristic earthquake model, we can estimate the size of a typical earthquake that might occur here. Using the empirical earthquake scaling relations from *Wells and Coppersmith* (1994), we can relate event size to characteristic slip without assuming a value for the rupture area. Further, if we assume that an earthquake will occur whenever enough strain has accumulated to generate a characteristic event, then we can relate slip rate and recurrence interval to moment magnitude,  $M_w$ . In figure 17 we see that for a  $6.6 \pm 0.9$  mm/yr slip rate and a mean recurrence interval of ~330 years (*Yule and Sieh*, 2000) a typical earthquake is about  $M_w = 7.40_{-0.05}^{+0.04}$ . With an empirical slip rate uncertainty of  $\pm 3$  mm/yr we find a larger moment magnitude range  $M_w = 7.40_{-0.37}^{+0.23}$ . These calculations ignore the



uncertainties is the empirical scaling relations. With both the slope and offset uncertainties the moment magnitude ranges from below 6 to greater than 8.

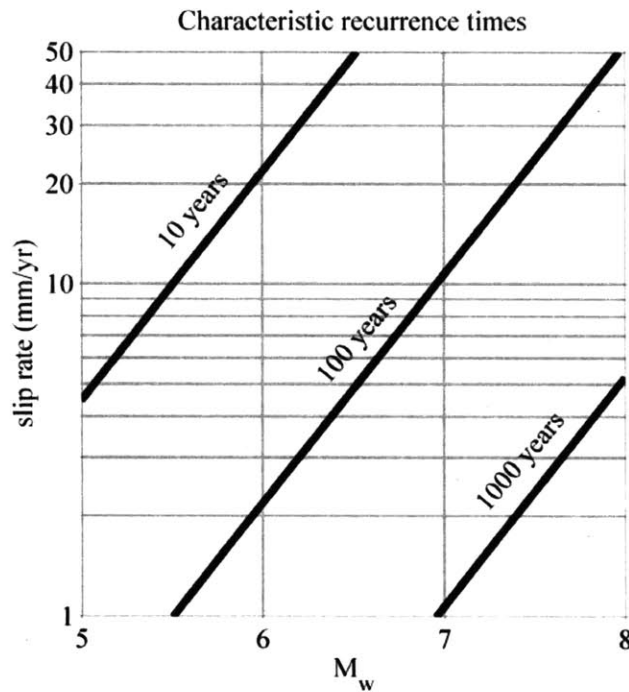


**Figure 16.** Relationship between moment magnitude,  $M_w$ , slip rate and earthquake recurrence time for an ideal earthquake cycle. The recurrence time multiplied by the slip rate gives the coseismic slip. The relationship between coseismic slip and moment magnitude was taken from *Wells and Coppersmith* (1994).

## 9. Conclusions

The distribution of slip across the Southern California fault system is one of the most basic pieces of information required to understand both regional tectonics and seismic hazard potential. Block modeling provides a framework that allows us to combine both plate motion (Euler pole rotation) and near-fault deformation (elastic strain

accumulation) effects. With the block model formulation presented in this paper, we have simultaneously estimated motions of 22 blocks, which gives slip rate estimates on about 40 major structures bounding these blocks. The residual velocity field (figure 10) shows how successfully this approach can reproduce the first order features of the observed velocity field (figure 5). The residual velocity field is interesting not only for demonstrating how successful the block model has been but also for localizing regions where more sophisticated models may be appropriate.

We find that the San Andreas Fault has an along-strike variation in slip rate of nearly a factor of five (table 1), from  $\sim 35$  mm/yr at the Parkfield to less than 7 mm/yr along the SBSAF. This enormous variation in slip rate forces us to reconsider seismic hazard, the relationship between paleoseismology and geodesy, and fault system evolution. We infer a 25 km locking depth for the Ft. Tejon segment of the SAF. While the interpretation of the deep locking depth is ambiguous, it may be an indicator that the SAF is late in its seismic cycle.

While the SBSAF is relatively slow, the SJF and the faults in the ECSZ make up for the bulk of the “missing” slip between the Pacific and North American Plates (PA-NA). Geodetic data constrain the SJF slip rate at  $\sim 14$  mm/yr. As it is even closer to metropolitan Los Angeles than is the SAF, the SJF may represent an even greater seismic hazard than the SBSAF. Of the faults in the ECSZ that make up the rest of the PA-NA plate motion, we find that the Blackwater and Goldstone faults are the most active. This result may be skewed by the presence of short-term postseismic relaxation data in the SCEC3.0 CMM. The observation that the fault slip rates inferred from the block model

along the Owens Valley – Blackwater system are systematically high lead support to the hypothesis that we are currently observing ongoing, or very recent, evolution of the ECSZ, if not the entire SCFS. The slip rates on the SBSAF and the SJF also support this model and provide time constraints pointing toward fault system reorganization in the latter half of the Holocene.

The distribution of deformation in and around the Los Angeles basin has been the subject of much interest due to the possibility of high seismic hazard. We find evidence for shortening along the southern San Gabriel range front and the northern Ventura basin, ranging from 0.5 to 13.5 mm/yr. We also find evidence for ~2 mm/yr of shortening on the Puente Hills Thrust underneath metropolitan Los Angeles. The offshore fault system also accommodates at least 5 mm/yr of strike slip motion but it is difficult to constrain rigorously due to the lack of offshore geodesy.

Our results differ from previous studies not only because of better data and but, more importantly, because we are able to estimate the slip rates on all of these structures simultaneously. The block model slip rate catalog is consistent with geodetic observations of interseismic deformation, a simple model of the earthquake cycle, and is kinematically compatible to plate motions. We can compare this catalog with that derived from geologic data, to more quantitatively evaluate both the regional seismic hazard and the evolution of the Southern California Fault System.

### Appendix A. Elastic models of viscoelastic data

To explore how viscoelastic deformation might be mapped into slip rate and locking depth estimates in a purely elastic model, we study the behavior of simple two-dimensional system. We evaluate the fault parallel velocities predicted by *Savage's* (2000) viscoelastic model at various times through the earthquake cycle, then use these velocity profiles to estimate slip rates and locking depths in a purely elastic model. The elastic model we use is,  $v = v_0 \pi^{-1} \tan^{-1}(x/D)$ , where  $v$  is the fault parallel velocity at a distance  $x$  from the fault,  $v_0$  is the long-term slip rate, and  $D$  is the locking depth. Using a nonlinear estimator, we find the apparent elastic slip rate  $v_0^E$  and locking depth  $D^E$  given  $v = v_s(x, D, t/T, \tau_0)$ , where  $v_s$  is the velocity from *Savage's* (2000) model. Figure 17 shows time series predicted from the *Savage and Prescott* (1978) and *Savage* (2000) model with  $\tau_0 \approx 5$ . The time dependent variation is greatest near the fault. All of the velocities slow as the next earthquake approaches.

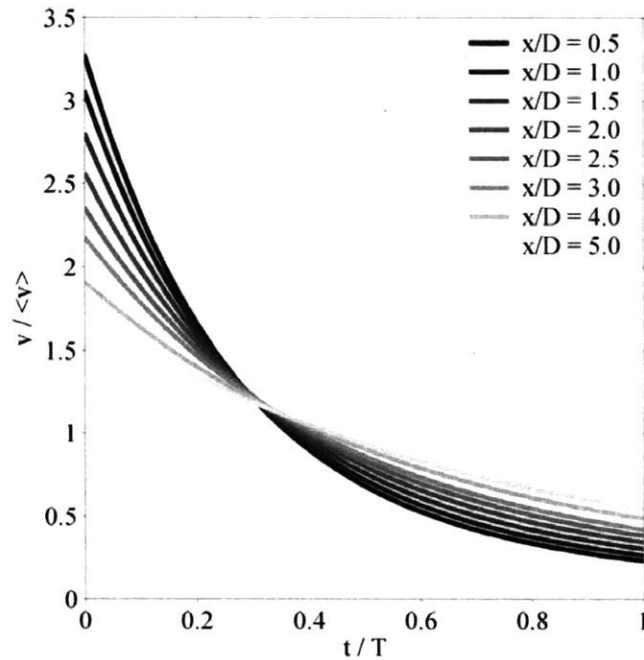


**Figure 17.** Synthetic velocity time series from the *Savage and Prescott* (1978) and *Savage* (2000) model. All of the velocities are normalized by the steady state values.

We'll consider the slip rates for both fixed and free locking depths,  $D^E$ . The viscoelastic model we employ is sensitive to the parameter  $\tau_0$  (e.g., *Savage*, 2000). We set  $\tau_0 \approx 5$ , corresponding to an earthquake repeat time of  $T = 1000$  years and a dynamic viscosity  $\eta = 10^{20}$  Pa·s. We'll carry out two different inversions. First, we estimate both the slip rate and the locking depth, and second where we fix the locking depth at the true value and estimate the slip rate. The difference between the two estimates highlights the ambiguity involved in interpreting fault locking depths based on geodesy alone.

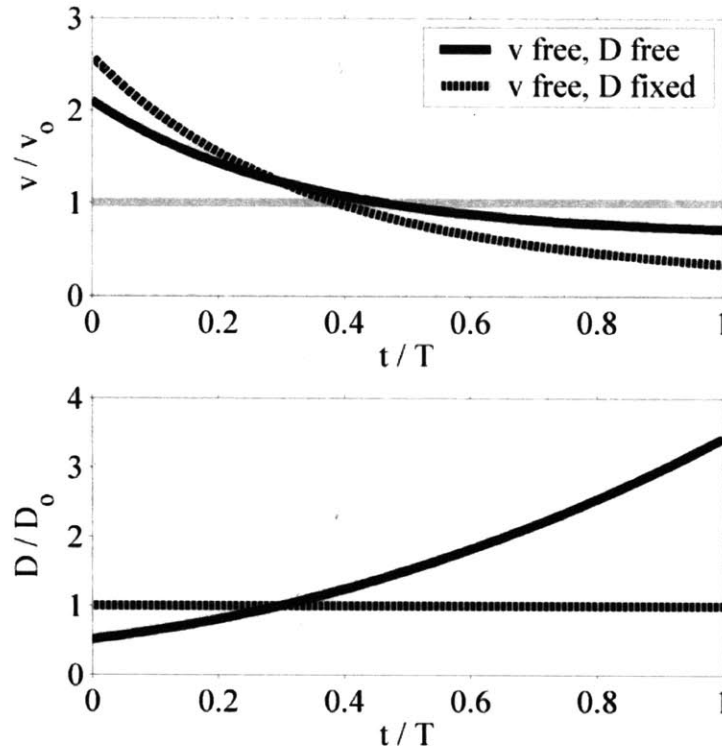


**Figure 18.** Estimated elastic parameters. The upper panel shows the slip rates estimated from an elastic model while the lower panel gives the fault locking depth estimates. The solid, dashed, and gray lines represent the free locking depth, fixed locking depth and reference lines respectively. The time through the earthquake cycle is parameterized as  $t/T$  and ranges from zero to one. In general, apparent slip rates decrease through the earthquake cycle and locking depths increase. Deeper locking depths appear late in the earthquake cycle.

The upper panel of figure 18 shows the estimated slip rates. Early in the earthquake cycle, we find high estimated elastic slip rates relative to the long-term value. Approximately 40% of the way through the cycle the apparent rate drops below the long-term rate. For the case where the locking depth is the estimated slip rate can drop well below the long-term value (~30%). The lower panel (figure 18) shows the estimated locking depths. Early in the earthquake cycle, we find locking depths approximately

50% of the true value while late in the cycle we see much deeper locking depths - up to three times the actual locking depth. These experiments provide a quantitative foundation for the argument that apparently deep estimated locking depths (from an elastic model) may be an indication that we are currently observing activity late in the seismic cycle.

**Appendix B: Observed velocities**

The merged and cleaned observed GPS velocities are shown in the table below.

<b>Longitude (degrees)</b>	<b>Latitude (degrees)</b>	<b>East vel. (mm/yr)</b>	<b>North vel. (mm/yr)</b>	<b>East sig. (mm/yr)</b>	<b>North sig. (mm/yr)</b>	<b>Correlation</b>	<b>Name</b>
243.839	31.257	-30.90	31.42	0.92	0.91	-0.065	LLCO_GPS
244.534	31.045	-31.25	30.00	1.04	1.05	-0.050	SPMX_GPS
243.333	31.871	-28.69	30.50	0.98	0.99	-0.056	CICE_GPS
246.480	31.354	-1.51	1.73	0.83	0.81	-0.077	PENA_GPS
244.757	31.988	-24.01	26.93	1.21	1.12	0.093	MAYR_GPS
241.512	32.914	-30.71	33.12	0.97	0.99	-0.054	SCIP_GPS
241.481	32.927	-29.64	34.88	0.88	0.91	-0.071	BLUF_GPS
240.521	33.232	-30.20	35.05	0.89	0.91	-0.072	TWIN_GPS
240.476	33.248	-31.16	34.61	0.91	0.94	-0.062	SN11_GPS
241.595	33.407	-28.54	33.34	0.86	0.92	-0.061	BRSH_GPS
240.959	33.472	-30.53	34.67	0.93	0.98	-0.061	SBIS_GPS
241.517	33.446	-28.96	32.61	0.88	0.91	-0.063	CAT1_GPS
239.894	33.951	-30.23	35.58	0.94	0.93	-0.039	SNRI_GPS
240.247	33.995	-29.18	33.91	0.92	0.92	-0.057	CENT_GPS
240.216	34.029	-30.17	35.10	1.04	1.01	-0.003	DEVL_GPS
241.664	33.747	-25.04	33.06	1.08	1.22	-0.024	PVOO_GPS
241.706	33.713	-27.79	30.31	1.02	1.05	-0.044	VTIS_GPS
241.727	33.720	-28.10	29.93	1.07	1.12	-0.039	TID8_GPS
241.628	33.779	-27.02	29.30	1.12	1.14	-0.037	PVHS_GPS
241.679	33.774	-28.57	29.29	1.08	1.12	-0.042	PVRS_GPS
241.647	33.797	-27.20	33.40	1.02	1.02	-0.042	SPJ1_GPS
241.669	33.798	-27.80	29.94	0.91	0.94	-0.055	TORP_GPS
241.727	33.824	-25.95	28.86	1.12	1.14	-0.034	CRHS_GPS
241.671	33.887	-26.75	28.99	1.09	1.12	-0.039	ECCO_GPS
241.784	33.868	-25.89	29.00	1.18	1.19	-0.091	56_Z_GPS
241.572	33.958	-27.14	27.85	1.16	1.18	-0.042	WRHS_GPS
241.693	33.928	-27.71	26.46	1.01	1.03	-0.045	LASC_GPS
241.825	33.930	-27.37	28.08	0.97	1.01	-0.069	HOLY_GPS
241.820	33.951	-26.13	27.75	1.43	1.47	-0.043	07CI_GPS
240.846	34.120	-28.34	32.98	1.03	0.98	-0.032	COTR_GPS
241.170	34.157	-28.53	29.84	0.86	0.89	-0.061	AOA1_GPS
241.298	34.033	-27.69	31.60	1.30	1.38	-0.067	6022_GPS
241.214	34.086	-28.94	30.27	1.21	1.04	-0.082	CATO_GPS
241.354	34.059	-27.88	29.42	0.87	0.90	-0.059	SPK1_GPS
241.486	34.060	-27.69	29.83	1.08	1.17	-0.056	WIRO_GPS
241.405	34.063	-27.27	30.86	0.96	0.99	-0.049	TUNA_GPS
241.502	34.090	-28.35	29.90	1.09	1.16	-0.015	MAND_GPS



241.581	33.972	-28.20	31.80	1.27	1.33	-0.012	VENI_GPS
241.597	33.996	-27.94	30.77	1.49	1.08	-0.009	0701_GPS
241.558	34.069	-26.58	27.32	0.86	0.89	-0.060	UCLP_GPS
241.829	34.063	-25.96	23.95	1.50	1.45	0.040	07DI_GPS
241.797	34.085	-24.88	25.77	1.16	1.07	-0.034	JEFF_GPS
241.239	34.146	-27.52	32.40	1.22	1.28	-0.041	0094_GPS
241.446	34.102	-26.83	32.21	1.11	1.13	-0.030	DIVI_GPS
241.354	34.140	-27.42	32.82	0.96	0.98	-0.054	CALA_GPS
241.370	34.139	-27.50	28.69	1.06	1.08	-0.040	CBHS_GPS
241.440	34.130	-26.03	32.50	1.31	1.25	-0.028	MULH_GPS
241.487	34.129	-26.61	30.11	1.07	1.08	-0.043	NIKE_GPS
241.425	34.182	-26.37	28.08	1.13	1.15	-0.033	LAPC_GPS
241.438	34.179	-26.14	30.42	0.99	1.00	-0.044	OXCO_GPS
241.457	34.202	-25.85	30.02	0.99	1.00	-0.043	MCDS_GPS
241.587	34.095	-28.26	25.89	1.08	1.11	-0.040	LFRS_GPS
241.678	34.135	-26.88	25.44	0.86	0.89	-0.059	LEEP_GPS
241.717	34.161	-27.09	26.06	1.17	1.16	-0.015	GLEN_GPS
241.793	34.129	-26.55	24.07	1.15	1.17	-0.034	OXYC_GPS
241.873	34.137	-25.38	24.20	0.84	0.87	-0.061	CIT1_GPS
241.627	34.222	-26.18	25.81	1.30	1.33	-0.042	Z786_GPS
241.723	34.185	-26.50	24.11	0.86	0.89	-0.060	BRAN_GPS
241.720	34.215	-25.05	25.82	1.31	1.26	0.000	VDGO_GPS
241.827	34.205	-25.51	23.66	0.84	0.87	-0.061	JPLM_GJP
243.017	32.569	-27.07	29.72	1.05	1.19	-0.064	1101_GPS
243.159	32.601	-25.69	28.82	1.48	1.21	-0.068	OTAY_GPS
243.442	32.245	-27.39	29.05	1.08	1.10	-0.040	VA01_GPS
243.523	32.607	-26.96	28.66	1.03	1.12	-0.061	1102_GPS
244.657	32.356	-18.65	27.00	0.89	0.89	-0.058	LPUR_GPS
242.852	32.818	-28.20	28.82	1.20	1.50	-0.031	SD17_GPS
242.747	32.840	-27.26	29.75	1.11	1.09	-0.044	SOLJ_GPS
242.750	32.865	-27.40	28.21	0.73	0.76	-0.093	SIO3_GPS
243.198	32.844	-27.01	28.20	0.96	1.04	-0.075	1106_GPS
243.069	32.912	-27.24	29.47	1.03	1.14	-0.043	SD18_GPS
242.723	33.130	-28.16	29.78	1.01	1.11	-0.088	1107_GPS
243.381	32.824	-26.27	28.05	0.95	1.03	-0.057	SD21_GPS
243.998	32.734	-27.04	28.00	0.97	0.96	-0.061	OCTI_GPS
244.494	32.664	-20.11	26.01	1.09	1.07	-0.025	BORD_GPS
244.500	32.738	-20.11	20.38	0.92	0.93	-0.060	T124_GPS
244.204	32.790	-23.78	26.77	0.91	0.91	-0.052	OCOT_GPS
244.406	32.800	-16.10	21.76	1.32	1.16	-0.007	E122_GPS
244.498	32.827	-13.39	19.53	0.97	0.94	-0.059	COLL_GPS
243.429	32.914	-28.61	28.40	1.08	1.18	-0.071	SD35_GPS
243.578	32.892	-26.92	27.57	0.79	0.81	-0.077	MONP_GPS
243.915	33.030	-22.06	23.89	1.10	1.12	-0.038	USGC_GPS
244.594	32.917	-2.27	4.20	0.95	0.91	-0.063	ORIE_GPS

244.265	33.070	-13.31	17.69	1.02	1.03	-0.045	CRRS_GPS
245.086	32.251	-7.70	7.38	1.12	1.13	-0.018	CPEI_GPS
244.925	32.559	-5.49	1.17	1.10	1.12	-0.020	MONT_GPS
244.938	32.709	-2.92	2.23	1.05	0.99	-0.052	JUNC_GPS
244.968	32.706	-2.10	0.99	1.10	1.12	-0.038	IID2_GPS
244.753	32.840	-3.46	-0.65	0.92	0.88	-0.067	GLOC_GPS
245.797	32.939	-0.56	2.67	1.04	0.96	-0.044	YUMA_GPS
242.435	33.375	-26.59	29.55	0.97	1.02	-0.059	0301_GPS
242.841	33.332	-25.67	28.90	1.26	1.44	-0.054	0303_GPS
243.140	33.357	-24.62	26.65	1.00	1.02	-0.047	PMOB_GPS
242.365	33.444	-27.89	30.64	1.02	1.04	-0.047	SCMS_GPS
242.291	33.464	-27.29	30.50	0.95	0.98	-0.069	DANA_GPS
242.320	33.469	-26.95	29.42	0.94	0.96	-0.061	1202_GPS
242.270	33.514	-27.07	30.69	0.86	0.87	-0.073	NIGU_GPS
242.284	33.554	-27.44	30.24	1.08	0.99	-0.032	KITE_GPS
242.197	33.618	-25.33	29.01	0.85	0.88	-0.064	TRAK_GPS
242.855	33.430	-26.31	27.20	0.98	1.04	-0.050	YUNG_GPS
242.811	33.505	-24.77	27.83	1.16	1.15	-0.028	ROSA_GLA
243.068	33.468	-23.48	26.68	1.16	1.25	-0.047	RDEC_GPS
243.164	33.484	-23.17	26.85	1.08	1.14	-0.087	A586_GPS
243.265	33.545	-21.04	25.43	1.01	1.06	-0.047	CARY_GPS
242.645	33.620	-24.69	27.92	1.15	1.24	-0.100	LAKE_GPS
242.914	33.636	-22.71	26.88	1.03	1.07	-0.055	DASH_GPS
243.152	33.630	-21.42	26.04	1.05	1.12	-0.043	R293_GPS
243.475	33.211	-23.95	26.15	1.08	1.10	-0.039	MVFD_GPS
243.307	33.234	-25.82	26.98	1.01	1.10	-0.101	1108_GPS
243.753	33.160	-22.53	23.99	0.94	1.03	-0.054	1109_GPS
243.297	33.382	-24.22	26.90	0.96	1.00	-0.067	SDG6_GPS
244.112	33.177	-14.21	15.92	0.94	0.97	-0.066	1110_GPS
244.593	33.196	-2.19	2.76	1.05	0.98	-0.053	COAC_GPS
244.481	33.231	-4.10	1.06	1.04	1.03	-0.065	1111_GPS
244.212	33.390	-10.88	9.55	0.86	0.88	-0.060	DHLG_GPS
244.248	33.412	-9.60	7.85	1.19	1.22	-0.027	07NE_GPS
243.299	33.543	-20.86	24.57	0.97	0.99	-0.045	CRAV_GPS
243.283	33.550	-21.00	25.50	0.98	1.02	-0.056	HOWY_GPS
243.411	33.527	-19.38	23.58	1.01	1.05	-0.042	TBLM_GPS
243.387	33.550	-18.30	23.26	1.04	1.08	-0.059	G114_GPS
243.426	33.553	-18.15	21.78	0.90	0.93	-0.052	LOKT_GPS
243.574	33.524	-17.09	18.76	0.91	0.94	-0.054	TORO_GPS
243.939	33.441	-11.42	16.57	1.05	1.05	-0.030	ROBO_GPS
243.311	33.555	-20.13	25.14	1.15	1.18	-0.054	M586_GPS
243.338	33.556	-19.95	24.51	0.89	0.91	-0.058	ANZA_GLA
243.369	33.558	-19.11	23.66	1.01	1.03	-0.043	ANZC_GPS
243.397	33.565	-18.93	23.11	1.16	1.20	-0.038	G120_GPS
243.404	33.568	-17.91	22.57	1.05	1.08	-0.023	RCUT_GPS

243.442	33.562	-16.29	22.26	1.25	1.33	-0.017	G128_GPS
243.417	33.565	-19.34	22.07	1.18	1.22	-0.024	G124_GPS
243.320	33.619	-18.25	22.91	0.99	1.06	-0.070	TOME_GLA
243.390	33.611	-17.45	22.27	0.81	0.83	-0.067	ROCH_GLA
243.483	33.571	-17.16	21.89	1.01	1.05	-0.035	PMCN_GPS
243.502	33.571	-15.80	19.52	1.17	1.21	-0.028	D138_GPS
243.516	33.581	-15.88	19.02	1.02	1.07	-0.051	PF6_GLA
243.553	33.574	-15.73	18.06	1.12	1.14	-0.060	GREN_GPS
243.570	33.584	-14.79	19.11	0.96	1.00	-0.061	PF1_GPS
243.523	33.603	-15.51	20.23	1.18	1.15	-0.022	PF5C_GPS
243.542	33.612	-15.57	19.16	0.80	0.82	-0.068	PIN1_GLA
243.538	33.620	-14.88	18.13	0.94	1.00	-0.066	ASBS_GPS
243.562	33.599	-15.94	20.71	1.17	1.18	-0.037	BNDY_GPS
243.410	33.646	-16.59	20.62	0.94	0.95	-0.055	JOES_GPS
243.589	33.623	-17.25	19.49	1.43	1.41	-0.029	L587_GPS
243.528	33.684	-14.19	19.29	0.97	0.97	-0.053	WHAY_GPS
243.609	33.688	-12.25	17.21	0.97	1.00	-0.057	RSRT_GPS
243.726	33.639	-11.86	15.53	1.05	1.08	-0.054	CAHU_GPS
243.840	33.628	-11.29	12.88	1.28	1.19	-0.012	VORO_GPS
244.167	33.429	-10.56	9.10	0.97	0.98	-0.038	TRAN_GPS
244.230	33.427	-7.74	7.99	1.30	1.27	0.008	S_31_GPS
244.217	33.441	-9.64	8.33	1.07	1.12	-0.047	25SE_GPS
244.322	33.427	-6.11	3.14	0.92	0.94	-0.046	SIPH_GPS
244.086	33.503	-11.45	7.55	1.06	1.02	-0.049	VARN_GPS
243.992	33.612	-8.16	7.30	1.05	1.07	-0.035	PAIN_GPS
244.036	33.677	-6.26	4.24	1.18	1.38	-0.065	1113_GPS
244.280	33.664	-3.35	1.47	0.86	0.88	-0.059	BLAC_GLA
241.912	33.737	-25.39	30.00	1.31	1.00	-0.024	1201_GPS
242.091	33.748	-26.14	29.52	1.09	1.23	-0.056	FIFT_GPS
241.957	33.774	-26.67	29.05	0.94	1.00	-0.054	FLOO_GPS
242.058	33.793	-26.99	28.09	1.00	1.02	-0.058	LASE_GPS
242.135	33.863	-25.58	25.35	1.04	1.07	-0.042	CCCS_GPS
241.945	33.917	-25.66	25.71	0.94	0.96	-0.054	LANW_GPS
242.347	33.849	-24.44	27.10	0.94	0.95	-0.064	SIER_GPS
242.402	33.847	-24.54	26.37	0.92	0.96	-0.058	OAKD_GPS
242.563	33.857	-23.12	25.54	0.82	0.85	-0.066	MATH_GPS
242.453	33.884	-23.89	26.09	0.93	0.96	-0.056	0819_GPS
242.262	33.914	-24.91	25.91	0.86	0.88	-0.061	SJUA_GPS
242.768	33.796	-22.27	25.46	1.17	1.12	-0.042	METZ_GLA
243.223	33.794	-14.13	23.02	1.03	1.06	-0.052	INDO_GLA
242.691	33.837	-22.67	25.85	0.97	1.07	-0.063	LAST_GLA
242.818	33.836	-21.21	23.99	1.02	1.04	-0.042	PPBF_GPS
241.997	33.992	-24.39	24.84	0.94	1.03	-0.043	WORK_GPS
242.151	33.993	-24.54	25.92	0.99	1.01	-0.046	SPMS_GPS
241.891	34.089	-23.59	24.04	1.19	1.21	-0.030	SGHS_GPS

242.000	34.078	-27.69	24.55	1.06	1.06	-0.026	0702_GPS
242.117	34.042	-25.83	23.34	1.08	1.11	-0.048	SNT0_GPS
242.451	33.975	-23.54	25.59	1.11	1.14	-0.102	LIMP_GPS
242.487	34.018	-22.05	24.14	1.02	1.05	-0.063	SANO_GPS
242.557	34.032	-22.44	24.27	0.92	0.93	-0.061	JUR3_GPS
242.470	34.077	-22.68	25.27	1.17	1.20	-0.065	STEE_GPS
242.104	34.126	-25.79	23.45	0.90	0.93	-0.057	AZU1_GPS
241.945	34.225	-25.09	22.51	0.96	0.96	-0.072	ECRK_GPS
242.311	34.121	-23.31	22.19	1.07	1.11	-0.049	PSEB_GPS
242.246	34.133	-23.95	22.89	1.10	1.12	-0.035	LORS_GPS
242.274	34.137	-23.72	21.07	1.21	1.20	-0.015	VERN_GPS
242.395	34.172	-22.00	22.74	1.21	1.24	-0.117	ANGA_GPS
242.234	34.222	-23.80	19.59	1.32	1.31	-0.014	CAMP_GPS
242.496	34.212	-20.14	20.15	1.08	1.09	-0.035	SANS_GPS
242.861	34.014	-16.36	20.81	0.94	0.99	-0.058	BRI2_GLA
242.896	34.022	-16.99	20.17	1.08	1.11	-0.054	0818_GPS
242.647	34.089	-21.40	21.84	0.96	0.99	-0.046	RTHS_GPS
242.900	34.039	-18.20	19.60	0.83	0.86	-0.062	CRFP_GPS
243.048	34.003	-14.23	20.32	1.09	1.10	-0.025	CHER_GLA
243.288	33.714	-17.45	22.00	0.96	1.00	-0.066	WD91_GLA
243.467	33.776	-13.16	18.48	1.11	1.15	-0.007	BOTR_GPS
243.701	33.714	-11.93	15.42	0.93	0.94	-0.059	PTHP_GPS
243.719	33.750	-10.36	13.64	1.06	1.05	-0.048	DUNP_GPS
243.842	33.740	-8.59	9.19	0.99	1.02	-0.047	COCH_GLA
243.829	33.749	-7.98	9.96	0.97	0.99	-0.047	GAPP_GLA
243.669	33.817	-9.30	15.09	1.36	1.36	-0.015	RMRD_GLA
243.825	33.810	-6.67	7.80	1.05	1.05	-0.034	BERD_GPS
243.511	33.839	-10.26	17.87	1.14	1.18	0.001	PSAR_GPS
243.569	33.870	-9.50	17.72	0.92	0.94	-0.052	EDOM_GLA
243.358	33.925	-13.17	19.17	1.17	1.25	-0.060	TOM2_GLA
243.594	33.931	-9.70	16.01	1.19	1.21	-0.014	WIDE_GLA
243.608	33.935	-9.81	17.53	0.93	0.95	-0.049	WIDC_GPS
243.827	33.952	-3.92	9.17	1.28	1.35	-0.002	PBB4_GPS
244.600	33.715	-1.26	0.81	1.03	0.96	-0.044	DESO_GPS
244.236	33.834	-1.12	2.52	1.13	1.13	-0.006	JTRE_GPS
244.757	33.681	-2.74	1.35	1.24	1.06	-0.051	1114_GPS
245.285	33.610	-2.00	1.11	0.80	0.81	-0.066	BLYT_GPS
244.855	34.158	-0.66	-0.68	1.09	1.11	-0.032	IMPS_GPS
245.519	34.044	-0.15	0.92	1.21	0.99	-0.031	ENDD_GPS
239.318	34.469	-32.26	33.62	0.85	0.90	-0.062	HARV_GPS
240.286	34.494	-30.20	29.96	0.96	0.96	-0.047	LACU_GPS
240.280	34.500	-29.22	30.94	1.02	1.05	-0.045	RCAG_GPS
239.384	34.556	-31.28	34.43	0.84	0.89	-0.063	VNDP_GPS
239.373	34.571	-29.25	36.17	1.32	1.23	-0.031	RUS1_GPS
239.383	34.593	-30.61	34.94	1.35	1.23	-0.037	ALVA_GPS

239.721	34.739	-31.45	33.06	1.13	1.16	-0.033	ORES_GPS
239.801	34.502	-29.35	32.66	1.03	0.98	-0.031	GAVI_GPS
240.657	34.298	-30.13	28.63	0.96	0.93	-0.033	SOLI_GPS
240.669	34.301	-28.76	27.84	1.10	0.99	-0.009	CHAF_GPS
241.163	34.248	-28.30	28.76	1.10	1.13	-0.035	TOST_GPS
241.122	34.295	-28.41	28.80	1.11	1.13	-0.035	MPWD_GPS
240.877	34.306	-27.20	29.06	1.13	1.09	-0.035	W304_GPS
240.858	34.327	-28.17	29.20	1.12	1.14	-0.041	OVLS_GPS
240.961	34.326	-29.62	30.16	0.99	0.94	-0.079	SCLA_GPS
241.123	34.328	-30.44	29.70	1.07	1.11	-0.038	HAP2_GPS
241.150	34.358	-30.21	29.95	1.28	1.11	-0.070	HAPY_GPS
240.798	34.440	-33.26	29.03	1.05	1.06	-0.041	OJAI_GPS
241.001	34.388	-27.86	26.91	0.92	0.93	-0.060	SNPA_GPS
241.060	34.394	-32.20	27.08	1.32	1.23	0.016	0706_GPS
240.990	34.440	-28.81	25.82	1.26	1.28	-0.051	SNP2_GPS
241.101	34.433	-28.35	24.96	1.08	1.10	-0.036	RCKS_GPS
241.134	34.478	-24.77	24.12	0.99	0.94	-0.064	HOPP_GPS
241.324	34.236	-26.89	29.88	0.88	0.91	-0.056	ROCK_GPS
241.330	34.279	-29.16	29.14	1.12	1.11	-0.011	CHRN_GPS
241.359	34.257	-27.22	29.48	0.84	0.87	-0.062	CHT3_GPS
241.445	34.233	-26.08	29.21	0.94	0.96	-0.051	NORT_GPS
241.476	34.254	-26.41	25.94	0.90	0.93	-0.054	CSN1_GPS
241.489	34.258	-24.40	26.06	1.11	1.16	-0.019	DELO_GPS
241.512	34.292	-23.94	24.23	0.91	0.93	-0.053	RESE_GPS
241.399	34.331	-27.45	25.74	0.81	0.84	-0.065	PICO_GNR
241.592	34.264	-24.77	26.10	0.99	1.01	-0.048	PACO_GPS
241.846	34.286	-20.73	22.71	1.16	1.16	-0.027	JSPH_GPS
241.589	34.353	-25.71	24.04	0.87	0.90	-0.057	CMP9_GPS
241.307	34.406	-28.33	26.77	1.09	1.19	-0.074	U145_GPS
241.460	34.407	-25.32	22.18	0.93	0.93	-0.050	0704_GPS
241.331	34.496	-24.03	21.22	1.00	0.96	-0.067	LOVE_GPS
241.682	34.386	-24.86	22.57	1.23	1.27	0.011	MAGI_GPS
241.815	34.387	-23.76	22.49	0.97	0.99	-0.027	GLSN_GPS
240.736	34.566	-29.01	24.84	1.29	1.17	0.052	0102_GPS
240.700	34.636	-27.18	23.99	0.97	0.95	-0.046	MUNS_GPS
240.645	34.683	-28.98	23.77	1.36	1.31	-0.041	OZNA_GPS
240.900	34.641	-24.88	22.36	1.05	1.07	-0.061	TWST_GPS
240.896	34.734	-24.24	20.55	1.14	1.17	-0.032	LVMS_GPS
241.390	34.515	-26.26	20.28	1.17	1.19	-0.035	FHFF_GPS
241.348	34.544	-23.05	19.80	1.47	1.46	-0.155	Z370_GPS
241.745	34.503	-23.44	22.89	1.10	1.14	-0.019	0048_GPS
241.755	34.629	-18.63	18.91	1.15	1.17	-0.029	QHTP_GPS
241.210	34.688	-22.64	20.24	1.31	1.36	-0.104	WARN_GPS
241.257	34.751	-21.38	18.17	1.09	1.15	-0.038	AIRR_GPS
241.854	34.754	-13.44	16.51	1.20	1.10	0.045	0027_GPS

239.394	34.894	-30.32	34.75	0.97	0.96	-0.042	LOSP_GPS
239.743	34.798	-30.63	34.29	1.26	1.16	-0.036	LAMO_GPS
240.286	34.823	-28.00	29.22	0.89	0.92	-0.057	SALI_GPS
240.162	35.003	-26.94	28.24	0.98	1.00	-0.049	0504_GPS
240.240	35.036	-25.45	25.40	0.89	0.92	-0.044	LGO7_GPS
239.933	35.076	-27.07	30.18	0.94	0.93	-0.052	MADC_GPS
240.516	34.852	-24.83	24.61	1.04	0.98	-0.046	YAM2_GPS
241.107	34.800	-20.47	19.53	1.01	1.03	-0.040	FZHS_GPS
241.132	34.825	-20.02	18.50	1.00	1.09	-0.063	0618_GPS
240.511	34.928	-23.23	22.88	1.20	1.14	-0.116	CUYA_GPS
240.568	34.960	-20.77	20.70	0.90	0.91	-0.054	PATW_GPS
240.821	35.002	-14.98	17.15	1.07	1.10	-0.051	J976_GPS
241.447	34.818	-13.89	17.64	0.97	1.02	-0.026	BUTJ_GPS
241.513	35.033	-13.81	14.42	1.11	1.20	-0.027	DBL1_GPS
241.811	34.983	-10.86	15.15	0.91	0.96	-0.075	SOLE_GPS
240.773	35.267	-12.48	11.32	0.97	0.99	-0.062	0616_GPS
241.068	35.223	-12.53	10.77	1.16	1.25	-0.054	WEED_GPS
241.340	35.089	-13.22	14.24	1.22	1.31	-0.033	JACK_GPS
241.492	35.086	-11.56	14.72	0.94	0.96	-0.043	DEER_GPS
241.330	35.138	-13.60	12.98	0.99	1.08	-0.043	RSPG_GPS
241.843	35.087	-10.24	13.96	0.97	1.00	-0.043	PORT_GPS
241.591	35.134	-9.84	13.10	1.08	1.21	-0.023	SUMT_GPS
241.705	35.121	-10.97	13.58	1.21	1.32	-0.020	PAJA_GPS
241.375	35.274	-11.98	12.32	0.96	1.02	-0.052	0617_GPS
238.716	35.665	-29.26	37.01	1.00	1.01	-0.033	BLAN_GPS
238.516	35.992	-29.50	35.80	1.04	1.03	-0.025	0509_GPS
239.168	35.359	-28.58	35.56	0.82	0.86	-0.062	BLHL_GPS
239.302	35.386	-27.22	34.40	0.92	0.96	-0.045	TESS_GPS
239.701	35.346	-25.49	30.03	1.14	1.08	-0.035	POZO_GPS
239.427	35.456	-27.22	33.17	0.87	0.91	-0.059	BARR_GPS
239.547	35.552	-25.23	31.55	0.84	0.87	-0.055	ALMO_GPS
239.707	35.583	-23.97	29.00	1.42	1.03	-0.037	L623_GPS
240.234	35.414	-13.51	16.18	1.39	1.19	-0.058	GOUD_GPS
239.887	35.520	-20.62	24.96	0.95	0.92	-0.038	POSO_GPS
239.999	35.575	-16.17	18.79	0.96	0.92	-0.052	C616_GPS
239.654	35.607	-24.67	30.05	1.09	1.01	-0.037	H623_GPS
239.739	35.605	-23.23	26.87	0.83	0.86	-0.057	REDH_GPS
240.146	35.603	-12.44	15.01	0.92	0.89	-0.049	P807_GPS
240.606	35.398	-13.33	12.57	0.88	0.88	-0.049	FIBR_GPS
241.526	35.662	-11.56	9.70	1.11	1.14	-0.029	ISLK_GPS
241.412	35.745	-11.67	9.87	0.88	0.91	-0.048	0614_GPS
239.953	35.889	-8.58	15.50	0.94	0.93	-0.047	TAR0_GPS
241.864	36.023	-9.81	9.51	0.86	0.89	-0.046	KMED_GPS
240.712	36.289	-10.82	11.33	1.00	1.02	-0.032	0609_GPS
241.974	34.333	-23.82	22.25	0.84	0.88	-0.058	CHIL_GPS

242.000	34.346	-24.04	22.61	1.06	1.07	-0.046	NEST_GPS
242.549	34.347	-17.12	18.34	0.91	0.94	-0.060	CAJO_GLA
242.140	34.413	-21.62	20.17	1.11	1.14	-0.031	DVPB_GPS
242.155	34.458	-18.05	19.22	0.85	0.88	-0.058	HOLC_GPS
242.322	34.382	-19.79	19.24	0.86	0.89	-0.056	TABL_GPS
242.235	34.493	-15.23	17.75	1.35	1.05	-0.032	0705_GLA
242.708	34.281	-17.11	18.64	0.95	0.98	-0.050	MILU_GLA
242.846	34.468	-14.09	13.88	1.01	1.03	-0.040	AVRY_GPS
242.932	34.454	-14.87	14.67	1.19	0.99	-0.059	PT65_GLA
241.879	34.502	-21.73	20.11	1.12	1.15	-0.032	VNPS_GPS
241.891	34.544	-19.06	20.57	1.21	1.32	-0.084	ALPN_GPS
242.078	34.512	-18.36	18.95	0.96	0.96	-0.045	PEAR_GLA
242.294	34.743	-12.59	15.58	0.95	0.97	-0.045	MDAY_GLA
242.758	34.537	-13.86	14.37	1.00	1.05	-0.070	0817_GPS
242.612	34.607	-15.02	16.20	1.02	1.04	-0.038	SCIA_GPS
242.770	34.630	-12.40	13.60	1.12	1.17	-0.064	ITER_GPS
243.302	34.391	-11.10	15.65	1.25	1.31	0.022	OLDD_GPS
243.335	34.454	-8.14	14.96	1.31	1.40	0.037	LAW4_GPS
243.671	34.734	-2.10	1.92	1.42	1.44	0.030	LAE4_GPS
244.257	34.559	-1.58	-0.76	1.06	1.08	-0.095	AMBO_GPS
243.984	34.624	-2.22	1.59	0.98	1.01	-0.035	SIBE_GPS
244.067	34.728	-3.16	-0.10	1.04	1.09	-0.077	0808_GPS
242.136	34.984	-11.43	14.22	0.95	0.98	-0.045	TTAP_GPS
242.305	34.925	-11.27	14.80	1.18	1.20	-0.026	PHLB_GPS
243.019	34.904	-10.06	11.15	0.89	0.91	-0.057	SOAP_GPS
242.793	34.975	-8.67	12.06	0.91	0.94	-0.045	RAIN_GPS
242.102	35.115	-10.45	13.43	0.98	1.01	-0.037	GS09_GPS
241.918	35.225	-11.55	13.04	0.97	0.99	-0.040	GS01_GPS
243.579	34.785	-4.84	2.84	1.00	1.03	-0.043	HECT_GPS
243.585	35.072	-5.75	1.69	1.09	1.14	-0.048	0803_GPS
244.598	35.142	-2.14	-0.19	0.84	0.86	-0.050	RVAL_GPS
245.396	34.807	-2.16	0.98	1.11	0.98	-0.017	NEED_GPS
242.039	35.426	-11.31	11.04	0.97	1.00	-0.037	GS15_GPS
242.308	35.337	-8.10	11.92	0.88	0.92	-0.046	JOBU_GPS
242.386	35.366	-7.68	11.11	1.35	1.15	-0.035	0806_GPS
241.899	35.495	-11.40	11.12	0.94	0.97	-0.042	GS02_GPS
242.130	35.584	-11.09	10.54	0.95	0.98	-0.039	GS18_GPS
242.293	35.470	-9.32	11.05	0.94	0.97	-0.040	GS16_GPS
242.294	35.513	-8.81	10.84	1.38	1.36	-0.022	PAOS_GPS
242.443	35.569	-9.71	9.94	0.94	0.97	-0.039	GS17_GPS
242.667	35.434	-7.90	9.38	0.96	0.99	-0.041	GS12_GPS
243.111	35.425	-6.67	5.67	0.77	0.80	-0.059	GOL2_GPS
242.851	35.522	-6.62	7.58	0.93	0.95	-0.041	GS13_GPS
242.188	35.647	-9.26	10.99	0.93	0.94	-0.055	INYO_GPS
242.260	35.660	-9.48	11.31	0.92	0.94	-0.040	GS19_GPS

242.801	35.615	-7.13	7.45	0.94	0.97	-0.039	GS14_GPS
242.599	35.769	-7.35	7.70	0.94	0.96	-0.041	GS20_GPS
242.673	35.813	-6.51	6.28	0.92	0.95	-0.039	TRN1_GPS
243.700	35.867	-3.32	2.19	1.05	1.09	-0.116	0915_GPS
242.518	35.925	-8.31	6.44	0.94	0.97	-0.038	GS24_GPS
242.711	35.913	-6.47	6.27	0.93	0.95	-0.040	GS25_GPS
242.671	35.978	-6.12	5.37	0.94	0.92	-0.041	0914_GPS
242.821	36.035	-6.25	4.67	0.92	0.95	-0.039	GS07_GPS
242.093	36.203	-8.94	7.44	0.91	0.94	-0.042	GS04_GPS
242.359	36.307	-6.50	5.11	0.83	0.84	-0.047	P166_GPS
242.826	36.294	-4.32	3.48	0.83	0.87	-0.046	PANA_GPS
242.720	36.402	-5.51	4.18	0.95	0.95	-0.022	0911_GPS
243.350	36.316	-3.36	0.83	1.02	1.03	-0.029	RYAN_GPS
243.584	36.304	-2.51	1.65	0.93	1.03	-0.014	0912_GPS
243.525	36.397	-3.09	1.05	0.82	0.87	-0.044	FUNE_GPS
239.646	36.501	-7.70	9.95	1.24	1.05	0.042	0607_GPS
240.882	36.738	-9.48	11.12	1.10	1.03	-0.058	0605_GPS
241.815	36.781	-6.70	8.15	1.22	1.01	-0.033	INDE_GPS
241.706	37.233	-7.70	6.64	0.78	0.80	-0.051	OVRO_GPS
241.848	37.271	-7.16	4.90	0.89	0.92	-0.036	WSTG_GPS
241.764	37.572	-5.13	4.80	0.87	0.90	-0.036	WMTN_GPS
242.213	36.538	-8.87	5.55	1.03	1.12	-0.021	CERR_GPS
241.881	36.603	-8.47	7.91	0.92	0.95	-0.041	BAMA_GPS
241.899	36.914	-8.14	6.05	0.90	0.94	-0.035	RITA_GPS
243.022	36.724	-3.11	2.13	0.95	0.99	-0.002	0909_GPS
243.254	36.828	-3.75	2.84	1.05	1.12	-0.003	P16X_GPS
243.837	36.690	-1.72	0.96	0.90	0.93	-0.040	1PDI_GPS
243.531	36.838	-3.18	1.09	0.91	0.92	-0.042	MILE_GPS
243.739	36.943	-1.80	1.52	0.92	0.94	-0.031	SHSN_GPS
243.851	36.994	-1.78	0.09	1.04	1.03	-0.026	MN71_GPS
279.616	25.614	0.52	-0.30	0.77	0.75	0.009	RICM_GPS
255.985	30.680	-0.16	0.38	0.64	0.62	-0.046	MDO1_GPS
251.881	34.301	-0.26	-0.27	0.61	0.61	-0.054	PIE1_GPS
268.425	41.772	0.56	0.54	0.51	0.49	-0.005	NLIB_GPS
283.173	39.022	0.08	0.38	0.53	0.52	0.004	GODE_GPS
288.507	42.613	-0.32	-0.17	0.50	0.49	0.002	WES2_GPS
281.929	45.956	0.41	-0.69	0.46	0.45	0.001	ALGO_GPS
293.167	54.832	0.08	1.02	1.00	0.99	0.000	SCH2_GPS
210.394	-17.577	-68.77	52.60	1.04	0.97	0.007	THTI_GPS
200.335	22.126	-60.73	55.61	0.76	0.75	0.002	KOKB_GPS
183.434	-43.956	-40.93	55.81	0.69	0.67	0.002	CHAT_GPS
167.730	8.722	-71.25	50.14	0.79	0.77	-0.002	KWJ1_GPS
153.979	24.290	-75.82	41.67	1.03	0.97	-0.004	MARC_GPS
151.887	7.447	-72.74	41.88	0.91	0.85	-0.004	TRUK_GPS
243.709	35.397	-5.41	-0.02	1.32	1.30	0.048	SILV_GHT



243.448	35.426	-4.85	1.60	1.42	1.37	0.018	P_42_GHT
243.425	36.809	-3.31	1.58	1.37	1.37	-0.011	BLAK_GPS
243.319	36.889	-4.41	1.17	1.37	1.38	-0.013	CLAI_GPS
243.138	36.858	-3.68	2.15	1.10	1.10	0.009	F23X_GPS
243.071	36.792	-3.55	3.04	1.11	1.11	0.011	MO93_GPS
242.973	36.638	-3.78	2.73	1.09	1.08	0.010	HOLD_GPS
242.958	35.168	-10.15	10.21	1.35	1.36	0.034	GS36_GPS
242.863	37.218	-3.24	1.64	1.04	1.02	-0.014	SCTY_GPS
242.853	36.606	-4.11	3.23	1.10	1.09	0.022	STOV_GPS
242.837	35.375	-6.89	11.15	1.30	1.29	0.008	GS49_GHT
242.788	36.543	-4.56	3.49	1.10	1.09	0.022	G165_GPS
242.714	37.061	-3.38	2.31	1.01	0.99	-0.025	NEV1_GPS
242.700	36.349	-5.35	5.18	1.10	1.09	0.034	M137_GPS
242.683	35.214	-9.40	11.79	1.32	1.32	0.022	GS47_GHT
242.640	36.992	-3.77	2.10	1.03	1.01	-0.023	GRAP_GPS
242.576	36.340	-6.44	4.93	1.06	1.06	-0.011	13DD_GPS
242.551	37.019	-3.94	3.07	1.03	1.01	-0.024	SAND_GPS
242.546	36.053	-6.66	5.95	1.05	1.03	-0.022	GS27_GPS
242.541	35.584	-8.74	10.31	1.34	1.36	0.041	GS48_GPS
242.521	36.572	-5.28	3.76	1.06	1.05	-0.020	HUNT_GPS
242.500	36.865	-3.96	3.49	1.02	1.01	-0.025	TINP_GPS
242.495	35.213	-9.94	11.86	1.32	1.32	0.014	FMTH_GPS
242.460	36.532	-5.74	4.05	1.06	1.05	-0.022	JACK_GPS
242.454	36.067	-7.89	6.36	1.28	1.28	0.003	GS43_GPS
242.454	36.759	-4.59	3.39	1.04	1.01	-0.018	TEAK_GPS
242.450	36.279	-6.94	4.97	1.15	1.18	-0.001	L166_GPS
242.443	36.002	-7.57	7.13	1.28	1.29	0.001	GS45_GPS
242.439	36.519	-5.47	3.57	1.06	1.06	-0.014	FLAT_GPS
242.417	36.232	-6.82	5.34	1.09	1.09	-0.016	T19S_GPS
242.415	35.429	-9.01	11.58	1.07	1.05	-0.016	GS11_GPS
242.409	35.083	-10.79	13.60	1.33	1.32	0.014	GS50_GPS
242.388	36.497	-5.99	5.17	1.06	1.07	-0.015	LEEF_GPS
242.368	36.107	-8.18	5.59	1.29	1.30	0.003	GS42_GPS
242.328	36.094	-9.94	5.67	1.14	1.12	-0.011	GS34_GPS
242.325	36.150	-8.57	5.00	1.05	1.04	-0.020	6813_GPS
242.244	36.217	-7.43	6.40	1.15	1.13	-0.009	GS35_GPS
242.116	36.062	-7.71	7.96	1.10	1.11	-0.017	FORK_GGE
242.056	36.045	-9.10	10.01	1.09	1.09	-0.012	BM25_GPS
242.031	35.845	-9.73	10.93	1.05	1.04	-0.018	GS22_GPS
242.013	37.092	-6.82	6.27	1.34	1.34	-0.011	WAUC_GPS
241.965	35.668	-10.53	11.33	1.05	1.04	-0.016	GS03_GPS
241.954	37.737	-4.68	4.90	1.17	1.17	-0.032	FISH_GPS
241.868	36.466	-9.41	8.94	1.01	0.98	-0.031	3188_GPS
241.794	34.992	-12.15	14.48	1.15	1.13	0.008	TROP_GPS
241.712	36.979	-8.63	7.29	1.05	1.03	-0.034	ABER_GPS

241.273	36.185	-10.80	9.04	1.07	1.04	-0.018	SPRN_GPS
238.249	38.536	-10.91	7.37	0.38	0.37	0.012	UCD1_GPS
238.179	39.206	-10.79	6.89	0.40	0.40	0.010	SUTB_GPS
239.056	39.975	-9.89	6.77	0.31	0.30	0.049	QUIN_GPS
238.500	39.555	-10.10	6.52	0.39	0.38	0.004	ORVB_GPS

**Appendix C. Southern California block geometry**

The fault system geometry of our preferred block model is shown in the table below. All segments come to the surface with the exception of the Puente Hills Thrust (PHT), which is buried to a depth of 5 km.

Segment Name	longitude 1 (deg)	latitude 1 (deg)	longitude 2 (deg)	latitude 2 (deg)	dip (deg)	locking depth (km)
Avawatz	244.000	34.140	244.000	34.140	90	10
Avawatz	243.637	35.500	243.934	35.083	90	10
Avawatz	243.934	35.083	244.000	34.980	90	10
Calico Blackwater	242.575	35.500	243.251	34.816	90	5
Calico Blackwater	243.251	34.816	243.431	34.564	90	5
Calico Blackwater	243.431	34.564	243.637	34.161	90	5
Chino	242.174	34.139	242.481	33.794	90	10
Closure (east)	216.760	55.690	325.661	58.239	90	15
Closure (east)	274.413	-13.347	325.661	58.239	90	15
Closure (east)	260.639	5.079	274.413	-13.347	90	15
Closure (north)	191.871	57.592	216.760	55.690	90	15
Closure (west)	190.538	57.203	191.871	57.592	90	15
Closure (west)	259.341	1.742	260.639	5.079	90	15
Closure (west)	162.912	55.592	190.538	57.203	90	15
Closure (west)	145.025	41.058	162.912	55.592	90	15
Closure (west)	142.758	34.025	145.025	41.058	90	15
Closure (west)	131.169	29.806	142.758	34.025	90	15
Closure (west)	124.115	3.316	131.169	29.806	90	15
Closure (west)	124.115	3.316	164.764	-7.061	90	15
Closure (west)	164.764	-7.061	180.290	-36.871	90	15
Closure (west)	252.514	-42.884	259.341	1.742	90	15
Closure (west)	204.097	-69.387	252.514	-42.884	90	15
Closure (west)	162.871	-57.774	180.290	-36.871	90	15
Closure (west)	162.871	-57.774	204.097	-69.387	90	15
Closure (west)	230.593	47.950	235.278	40.845	90	15
Coastal Ranges Split	240.410	35.061	240.583	34.422	90	10
Cucamonga	241.995	34.147	242.174	34.139	135	15
Cucamonga	242.174	34.139	242.265	34.108	135	15
Cucamonga	242.265	34.108	242.324	34.129	135	15
Cucamonga	242.324	34.129	242.371	34.145	135	15
Cucamonga	242.371	34.145	242.605	34.178	135	15
Cucamonga	242.605	34.178	242.670	34.200	135	15

Death Valley	243.300	35.910	243.572	35.591	90	10
Death Valley	243.120	36.560	243.300	35.910	90	10
Death Valley	242.060	37.483	243.120	36.560	90	10
Death Valley	240.580	39.000	242.060	37.483	90	10
Deep Springs Valley	241.946	37.150	242.060	37.483	90	10
Elsinore	244.255	32.614	244.985	32.175	90	15
Elsinore	242.634	33.660	243.657	33.000	90	15
Elsinore	242.481	33.794	242.567	33.714	90	15
Elsinore	242.567	33.714	242.634	33.660	90	15
Eureka Peak	243.637	34.161	243.751	33.804	90	5
Garlock	241.072	34.818	241.530	35.000	90	15
Garlock	241.530	35.000	242.066	35.318	90	15
Garlock	242.066	35.318	242.240	35.420	90	15
Garlock	242.240	35.420	242.529	35.500	90	15
Garlock	242.565	35.510	243.045	35.578	90	10
Garlock	243.045	35.578	243.572	35.591	90	15
Goldstone Lake	243.091	35.500	243.292	35.156	90	10
Goldstone Lake	243.292	35.156	244.000	34.140	90	10
Hunter Mountain	242.196	36.664	242.583	36.456	90	10
Nevada	243.934	35.083	244.000	35.152	90	10
Nevada	246.603	41.890	246.689	37.971	90	10
Nevada	235.958	43.583	246.603	41.890	90	10
Newport	241.888	33.756	242.070	33.618	90	15
Newport	241.644	33.977	241.716	33.897	90	15
Newport	241.716	33.897	241.802	33.827	90	15
Newport	241.802	33.827	241.888	33.756	90	15
Newport	242.070	33.618	242.503	33.164	90	15
Newport	242.503	33.164	242.658	33.000	90	15
Newport Inglewood	241.587	34.051	241.644	33.977	90	15
Oak Ridge	240.670	34.216	241.135	34.409	45	15
Oceanside	242.503	33.164	242.520	33.000	90	15
Owens Valley	241.949	36.570	242.017	36.143	90	10
Owens Valley	240.580	39.000	241.521	37.633	90	10
Owens Valley	241.521	37.633	241.949	36.570	90	10
Owens Valley	216.760	55.690	230.593	47.950	90	15
Owens Valley	230.593	47.950	235.958	43.583	90	15
Owens Valley	235.958	43.583	240.580	39.000	90	15
Pacific	239.935	34.156	241.350	33.119	90	15
Pacific	241.350	33.119	241.488	33.000	90	15
Pacific	243.141	31.575	244.239	31.325	90	15
Pacific	244.239	31.325	245.328	29.522	90	15
Pacific	245.328	29.522	259.341	1.742	90	15
Pacific	238.131	36.359	238.976	35.415	90	15
Pacific	238.976	35.415	239.196	34.971	90	15

Pacific	239.196	34.971	239.335	34.565	90	15
Pacific	239.500	34.477	239.563	34.443	90	15
Pacific	239.563	34.443	239.756	34.309	90	15
Pacific	239.756	34.309	239.935	34.156	90	15
Palos Verdes	241.360	34.014	241.706	33.757	90	15
Palos Verdes	241.706	33.757	242.369	33.000	90	15
Palos Verdes	242.541	32.803	243.141	31.575	90	15
Panamint Valley	242.583	36.456	243.045	35.578	90	10
Pinto Mountain	243.637	34.161	244.000	34.140	90	15
Puente Hills	242.009	33.820	242.301	33.774	135	15
Puente Hills	242.301	33.774	242.481	33.794	135	15
Puente Hills	241.740	34.099	242.009	33.820	135	15
Raymond Hill	241.587	34.051	241.740	34.099	135	15
Raymond Hill	241.740	34.099	241.829	34.117	90	15
Raymond Hill	241.829	34.117	241.995	34.147	90	15
Saline Valley	241.946	37.150	242.196	36.664	90	10
San Andreas	240.255	35.191	240.410	35.061	90	25
San Andreas	240.410	35.061	240.615	34.929	90	25
San Andreas	240.615	34.929	240.750	34.873	90	25
San Andreas	240.999	34.821	241.072	34.818	90	25
San Andreas	241.548	34.677	242.195	34.428	90	25
San Andreas	241.072	34.818	241.548	34.677	90	25
San Andreas	242.195	34.428	242.378	34.347	90	25
San Andreas	242.378	34.347	242.670	34.200	90	25
San Andreas	242.670	34.200	242.879	34.110	90	15
San Andreas	242.879	34.110	243.106	34.031	90	15
San Andreas	243.106	34.031	243.751	33.804	90	15
San Andreas	243.751	33.804	244.000	33.592	90	15
San Andreas	244.278	33.356	244.494	32.908	90	10
San Andreas	244.494	32.908	244.985	32.175	90	0
San Andreas	244.985	32.175	247.749	29.024	90	15
San Andreas	247.749	29.024	260.639	5.079	90	15
San Andreas	237.416	37.772	239.157	36.265	90	0
San Andreas	239.717	35.743	239.922	35.525	90	25
San Andreas	239.947	35.500	240.255	35.191	90	25
San Andreas	239.157	36.265	239.378	36.066	90	10
San Andreas	239.378	36.066	239.717	35.743	90	10
San Andreas	240.750	34.873	240.999	34.821	90	25
San Andreas	235.278	40.845	237.416	37.772	90	15
San Cayetano	240.800	34.465	241.135	34.409	135	5
San Cayetano	240.583	34.422	240.800	34.465	135	5
San Cayetano	241.135	34.409	241.377	34.463	135	5
San Gabriel	241.072	34.818	241.124	34.699	90	15
San Gabriel	241.124	34.699	241.377	34.463	90	15

San Gabriel	241.377	34.463	241.527	34.392	135	15
San Gabriel	241.527	34.392	241.676	34.320	135	15
San Gregorio	237.416	37.772	238.131	36.359	90	15
San Jacinto	242.978	33.862	244.000	33.068	90	10
San Jacinto (south)	242.670	34.200	242.978	33.862	90	10
San Jacinto (south)	244.028	33.046	244.985	32.175	90	10
Santa Monica	241.034	34.028	241.360	34.014	135	15
Santa Monica	241.360	34.014	241.498	34.023	135	15
Santa Monica	241.498	34.023	241.587	34.051	135	15
Santa Monica (west)	240.670	34.216	240.748	34.064	135	15
Santa Monica (west)	240.748	34.064	241.034	34.028	135	15
Sierra Madre	241.767	34.282	241.905	34.182	135	15
Sierra Madre	241.676	34.320	241.767	34.282	135	15
Sierra Madre	241.905	34.182	241.995	34.147	135	15
Sierra Madre	242.017	36.143	242.565	35.510	90	10
Ventura (west)	239.756	34.309	240.670	34.216	45	15
Ventura Split	241.377	34.463	241.482	34.210	90	10
Ventura Split	240.583	34.422	240.670	34.216	90	10
Ventura Split	241.482	34.210	241.587	34.051	90	10

## References

- Argus, D. F., M. B. Helfin, A. Donnellan, F. H. Webb, D. Dong, K. J. Hurst, D. C. Jefferson, G. A. Lyzenga, M. M. Watkins, and J. F. Zumberge, Shortening and thickening of metropolitan Los Angeles measured and inferred using geodesy, *Geology*, 27, 703 - 706, 1999.
- Argus, D. F., and R. G. Gordon, Present tectonic motion across the Coast Ranges and San Andreas fault system in Central California, *Geol. Soc. Am. Bull.*, 113, 1580-1592, 2001.
- Atwater, T., Implications of plate tectonics for the Cenozoic evolution of western North America, *Geol. Soc. Am. Bull.*, 81, 3512 - 3535, 1970.
- Bawden, G. W., W. Thatcher, R. Stein, K. W. Hudnut, G. Peltzer, Tectonic contraction across Los Angeles after removal of groundwater pumping effects, *Nature*, 412, 812 - 815, 2001.
- Bennett, R. A., W. Rodi, and R. E. Reilinger, Global Positioning System constraints on fault slip rates in Southern California and northern Baja, Mexico, *J. Geophys. Res.*, 101, 21,943 - 21,960, 1996.
- Bennett, R. A., B. P. Wernicke, J. L. Davis, P. Elosegui, J. K. Snow, M. J. Abolins, M. A. House, G. L. Stirewalt, and D. A. Ferrill, Global Positioning System constraints on fault slip rates in the Death Valley region, California and Nevada, *Geophys. Res. Lett.*, 24, 3073-3076, 1997.
- Beanland, S., and M. M. Clark, The Owens Valley fault zone, eastern California, and surface faulting associated with the 1872 earthquake, *U. S. Geol. Surv. Bull.*, 1982, p. 29, 1994.
- Bird, P., and J. Baumgardner, Fault friction, regional stress, and crust-mantle coupling in Southern California from finite element models, *J. Geophys. Res.*, 89, 1932-1944, 1984.
- Bird, P., and R. W. Rosenstock, Kinematics of present crust and mantle flow in southern California, *Geol. Soc. Am. Bull.*, 95, 946 - 957, 1984.
- Bird, P., and X. Kong, Computer simulations of California tectonics confirm very slow strength of major faults, *Geol. Soc. Am. Bull.*, 106, 159 - 174, 1994.
- Cheng, A., D. D. Jackson, and M. Matsu'ura, Aseismic crustal deformation in the Transverse Ranges of Southern California, *Tectonophysics*, 144, 159-180, 1997.
- DeMets, C., R. G. Gordon, D. F. Argus and S. Stein, Current plate motions. *Geophys. J. Int.*, 101, 425-478, 1990.

DeMets, C., and T. Dixon, New kinematic models for Pacific-North America motion from 3 Ma to present, 1: Evidence for steady motion and biases in the NUVEL-1A model, *Geophys. Res. Lett.*, 26, 1921-1924, 1999.

Dixon, T. H., M. Miller, F. Farina, H. Wang, and D. Johnson, Present-day motion of the Sierra Nevada block and some tectonic implications for the Basin and Range Province, North American Cordillera, *Tectonics*, 19, 1-24, 2000.

Dixon, T. H., E. Norabuena, and L. Hotaling, Paleoseismology and Global Positioning System; earthquake-cycle effects and geodetic versus geologic fault slip rates in the Eastern California shear zone, *Geology*, 31, 55-58, 2003.

Dolan, J. F., K. Sieh, T. K. Rockwell, Late Quaternary activity and seismic potential of the Santa Monica fault system, Los Angeles, California, *Geol. Soc. Am. Bull.*, 112, 1559-1581, 2000.

Donnellan, A., B. H. Hager, and R. W. King, Discrepancy between geological and geodetic deformation rates in the Ventura Basin, *Nature*, 366, 333 - 336, 1993a.

Donnellan, A., B. H. Hager, R. W. King, and T. A. Herring, Geodetic measurement of deformation in the Ventura basin region, southern California, *J. Geophys. Res.*, 98, 21,727 - 21,739, 1993b.

Ellsworth, W. L., Earthquake history, 1769-1989, Wallace, R. E. ed., The San Andreas fault system, California, U. S. Geological Survey Professional Paper, P 1515, 153-187, 1990.

Feigl, K. L., R. W. King, and T. H. Jordan, Geodetic measurement of tectonic deformation in the Santa Maria fold and thrust belt, California, *J. Geophys. Res.*, 95, 2679-2699, 1990.

Feigl, K. L., D. C. Agnew, Y. Bock, D. Dong, A. Donnellan, B. H. Hager, T. A. Herring, D. D. Jackson, T. H. Jordan, R. W. King, S. Larsen, K. M. Larson, M. H. Murray, S. Zhengkang, and F. H. Webb, Space geodetic measurement of crustal deformation in Central and Southern California, *J. Geophys. Res.*, 98, 21,677 - 21,712, 1993.

Gan, W., J. L. Svarc, J. C. Savage, and W. H. Prescott, Strain accumulation across the eastern California shear zone at latitude 36 degrees 30 N, *J. Geophys. Res.*, 105, 16,229-16,236, 2000.

Hager, B. H., G. A. Lyzenga, A. Donnellan, and D. Dong, Reconciling rapid strain accumulation with deep seismogenic fault planes in the Ventura Basin, California, *J. Geophys. Res.*, 104, 25,207-25,219, 1999.



Hanks, T. C., and H. Kanamori, A moment magnitude scale, *J. Geophys. Res.*, 84, 2348-2350, 1979.

Hauksson, E. Crustal structure and seismicity distribution adjacent to the Pacific and North America plate boundary in southern California, *J. Geophys. Res.*, 105, 13,875-13,903, 2000.

Hearn, E. H., and E. D. Humphreys, Kinematics of the southern Walker Lane Belt and motion of the Sierra Nevada block, California, *J. Geophys. Res.*, 103, 27,033-27,049, 1998.

Hubert-Ferrari, A., A. Barka, E. Jacques, S. S. Nalbant, B. Meyer, R. Armijo, P. Tapponnier, and G. C. P. King, Seismic hazard in the Marmara Sea region following the 17 August 1999 Izmit earthquake, *Nature*, 404, 269-273, 2000.

Hudnut, K. W., Y. Bock, M. Cline, P. Fang, Y. Feng, J. Freymueller, X. Ge, W. K. Gross, D. Jackson, M. Kim, N. E. King, J. Langbein, S. C. Larsen, M. Lisowski, Z. K. Shen, J. Svarc, and J. Zhang, Co-seismic displacements of the 1992 Landers earthquake sequence, *Bull. Seis. Soc. Am.*, 84, 625-645, 1994.

Hudnut, K. W., Z. Shen, M. Murray, S. McClusky, R. King, T. Herring, B. Hager, Y. Feng, P. Fang, P., A. Donnellan, and Y. Bock, Co-seismic displacements of the 1994 Northridge, California, earthquake, *Bull. Seis. Soc. Am.*, 86, 19-36, 1996.

Jennings, C. W., Fault Activity Map of California and Adjacent Areas with Location and Ages of Recent Volcanic Eruptions. California Geologic Data Map Series, Map No. 6. California Division of Mines and Geology, 1994.

Johnson, H. O., D. C. Agnew, and F. K. Wyatt, Present - day crustal deformation in Southern California, *J. Geophys. Res.*, 99, 23,951 - 23,974, 1994.

Kagan, Y. Y., <http://scec.ess.ucla.edu/ykagan.html>, 2002.

Kaverina, A., D. Dreger, and E. J. Price, The combined inversion of seismic and geodetic data for the source process of the 16 October 1999  $M_w$  7.1 Hector Mine, California, earthquake, *Bull. Seis. Soc. Am.*, 92, 1266-1280, 2002.

Kohlstedt, D. L., B. Evans, and S. J. Mackwell, Strength of the lithosphere; constraints imposed by laboratory experiments, *J. Geophys. Res.*, 100, 17,587-17,602, 1995.

Lyons, S. N., and D. Sandwell, Fault creep along the southern San Andreas from interferometric synthetic aperture radar, permanent scatterers, and stacking, *J. Geophys. Res.*, 108, 2047, doi:10.1029/2002JB001831, 2003.

Malvern, L. E., Introduction to the Mechanics of a Continuous Medium, 1969.

Matsu'ura, M., and D. D. Jackson, Dislocation model for aseismic crustal deformation at Hollister, California, *J. Geophys. Res.*, *91*, 12,661 - 12,674, 1986.

McCaffrey, R., Estimates of modern arc-parallel strain rates in fore arcs, *Geology*, *24*, 27-30, 1996.

McClusky, S. C., S. C. Bjornstad, B. H. Hager, R. W. King, B. J. Meade, M. M. Miller, F. C. Monastero, and B. J. Souter, Present Day Kinematics of the Eastern California Shear Zone from a Geodetically Constrained Block Model, *Geophys. Res. Lett.*, *28*, 3339 - 3372, 2001.

McGill, S., and K. Sieh, Holocene slip rate of the central Garlock Fault in southeastern Searles Valley, California, *J. Geophys. Res.*, *98*, 14,217 - 14,231, 1993.

McGill, S., and T. Rockwell, Ages of late Holocene earthquakes on the central Garlock Fault near El Paso Peaks, California, *J. Geophys. Res.*, *103*, 7265 - 7279, 1998.

Meade, B. J., B. H. Hager, and R. E. Reilinger, Estimates of Seismic Potential in the Marmara Sea from Block Models Constrained by GPS Observations, *EOS Trans. AGU*, *82*(20), Spring Meet. Suppl., Abstract T61A-06, 2001.

Meade, B. J., B. H. Hager, S. C. McClusky, R. E. Reilinger, S. Ergintav, O. Lenk, A. Barka, and H. Ozener, Estimates of Seismic Potential in the Marmara Sea Region from Block Models Secular Deformation Constrained by Global Positioning System Measurements, *Bull. Seis. Soc. Am.*, *92*, 208 - 215, 2002.

Miller, M. M., D. J. Johnson, T. H. Dixon, and R. K. Dokka, Refined kinematics of the Eastern California shear zone from GPS observations, 1993-1998, *J. Geophys. Res.*, *106*, 2245-2263, 2001.

Minster, J. B., and T. H. Jordan, Present-day plate motions, *J. Geophys. Res.*, *83*, 5331-5354, 1978.

Minster, B., and T. H. Jordan, Vector constraints on western U.S. deformation from space geodesy, neotectonics, and plate motions, *J. Geophys. Res.*, *92*, 4798 - 4804, 1987.

Murray, M. H., and P. Segall, Modeling broad scale deformation in northern California and Nevada from plate motions and elastic strain accumulation, *Geophys. Res. Lett.*, *28*, 4315 - 4318, 2001.

Nur, A., and G. Mavko, Postseismic viscoelastic rebound, *Science*, *183*, 204 - 206, 1974.

Nur, A., H. Ron, and G. Beroza, Landers-Mojave earthquake line; a new fault system?, *GSA Today*, 3, p. 253, 256-258, 1993a.

Nur, A., H. Ron, and G. C. Beroza, The nature of the Landers - Mojave earthquake line, *Science*, 261, 201 - 203, 1993b.

Okada, Y. Surface deformation due to shear and tensile faults in a half space, *Bull. Seis. Soc. Am.*, 75, 1135-1154, 1985.

Oskin, M. E., Transient versus long-term strain accumulation on the Blackwater Fault, Eastern California shear zone, *Abstracts with Programs – Geol. Soc. of Am.*, 34, 39, 2002.

Peltzer, G., F. Crampe, S. Hensley, and P. Rosen, Transient strain accumulation and fault interaction in the Eastern California shear zone, *Geology*, 29, 975 - 978, 2001.

Petersen, M. D., and S. G. Wesnousky, Fault slip rates and earthquake histories for active faults in Southern California, *Bull. Seis. Soc. Am.*, 84, 1608 - 1649, 1994.

Pollitz, F. F., G. Peltzer and R. Burgmann, Mobility of continental mantle: Evidence from postseismic geodetic observations following the 1992 Landers earthquake, *J. Geophys. Res.*, 105, 8035-8054, 2000.

Potter, D. R., Long-Term Postseismic Relaxation in Southern California: Evidence from a Geostatistical Analysis of Geodetic Data, *Ph. D. Dissertation*, University of California Los Angeles, 1997.

Reid, H.F., The mechanics of the earthquake, v. 2 of The California Earthquake of April 18, 1906: Report of the State Earthquake Investigation Commission: Carnegie Institution of Washington Publication 87, C192 p.2 vols., 1910.

Rockwell, T. K., S. Lindvall, M. Herzberg, D. Murback, T. Dawson, and G. Berger, Paleoseismology of the Johnson Valley, Kickapoo, and Homestead Valley Faults: Clustering of Earthquakes in the Eastern California Shear Zone, *Bull. Seis. Soc. Am.*, 90, 1200 - 1236, 2000.

Sauber, J., W. Thatcher, and S. C. Solomon, Geodetic Measurement of Deformation in the Central Mojave Desert, California, *J. Geophys. Res.*, 91, 12,683 - 12,693, 1986.

Sauber, J., W. Thatcher, S. C. Solomon, and M. Lisowski, Geodetic slip rate for the Eastern California shear zone and the recurrence time of Mojave Desert earthquakes, *Nature*, 367, 264 - 266, 1994.

Saucier, F., and E. Humphreys, Horizontal crustal deformation in Southern California from joint models of geologic and very long baseline interferometry measurements, Smith, D. E., D. L. Turcotte eds., Contributions of space geodesy to geodynamics; crustal dynamics, Geodynamics Series, 23, 139-176, 1993.

Savage, J. C., Viscoelastic coupling model for the earthquake cycle driven from below, *J. Geophys. Res.*, 105, 25,525 - 25,532, 2000.

Savage, J. C., and R. O. Burford, Geodetic determination of the relative plate motion in central California, *J. Geophys. Res.*, 78, 832 - 845, 1973.

Savage, J. C., and W. H. Prescott, Asthenosphere readjustment and the earthquake cycle, *J. Geophys. Res.*, 83, 3369 - 3376, 1978.

Savage, J. C., M. Lisowski, and W.H. Prescott, An Apparent Shear Zone Trending North-Northwest across the Mojave Desert into Owens Valley, Eastern California, *Geophys. Res. Lett.*, 17, 2113-2116, 1990.

Savage, J. C., and M. Lisowski, Viscoelastic coupling model of the San Andreas fault along the Big Bend, southern California, *J. Geophys. Res.*, 103, 7281 - 7292, 1998.

Savage, J. C., W. Gan, and J. L. Svarc, Strain accumulation and rotation in the Eastern California shear zone, *J. Geophys. Res.*, 106, 21,995-22,007, 2001.

Segall, P., Integrating Geologic and Geodetic Estimates of Slip Rate on the San Andreas Fault System, *Int. Geol. Rev.*, 44, 62--82, 2002.

Sella, G. F., T. H. Dixon, and A. Mao, REVEL: a model for recent plate velocities from space geodesy, *J. Geophys. Res.*, 107, p. 17, 2002.

Sieh, K., Slip along the San Andreas Fault associated with the great 1857 earthquake: *Bull. Seis. Soc. Am.*, 68, 1421-1428, 1978.

Sieh, K. E., and R. H. Jahns, Holocene activity of the San Andreas Fault at Wallace Creek, California, *Geol. Soc. Am. Bull.*, 95, 883-896, 1984.

Schaff, D. P., G. H. R. Bokelmann, G. C. Beroza, F. Waldhauser, and W. L. Ellsworth, High-resolution image of Calaveras Fault seismicity, *J. Geophys. Res.*, 107, p. 16, 2002.

Sharp, R. V., Variable Rates of Late Quaternary Strike Slip on the San Jacinto Fault Zone, Southern California, *J. Geophys. Res.*, 86, 1754 - 1762, 1981.

Shaw, J. H., and P. M. Shearer, An elusive blind - thrust fault beneath metropolitan Los Angeles, *Science*, 283, 1516 - 1518, 1999.

Shen, Z-K., D. D. Jackson, and B. X. Ge, Crustal Deformation Across and Beyond the Los Angeles Basin from Geodetic Measurements, *J. Geophys. Res.*, 101, 27,957 - 27,980, 1996.

Souter, B. J., Comparisons of geological models to GPS observations in Southern California, *Ph. D. Dissertation*, Massachusetts Institute of Technology, 1998.

Steblov G. M., M. G. Kogan, R. W. King, C. H. Scholz, R. Bürgmann, D. I. Frolov, Imprint of the North American plate in Siberia revealed by GPS, *Geophys. Res. Lett.*, 30 (18), 1924, doi:10.1029/2003GL017805, 2003.

Stein, R. S., Hanks, and C. Thomas,  $M \geq 6$  earthquakes in southern California during the twentieth century; no evidence for a seismicity or moment deficit, *Bull. Seis. Soc. Am.*, 88, 635-652, 1998.

Walls, C., T. Rockwell, K. Mueller, Y. Bock, S. Williams, J. Pfanner, J. Dolan, and P. Feng, Escape tectonics in the Los Angeles metropolitan regions and implications for seismic risk, *Nature*, 394, 356 - 360, 1998.

Ward, S. N., On the consistency of earthquake moment rates, geologic fault data, and space geodetic strain: the United States, *Geophys. J. Int.*, 134 (1), 172-186, 1998.

Weaver, K. D., and J. F. Dolan, Paleoseismology and geomorphology of the Raymond Fault, Los Angeles County, California, *Bull. Seis. Soc. Am.*, 90, 1409-1429, 2000.

Weldon, R. J., and K. E. Sieh, Holocene rate of slip and tentative recurrence interval for large earthquakes on the San Andreas Fault, Cajon Pass, Southern California, *Geol. Soc. Am. Bull.*, 96, 793 - 812, 1985.

Weldon, R. J., and E. D. Humphreys, A Kinematic Model of Southern California, *Tectonics*, 5, 33 - 48, 1986.

Wells, D. L., K. J. Coppersmith, New empirical relationships among magnitude, rupture length, rupture width, rupture area, and surface displacement, *Bull. Seis. Soc. Am.*, 84, 974 - 1002, 1994.

Wessel, P., W. H. F. Smith, Free software helps map and display data, *EOS Trans. AGU*, 84, 441, 1991.

Yule, Doug, and Sieh, Kerry, The paleoseismic record at Burro Flats; evidence for a 300-year average recurrence for large earthquakes on the San Andreas Fault in San Gorgonio Pass, Southern California, *Abstracts with Programs – Geol. Soc. Am.*, 33, 31, 2000.



## Chapter 2

# Viscoelastic Deformation for a Clustered Earthquake Cycle<sup>9</sup>

**Abstract.** The clustering of earthquakes in time on the same fault affects the rate and pattern of interseismic deformation. We develop a model of the surface velocity field through a clustered earthquake cycle by superposing the velocities of individual viscoelastic earthquake cycles of constant period but varying phase. Velocity profiles prior to and after an earthquake show a much wider range of behavior than they do through a single earthquake cycle. These new types of behavior provide possible explanations for discrepancies between geologic estimates of long-term fault slip rates and slip rate estimates from geodetic data.

### 1. Introduction

Characterizations of the temporal pattern of earthquakes range from periodic (*Reid, 1910, Savage and Prescott, 1978*) to chaotic (*Scholtz, 1992*). Periodically spaced events have been recognized in the rupture history revealed by paleoseismic data in New Zealand (*Bull, 1996*). Other ancient large earthquake catalogs reveal complicated behavior that appears more regular than chaotic, and is described as clustered in time (e.g., *Wallace, 1987, Swan, 1988; Sieh et al., 1989, Grant and Seih, 1994, Marco et al.,*

---

<sup>9</sup> This work is being prepared for publication with Brad Hager

1996, *Rockwell et al.*, 2000, *Friedrich et al.*, 2003). The clustered events consist of a small number of earthquakes, typically 2-6, occurring in rapid succession on the same fault segment. This active period is followed by a period largely devoid of major seismic events (figure 1). The reported time spans covered by single clustered cycles range widely, from several hundred years for the Carrizo segment of the San Andreas Fault (*Sieh et al.*, 1989), to 20,000 – 30,000 yrs for the Wasatch fault in Utah (*Friederich et al.*, 2003), the Dead Sea fault (*Marco et al.*, 1996), and the Xiaojiang fault in China (*Xu and Deng*, 1996).

Several theoretical investigations have addressed the possible causes of clustering. For example, *Ben-Zion et al.* (1999) and *Lyakovsky et al.* (2001) showed that fault healing and damage rheology could lead to clustering. *Lynch et al.* (2003) showed that communication between nearby fault segments via viscoelastic coupling could result in clustering. *Kenner and Simons* (2003) used a simple analog spring-dashpot-slider system to show that low viscosities and low loading rates tend to promote clustering.

The question that we address in this paper is how earthquake clustering influences the geodetically observable velocity field measured near a fault. For example, *Friederich et al.* (2003) addressed observations of deformation across the Wasatch fault zone in eastern Utah on both geologic and geodetic time scales. They demonstrated that earthquakes in this region are clustered; four large earthquakes have occurred there in the past 10,000 yrs, following a period of relative inactivity for ~ 20,000 yrs. The geologic slip rate estimated over the more recent active period is three times that estimated for the inactive period. They provided a number of hypotheses about how the geodetic rate



might compare to the geologic rate averaged over 10,000 yr (intra-cluster) and 30,000 yr (inter-cluster) time scales. *Pe'eri et al.* (2002) have used geodetic measurements of interseismic deformation to estimate the strike slip rate on the Dead Sea fault, a structure that is one of the type locales for clustering (*Marco et al.*, 1996). Our model provides a new framework for interpreting these observations.

## 2. An idealized clustered earthquake cycle

Consider the simple idealized description of a clustered earthquake cycle shown in Figure 1. Each clustered cycle of inter-cluster period  $T$  is made up of an active period, with  $n$  earthquakes repeating with offsets  $\Delta T$ , and a quiet period of duration  $T - (n-1)\Delta T$ . If  $s$  is the characteristic coseismic slip per event and  $v_0$  is the long-term geologic slip rate of the fault, the balance between coseismic slip and long-term geologic slip is given by  $ns = v_0 T$ . For the model shown in figure 1,  $n = 4$  and  $\Delta T = T/10$ . We also define the average recurrence interval,  $T_{av} = T/n$ , which gives the relation  $s = v_0 T_{av}$ .

The time evolution of the surface velocity field during the earthquake cycle depends on the rheology of the system. Here we present a simple model of the deformation associated with an infinitely long strike slip fault in an elastic layer of thickness  $H$  overlying a half space consisting of a Maxwell viscoelastic material. We assume that each earthquake breaks the entire elastic layer. *Savage and Prescott* (1978) and *Savage* (2000) described the time evolution of the surface velocity field through an earthquake cycle for this model, assuming that earthquakes are strictly periodic with period,  $T$ . The resulting velocity field is a function of two additional times: the time since

the last earthquake,  $t$ , and the Maxwell relaxation time of the viscoelastic halfspace,  $\tau_M = \eta/\mu$ , where  $\mu$  is the shear modulus and  $\eta$  is the dynamic viscosity. Because of the wide range in  $T$  observed, it is useful to combine these three times into dimensionless parameters, only two of which are independent. Since we are investigating repeating earthquakes, we follow *Savage and Prescott (1978)* in using the dimensionless parameters  $\tau_0 = T/2\tau_M$ , and  $t' = t/T$ . (In the limit  $T$  goes to infinity, this formulation can also be used to describe the response of a single earthquake.)

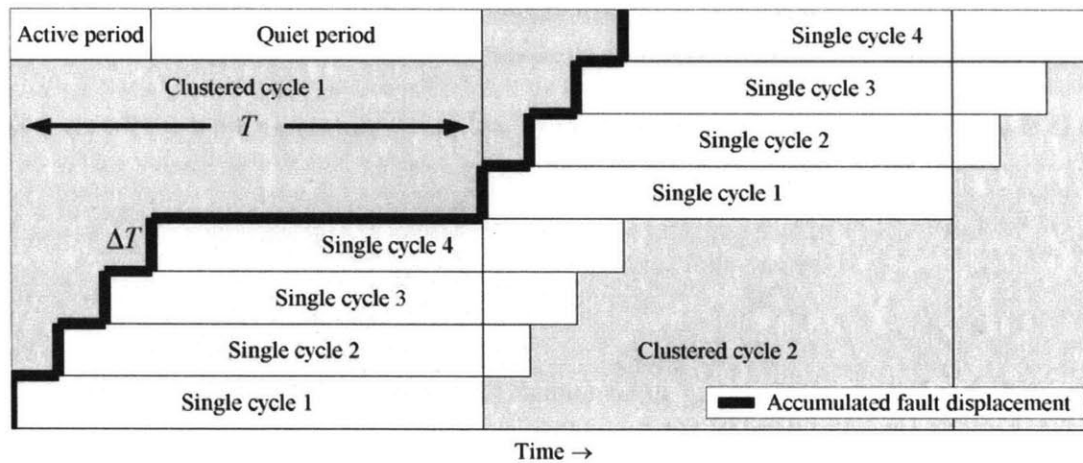


**Figure 1.** A schematic diagram of a clustered earthquake cycle. Each single earthquake cycle is represented by a thin rectangle. These are offset and stacked on top of each other to emphasize the overlapping nature of the earthquake cycles. The length of the single earthquake cycles is the same as the clustered earthquake cycle. The heavy dark line shows what the temporal pattern of deformation at the fault trace.

Despite the more complex temporal pattern of earthquakes, some of the important models for a single earthquake cycle can be extended to the clustered case. Both the

single and clustered earthquake cycles must balance interseismic strain accumulation and coseismic strain release. Our clustered earthquake cycle model can be taken to the limit of a periodic earthquake model with long-term geologic slip rate in two ways. If  $n$  and  $s$  are held constant, and  $\Delta T = T/n = T_{av}$ , the model becomes periodic with period  $T/n$ . Alternatively, in the limit  $\Delta T$  goes to zero the model becomes periodic with period  $T$ , but the slip in the composite event must be increased proportionally, to  $ns$ , to balance the geologic rate. In comparing our results to those for periodic earthquakes, both limits are of interest and it is important to specify which is used.

It is straightforward to generalize the *Savage and Prescott (1978)* model to the simple clustered earthquake cycle shown in figure 1. A clustered earthquake cycle begins with the onset of one active period and ends at the start of the next. The clustered earthquake cycle can be thought of as the superposition of  $n$  individual earthquake cycles, each with period  $T$ . (Note that, for each of these individual earthquake cycles,  $\tau_0$  is defined in terms of  $T$ , not in terms  $T_{av}$  for the entire cluster.) We calculate velocity profiles for a given relaxation parameter by summing the contributions from the individual earthquake cycles

$$v_c(t', \tau_0, \Delta T, n) = \sum_{k=1}^n v_s(|\Delta T(t' - k - 1)|, \tau_0) \quad (1)$$

where,  $v_c$  is the velocity due to the event clustering,  $t$  is the time since the onset of the active period,  $n$  is the number of earthquakes in the active period,  $v_s$  is the velocity from

*Savage's* (2000) model and  $\Delta T$  is the time lag between earthquakes. For the plots shown here, we model the behavior of a clustered earthquake cycle with  $n = 4$  earthquakes separated by  $T / 10$  each and a relaxation parameter  $\tau_0 = 5$ . For example, for a choice of  $T = 500$  year (as might be appropriate for the SAF, corresponding to  $\eta \approx 5 \times 10^{19}$  Pa·s for  $\mu = 30$  GPa), the active and quiet periods are 150 and 350 years long respectively; for  $T = 25,000$  yrs (as might be appropriate for the Wasatch fault, corresponding to  $\eta \approx 2.5 \times 10^{21}$  Pa·s) the active and quiet periods are 7,500 and 17,500 years long respectively.

In an elastic half space the steady state interseismic velocity profile parallel to an infinitely long vertical strike slip fault is given by  $v = v_0 \pi^{-1} \tan^{-1}(x/H)$  where  $x$  is the distance from the fault trace,  $H$  is the locking depth and  $v_0$  is the slip rate (e.g., *Savage and Burford, 1973*). This model provides a useful reference for the effects of viscoelasticity.

Figure 2 shows velocity profiles at various times for a clustered earthquake cycle. For reference, we show the results for the two limiting cases of periodic earthquakes – the case  $\Delta T = 0$ , with slip  $4s$  (Figure 2a) and the case  $\Delta T = T / 4$  (Figure 2b). For large  $\tau_0$ , ( $\tau_0 = 5$  in Figure 2a) there are large variations through the earthquake cycle. Immediately after an earthquake, the fault parallel velocity is greater than the steady state velocity and peaks near the fault. Late in the cycle, as the next earthquake approaches, the surface velocities decay to values lower than the steady state and the maximum velocity is found far away from the fault. This pattern can be succinctly summarized as “slow before, fast after”. In Figure 2b, since the recurrence interval is a factor of 4 smaller than that in

Figure 2a, the effective  $\tau_0$  is a factor of 4 smaller,  $\tau_0 = 1.25$ . For lower values of  $\tau_0$ , (i.e. shorter repeat time or higher viscosity) (Figure 2b) there is less variation through the earthquake cycle due to viscoelastic relaxation.

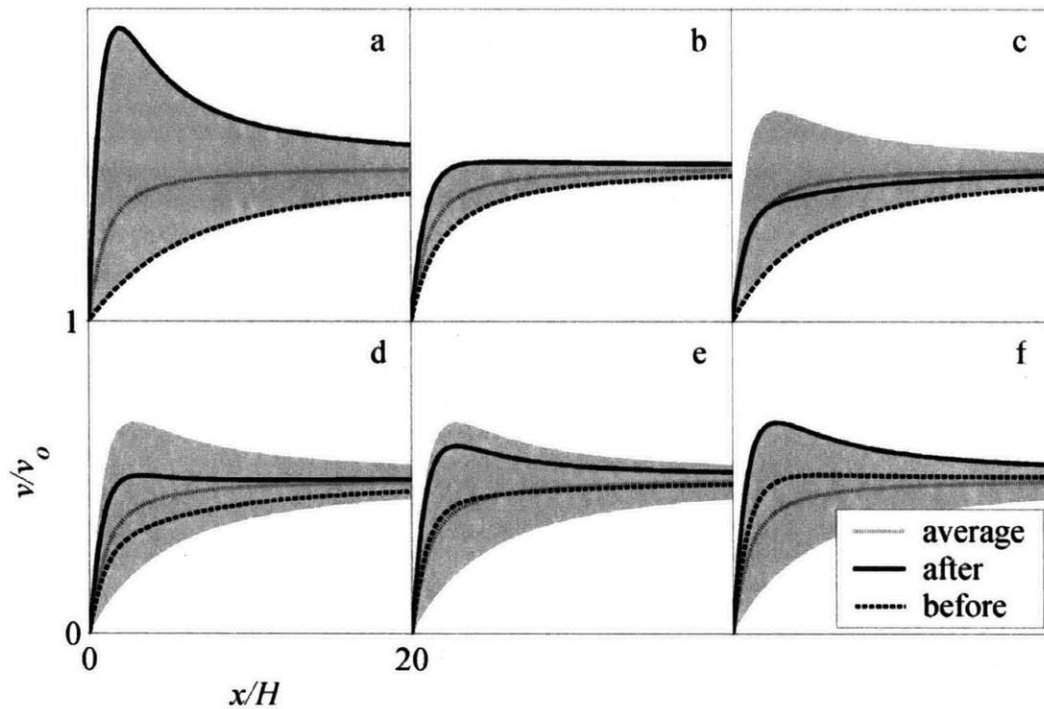


**Figure 2.** Interseismic velocity profiles. Each of these figures shows half of a fault parallel velocity profile at various times through the earthquake cycle. In all cases the finely dashed line is the steady state profile, the solid black line is the profile immediately following an event and the coarsely dashed line shows the velocity profile immediately prior to the event. The axes are the same for all figures but are shown only on the lower left figure for clarity. a) Profiles for a single earthquake cycle with  $\tau_0^{\text{ref}}$ . b) Profiles for a single earthquake cycle with  $\tau_0^{\text{ref}} / 4$ . c) Profiles for the first event in a clustered earthquake cycle with  $\tau_0^{\text{ref}}$ . d) Profiles for the second event in a clustered earthquake cycle with  $\tau_0^{\text{ref}}$ . e) Profiles for the third event in a clustered earthquake cycle with  $\tau_0^{\text{ref}}$ . f) Profiles for the fourth, and last, event in a clustered earthquake cycle with  $\tau_0^{\text{ref}}$ .

Immediately after the first earthquake in the clustered cycle, the velocity is slower than the steady state profile (figure 2c). This is because the three other out of phase earthquake sequences that are late in their cycles contribute very little and effectively reduce the total velocity. Thus in a clustered earthquake cycle the velocity immediately after an earthquake need not be greater than the steady state value even in the case of large  $\tau_0$ . This is a case of “slow before, slow after” and is different from the single earthquake cycle model where the velocity following an earthquake is always greater than the steady state value (Figures 2a, b).

After additional active period earthquakes (figure 2d), the pre-event velocity is slow and the postseismic is fast, just as in the single earthquake cycle. Late in the active period the pre-event velocity may be greater than the steady state due to the influence of the high velocities generated by the previous earthquakes (“fast before, fast after”, see figure 2f). Again, this is different from the prediction for a single earthquake cycle where the velocity preceding an earthquake is always less than the steady state value. Of course, at the end of a long enough quiet period the velocities are much lower than the steady state as all of the earthquakes are late in their cycles. In total, the pattern of deformation immediately before and after earthquakes in the presence of clustering shows a range of behavior including “slow before, slow after” for the first event in the sequence “slow before, fast after” for the second, and “fast before, fast after” for the fourth. The interseismic velocity profiles between the third and fourth events in the active period are particularly notable as they are remarkably similar to steady state profiles with a shallower locking depth and a slightly lower slip rate.

Earthquake clustering also tends to reduce the total amount of variation through the seismic cycle. The area swept through by the velocity profile in the single earthquake cycle (shaded area in figure 2b) is greater than that swept through in any event in the clustered earthquake cycle (shaded area in figures 2b-d). The after profiles are never as “fast” and the before profiles are never as “slow”. Thus, the steady state assumption may be more appropriate for a clustered earthquake cycle than for a single earthquake cycle.

### 3. Variations with $\tau_0$ and $\Delta T / T$

Thus far we've only presented the results for what might be termed a typical clustered earthquake cycle. Two interesting parameters to vary are the active period interevent time  $\Delta T / T$  and the relaxation parameter  $\tau_0$ . This is similar to the single earthquake cycle; smaller values of  $\tau_0$  give smaller variations through the seismic cycle, though the magnitude of variation is smaller in a clustered earthquake cycle (figure 3). However, there is more variation than for the case of overlapping periodic earthquakes where  $T / \Delta T = n$ .

Values of  $\tau_0 \geq 5$  show greater deviations from the steady state and preserve the same sense of behavior. An exception is the velocity immediately following the first active period event which does significantly exceed the steady state profile within a few locking depths of the fault trace. Longer interevent times tend to reduce variability by averaging over a greater portion of the earthquake cycle. Conversely, shorter interevent times increase variability while preserving the sense of pre- and post-earthquake behavior

discussed in the previous section. Thus, we always see less total variability in a clustered earthquake cycle than for a single event case.

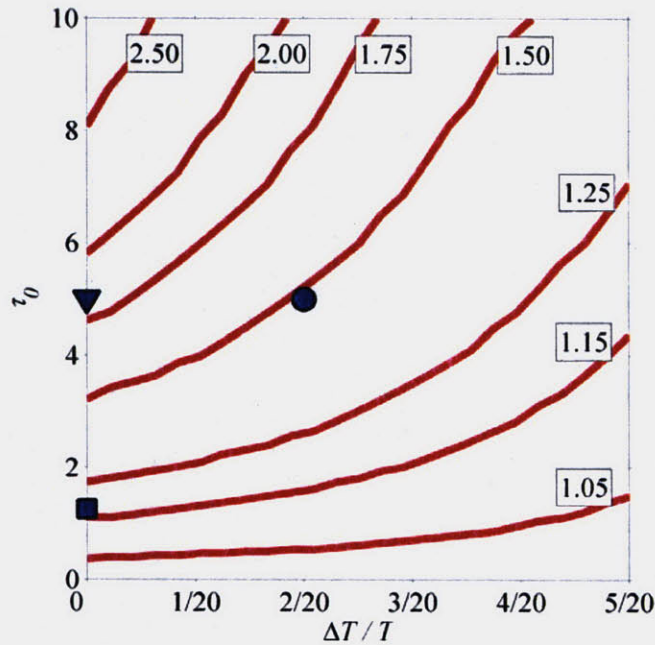


**Figure 3.** Variations with  $\tau_0$  and interevent time,  $\Delta T$ . The shaded circle shows the values of  $\tau_0$  and  $\Delta T$  that we use for our example clustered earthquake cycle. The contours show deviations in the peak velocity from a reference model. As  $\Delta T$  decreases the total amount of variation through the clustered earthquake cycle increases. Conversely, the contours grow sparser as  $\Delta T$  increases as the different earthquake cycles overlap on one another and tend to average to the reference earthquake cycle. The shaded circle, triangle, square and circle represent the cases shown in figures (2a), (2b), and (2c, d, e, f) respectively.



#### 4. Discussion

The parameter  $\tau_0$  can be shown to be the same as the parameter that *Kenner and Simons* (2003) named the Wallace number and used to describe their models; systems with large  $\tau_0$  tended to show clustered earthquakes, suggesting that their model could be tested by geodetic data if the *Savage and Prescott* (1978) model were extended to earthquakes that are clustered. Modern geodetic techniques, including GPS and InSAR, allow for precise measurements of crustal velocities with uncertainties on the order of millimeters per year. Fault slip rates can be estimated by fitting the observed velocities to models of interseismic deformation. Using steady state models to interpret a viscoelastic velocity field, “fast” profiles yield “fast” slip rates and “slow” profiles yield “slow” slip rates in the absence of significant far field data (e.g., *Meade and Hager*, 2004a). This somewhat crude mapping allows us to study variations through the seismic cycle by comparing present day slip rates with long term slip rates obtained with paleoseismic and geomorphic methods. Several notable examples are more readily interpreted with a clustered rather than a single earthquake cycle model.

The model immediately suggests an explanation for why the geodetic slip rate estimates across the Wasatch fault are substantially higher than the 26,000 yr geologic average (*Friedrich et al.*, 2003). Several clustered events have recently occurred so the situation is comparable to that shown in figure 2f. As can be seen from figure 2f, rates may appear faster than the long term geologic rate even if it has been a long time since the last earthquake. If we can extrapolate the results for our strike-slip model to an

extensional environment, for  $T = 26,000$  yrs,  $\tau_0 = 5$ , corresponds to a viscosity of  $\eta \approx 2.5 \times 10^{21}$  Pa·s – a relatively high value.

The most widely recognized fault in the Southern California Fault System (SCFS) is the San Andreas (SAF). As it emerges from the Big Bend, south of Cajon Pass, the main fault trace is ill defined until the partially creeping segment south of the Salton Sea (*Lyons and Sandwell, 2003*). *Sieh et al. (1989)* estimated that the southern SAF (i.e., Indio segment) most likely last ruptured in a large event in  $1688 \pm 13$  CE with two prior events in the preceding 400 years. If we consider the past 400 years as the quiescent period then it is at least as long as the active period, thus  $T \geq 800$  years and  $\Delta T \approx 130$  years. The length of the quiet period is unknown but slip rate estimates based on geodetic data (e.g., *Meade and Hager, 2004a*) may reflect behavior late in the quiet period of a clustered earthquake cycle, and thus be less than the long-term average.

Paralleling the SAF, about 40 km to the west, is the San Jacinto Fault (SJF) with a long-term (half-Quaternary) strike slip rate of 12 mm/yr (*Sharp, 1981*). Present day slip rate estimates based on models of interseismic geodetic observations find a slip rate of  $14.3 \pm 0.4$  mm/yr (*Meade and Hager, 2004a*). As it has been  $\sim 250$  years since the last major earthquake on the San Jacinto and typical recurrence intervals are expected to be on the order of no more than 400 years, the fault must be considered to be late in a single earthquake cycle. However, this fails to help explain the apparent discrepancy between the geologic and geodetic slip rate estimates. The reason this single earthquake model fails is that late in the earthquake cycle the apparent slip rate (geodetic estimate) should be lower than the long term average (geologic estimate). Again, this is the opposite of

the situation we observe today where the San Jacinto Fault is relatively fast compared with the long term geologic rate (*Sharp, 1981*).

However, the San Jacinto rupture history as revealed in the paleoseismic record (*Rockwell, 2003*) provides evidence for the temporal clustering of earthquakes. Specifically, the fault has experienced approximately five ruptures over the last 1100 years, while there is a record of only one substantial fault displacement for at least the previous millennium (900-0 CE). This suggests that prior to 900 CE the SJF had been quiet for nearly a thousand years, and that the last thousand years are an active period in terms of the clustered earthquake model. Thus, the SJF may still be in an active period of a clustered earthquake cycle. Unfortunately, the SJF paleoseismic record is currently insufficient to determine either the quiet period length or the number of active period earthquakes. However, we suggest that the present situation may be similar to that presented in the idealized clustered earthquake model. If there are still earthquakes left to occur in the current active period then although it has been a long time since the last event (and presumably less time until the next) we currently may be observing a situation analogous to that shown in figure 2f. In this case, immediately prior to the last active period earthquake and for a long time after, the fault parallel velocity is greater than the long-term value.

For the SJF case, this model would require that the quiet period is longer than the active period by at least a factor of two, and  $\tau_0 = 5-10$  for  $\Delta T \approx 250$  years. If  $\tau_0$  were higher, the relaxation would be too fast for us to observe today. Conversely if  $\tau_0$  were much lower, there would be negligible variation from the steady state expectation.

For typical shear modulus values this range of  $\tau_0$ 's suggest a range of dynamic viscosities  $\eta \approx 10^{20} - 10^{21}$  Pa·s. These values are higher by at least an order of magnitude than those estimated by *Pollitz et al. (2001)* based on InSAR observations of postseismic deformation following the 1992 Landers earthquake to the north-northeast of the SJF.

In the Eastern California Shear Zone (ECSZ), south of the Garlock Fault, geodetic estimates of slip rates (*McClusky et al., 2001, Peltzer et al., 2001*) have tended to be higher than geologic estimates (e.g., *Rockwell et al., 2000, Oskin, 2002*) by a factor of two. While both *McClusky et al. (2001)* and *Peltzer et al. (2001)* determined slip rates after the 1992 Landers earthquake, their models are consistent with the high strain rate estimates made prior to the event (*Sauber et al., 1994*). Fast rates before and after the Landers earthquake are incompatible with the variation in surface deformation predicted by the single earthquake cycle model. However, the clustered earthquake model does show this “fast before, fast after” behavior near the last earthquake in the active period (figure 2f). To double the apparent slip rate prior to the last earthquake in the cycle would require  $\tau_0 \geq 5$ . This is likely reasonable for the ECSZ, where the repeat time is believed to be quite long (e.g., *Rockwell et al., 2000*).

The pre-earthquake velocity profile in figure 2d is quite similar to the profile that would be expected from the same fault slip rate but with a shallow locking depth. *Peltzer et al. (2001)* estimated a shallow locking depth for the Blackwater fault in California's Mojave Desert using radar interferometry. The alternative explanation is that the fault is

not locked to some shallow depth, but is instead near to the last earthquake in an active period of a clustered earthquake cycle.

## 5. Conclusions

A clustered earthquake cycle model shows a wider variety of pre- and post-seismic behavior with respect to the steady state model than does the single earthquake cycle. At the same time, there is less total variability through the clustered cycle due to the overlapping of individual earthquake cycles. These observations highlight the challenge of interpreting geodetic measurements of crustal deformation in the context of viscoelastic relaxation. Despite this difficulty, the clustered earthquake model provides both the motivation and a mechanism for integrating paleoseismic rupture histories with present day estimates of interseismic surface velocities to determine the dynamics of actively deforming zones. This model may help to reconcile apparent differences between short and long-term fault slip rates as well as provide an alternative explanation for estimates of apparently shallow fault locking depths in some places.

**References**

Bull, B. W., Prehistorical earthquakes on the Alpine Fault, New Zealand, *J. Geophys. Res.*, *101*, 6037-6050, 1996.

Dorsey, R. J., P. J., Umhoefer, and P. D. Faulk, Earthquake clustering inferred from Pliocene Gilbert-type fan deltas in the Loreto Basin, Baja California Sur, Mexico, *Geology*, *25*, 679-682, 1997.

Elsasser, W. M., Convection and stress propagation in the upper mantle, in *The application of modern physics to the earth and planetary interiors*, ed. S. K. Runcorn, 223-246, 1969.

Friedrich, A. M., B. P. Wernicke, N. Niemi, R. A. Bennett, and J. L. Davis, Comparison of geodetic and geologic data from the Wasatch region, Utah, and implications for the spectral character of Earth deformation at periods of 10 to 10 million years, *J. Geophys. Res.*, *108*, doi:10.1020/2002JB000682, 2003.

Grant, L. B., and K. Sieh, Paleoseismic evidence of clustered earthquakes on the San Andreas fault in the Carrizo Plain, California, *J. Geophys. Res.*, *99*, 6819-6841, 1994.

Marco, S., M. Stein, and A. Agnon, Long-term earthquake clustering: A 50,000-year paleoseismic record in the Dead Sea Graben, *J. Geophys. Res.*, *106*, 4103-4120, 1996.

McClusky, S. C., S. C. Bjornstad, B. H. Hager, R. W. King, B. J. Meade, M. M. Miller, F. C. Monastero, and B. J. Souter, Present Day Kinematics of the Eastern California Shear Zone from a Geodetically Constrained Block Model, *Geophys. Res. Lett.*, *28*, 3339-3372, 2001.

Meade, B. J., B. H. Hager, S. C. McClusky, R. E. Reilinger, S. Ergintav, O. Lenk, A. Barka, and H. Ozener, Estimates of Seismic Potential in the Marmara Sea Region from Block Models Secular Deformation Constrained by Global Positioning System Measurements, *Bull. Seis. Soc. Am.*, *92*, 208-215, 2002.

Meade, B. J., and B. H. Hager, Block Models of the Present Day Deformation of Southern California Constrained by Geodetic Measurements, *J. Geophys. Res.*, In prep, 2004a. (Chapter 1 of this thesis)

Oskin, M., Transient versus long-term strain accumulation on the Blackwater Fault, Eastern California shear zone, *Geol. Soc. Am.*, *34* (6), 39, 2002.

Pe'eri, S., S. Wdowinski, A. Shtibelman, N. Bechor, Y. Bock, R. Nikolaidis and M. van Domselaar, Current plate motion across the Dead Sea Fault from three years of continuous GPS monitoring, *Geophys. Res. Let.*, doi:10.1029/2001GL013879, 2002.

Peltzer, G., F. Crampe, S. Hensley, and P. Rosen, Transient strain accumulation and fault interaction in the Eastern California shear zone, *Geology*, 29, 975-978, 2001.

Reid, H.F., The mechanics of the earthquake, v. 2 of The California Earthquake of April 18, 1906: Report of the State Earthquake Investigation Commission: Carnegie Institution of Washington Publication 87, C192 p.2 vols., 1910.

Rockwell, T. K., S. Lindvall, M. Herzberg, D. Murback, T. Dawson, and G. Berger, Paleoseismology of the Johnson Valley, Kickapoo, and Homestead Valley Faults: Clustering of Earthquakes in the Eastern California Shear Zone, *Bull. Seis. Soc. Am.*, 90, 1200-1236, 2000.

Rockwell, T. K., personal communication, 2002.

Sauber, J., W. Thatcher, S. C. Solomon, and M. Lisowski, Geodetic slip rate for the Eastern California shear zone and the recurrence time of Mojave Desert earthquakes, *Nature*, 367, 264-266, 1994.

Savage, J. C., Viscoelastic coupling model for the earthquake cycle driven from below, *J. Geophys. Res.*, 105, 25,525-25,532, 2000.

Savage, J. C., and R. O. Burford, Geodetic determination of the relative plate motion in central California, *J. Geophys. Res.*, 78, 832-845, 1973.

Savage, J. C., and W. H. Prescott, Asthenosphere readjustment and the earthquake cycle, *J. Geophys. Res.*, 78, 3369-3376, 1978.

Seih, K., M. Stuiver, and D. Brillinger, A More Precise Chronology of Earthquakes Produced by the San Andreas Fault in Southern California, *J. Geophys. Res.*, 94, 603-623, 1989.

Scholz, C. H., Earthquake predictions: models of the seismic cycle, *Nature*, 335, 774-775, 1992.

Sharp, R. V., Variable Rates of Late Quaternary Strike Slip on the San Jacinto Fault Zone, Southern California, *J. Geophys. Res.*, 86, 1754 - 1762, 1981.

Swan, F. H., Temporal clustering of paleoseismic events on the Oued Fodda Fault, Algeria, *Geology*, 16, 1092-1095, 1988.

Vergnolle, M., F. Pollitz, and E. Calais, Constraints on the viscosity of the continental crust and mantle from GPS measurements and postseismic deformation models in western Mongolia, *J. Geophys. Res.*, 108, doi:10.1029/2002JB002374, 2002.



## Chapter 3

### Spatial Localization of Moment Deficits in Southern California<sup>10</sup>

**Abstract.** The balance between elastic strain accumulation and release defines the extent to which a fault system suffers from a surplus or deficit of large earthquakes. We present an estimate of the regional moment accumulation rate in Southern California based on a new slip rate catalog estimated from a block model constrained by geodetic data. The moment accumulation rate calculated from this catalog ( $\sim 21.2 \pm 4.2 \times 10^{18}$  N·m/yr) is nearly twice as large as previous estimates. We also introduce a new method for localizing areas of high moment deficit. In Southern California we find three major areas of moment deficit: 1) the Southern San Andreas and San Jacinto Faults, 2) the northern Mojave Desert, and 3) the greater Los Angeles area. We calculate the minimum magnitude earthquake sources that could eliminate these deficits. For the Southern San Andreas and San Jacinto Faults we find that an equivalent  $M_w = 7.8$  earthquake is required to balance the deformation accumulated over the last two centuries.

#### 1. Introduction

The potential for large earthquakes is typically characterized by one of three approaches. The first is the estimation of moment magnitudes based on the geometries of faults (e.g., *Dolan et al.*, 1995, *Shaw and Shearer*, 1998, *Meade et al.*, 2002). A second method is to estimate Gutenberg Richter  $b$ -values from earthquake catalogs and extrapolate these values to larger magnitudes and other locations (e.g., *Working Group on*

---

<sup>10</sup> This work is being prepared for publication with Brad Hager

*California Earthquake Probabilities (WGCEP), 1995, Stein and Hanks, 1998*). The third approach is based on assessing the balance between interseismic moment accumulation and coseismic moment release rates (e.g., *WGCEP, 1995, Stein and Hanks, 1998, Ward, 1998*). We extend this third method to allow us to localize regions of seismic moment deficit. This is feasible because we have a moment accumulation (slip rate) model that is consistent with geodetic data, fault system geometry, and plate motion constraints. In addition to identifying regions of local moment release deficit, we estimate the sources of the smallest coseismic events that could alleviate these deficits. The identification of localized areas of moment deficit presents clear targets for paleoseismic work.

## 2. Moment accumulation, release and balance

The potency, or geometric moment, of an earthquake is the product of the average slip over the rupture area,  $P = \bar{s}A$  (e.g., *Ben-Zion, 2001*). Geodetic studies of earthquake sizes typically assume an elastic Poisson body and therefore directly estimate the potency of a coseismic rupture. Earthquake sizes are more commonly expressed as scalar moments. Potency is typically converted to moment by multiplying  $P$  by the shear modulus  $\mu = 3 \times 10^{10}$  Pa. For the sake of continuity with the literature, we use moment throughout the rest of this paper.

The total coseismic moment release,  $M_0^R$ , in a given region is the sum over all earthquakes.

$$M_0^R = \sum_j^{\text{earthquakes}} M_0^j = \mu \sum_j^{\text{earthquakes}} \bar{s}_j A_j \quad (1)$$

The shear modulus,  $\mu$ , is treated as a constant. This is certainly not the case in Southern California where there are large vertical and lateral variations in lithology that have an impact on deformation from faulting (e.g., Ventura Basin, *Hager et al.*, 1999). The mean annual moment release rate,  $\dot{M}_0^R$ , is calculated by dividing the total moment release,  $M_0^R$ , by the time span of the earthquake catalog from which it was derived,  $T_{eq}$ .

We define the regional moment accumulation rate,  $\dot{M}_0^A$ , in terms of fault slip rates on rectangular fault patches as

$$\dot{M}_0^A = \mu \sum_i^{\text{faults}} \|\vec{v}_i\| A_i \quad (2)$$

Here  $\|\vec{v}\|$  is the magnitude of the slip rate vector. If fault slip rates are constant in time then the total moment accumulation is given by the moment accumulation rate multiplied by the time over which it has been accumulating  $M_0^A = \dot{M}_0^A T_{eq}$ .

Other authors have used alternative definitions of moment accumulation rate based entirely on geodetic data. *Ward* (1994, 1998) calculated an interseismic moment accumulation rate following *Kostrov's* (1974) method as  $\dot{M}_0^A = 2\mu a H \dot{\epsilon}$ , where  $H$  is the seismogenic thickness and  $\dot{\epsilon}$  is the strain rate determined from geodesy,  $a$  is the surface area not of the faults, but of the deforming region. This interpretation of geodetic data

does not include any information regarding the fault system geometry where moment is actually released, so provides only a lower bound. In addition, this method may suffer from the strain rate paradox, where high strain rates are correlated with shallow fault locking depths and anti-correlated with strain release in large earthquakes. The creeping segment of the San Andreas Fault northwest of Parkfield is the type example.

Regardless of the method employed, the question is the same: Has the rate of coseismic moment release,  $\dot{M}_0^R$ , kept up with the rate of moment accumulation,  $\dot{M}_0^A$ , over the time span of the earthquake catalog,  $T_{eq}$ ? If the moment release rate is greater than the accumulation rate,  $\dot{M}_0^R > \dot{M}_0^A$ , then there is a moment surplus. Conversely more moment accumulation than release,  $\dot{M}_0^A > \dot{M}_0^R$ , defines a moment deficit. In order to calculate these quantities we should first understand the data that constitute the fault slip rate and historical earthquake catalogs.

### 3. Earthquake catalogs

The length of the historical earthquake catalog in Southern California is less than 200 years. As *Stein and Hanks* (1998) have pointed out, the record prior to 1850 should be viewed with skepticism. The biggest reason for this is that there are not the type of shaking and damage reports required to reliably estimate the locations and magnitudes of earthquakes; we have a very short history of earthquake activity in Southern California. In the second half of the 19<sup>th</sup> century the population of the southern half of the state increased and newspapers followed (*Stein and Hanks*, 1998). Media reports describing the 1857 Ft. Tejon earthquake are extremely valuable for characterizing its magnitude.

Paleoseismic studies also allow us to date the time of pre-historic events, but with less control on the slip magnitude and event size. As more paleoseismic studies are completed, it may be possible to build estimated rupture models for events that pre-date the recorded history of Southern California.

What are the contents of the earthquake catalogs that are currently available? *Ellsworth* (1990) compiled an extensive list of all of the major earthquakes in Southern California since 1800. *Stein and Hanks* (1998) supplemented this list by adding six earthquakes with  $M_w \approx 6$  to the south of the U.S.-Mexico border. *Kagan* (2002) compiled a catalog that contains not only these estimates, but also the Harvard CMT focal mechanism estimates for more recent events (figure 1). For calculations in the following sections, we use a slightly modified version of the *Kagan* (2002) catalog. The only change we have made is the magnitude estimate for the 1872 Owens Valley earthquake. *Kagan* (2002) reports this as  $M_w = 7.2$ , a value significantly smaller than estimates that put the magnitude close to  $M_w = 7.8$ . In the context of our moment deficit calculations, the larger magnitude estimate, which we adopt, is conservative.

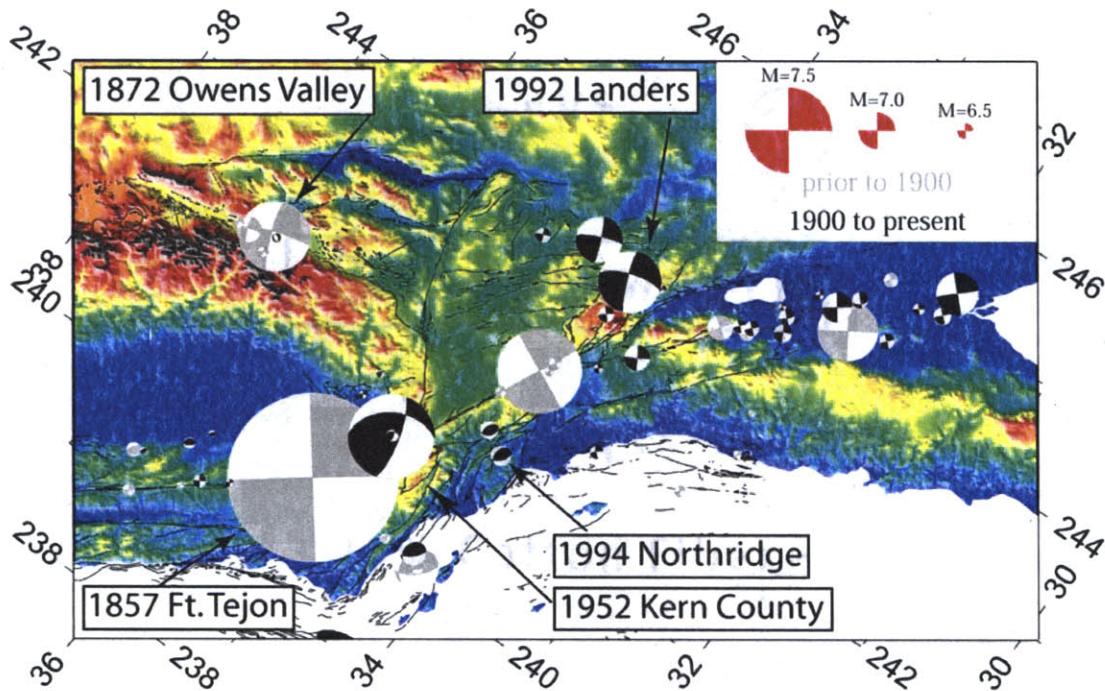


**Figure 1.** Focal mechanisms for large earthquakes (Kagan, 2002) in Southern California overlaid on topography (GTOPO30) and fault traces (Jennings, 1994). The area of each focal mechanism is proportional to its scalar seismic moment. The darker quadrants are compressional. Focal mechanisms with gray compressional quadrants are those from 1807-1900, and those with black compressional quadrants are from 1900-present. The largest focal mechanism is associated with 1857 Ft. Tejon earthquake along the San Andreas Fault.

Of all the parameters in the Southern California catalog, the magnitude of the Ft. Tejon is the greatest unknown. Sieh (1978) estimated that it was a  $M_w = 7.9$ , based on the mapped surface slip distribution. However, the slip distribution at depth is unknown. For this reason we assign the Ft. Tejon event an uncertainty of  $\sigma_{M_w} = 0.1$  magnitude units. This equates to a difference in moment release of 40%.

#### 4. Fault slip rate catalogs

Fault slip rate catalogs are the essential components for computing moment accumulation rates. We use two different catalogs and compare their results. The standard catalog of fault slip rates for Southern California has been compiled by the California Division of Mines and Geology (CDMG<sup>11</sup>, *Petersen et al.*, 1996). This catalog is largely based on the *Petersen and Wesnousky* (1994) review paper. *Meade and Hager* (2004a) present an alternative slip rate catalog derived from their block model constrained by geodetically estimated interseismic velocities. The block model (BM) slip rate catalog has two features that distinguish it from the *Petersen et al.* (1996) catalog. First, it satisfies the path integral constraint, as discussed in *Meade and Hager* (2004a). This ensures that fault slip rates are internally consistent. Second, the block-model-derived slip rate catalog combines the fault system geometry information with geophysical information into a unified framework. The slip rate estimates vary substantially even for the most well known structure in Southern California: the San Andreas Fault. The *Petersen et al.* (1996) catalog reports Holocene estimates of 25 – 35 mm/yr for the SAF from San Bernadino (*Weldon and Sieh*, 1985) to the Carrizo Plain (*Sieh and Jahns*, 1984). In contrast, the block model estimates that the San Bernadino segment of the SAF is roughly 5 times slower than the Carrizo Plain (*Meade and Hager*, 2004a). This is a consequence of the geometric constraints implicit in the block model approach. Thus, the two catalogs present substantially different results: one based on

---

<sup>11</sup> Now known as the California Geological Survey (CGS).

geologic data (*Petersen et al.*, 1996) and the other based on geodetic data (*Meade and Hager*, 2004a).

Despite all geologic and geophysical data that goes into both catalogs, we still haven't quantified what we don't know about slip rates. That is, how much deformation is occurring on other structures such as folds and unrecognized structures. The geologic catalog places no constraints on the amount of deformation that is occurring on unrecognized structures. While not explicitly recognizing the thousands of small faults that populate the crust, the block modeling method (*Meade and Hager*, 2004a) ensures that all active slip is accounted for on some structure, in the absence of extreme local rotations. This is not the case for the *Petersen et al.* (1996) catalog, which, on the other hand, has the advantage of precise long-term rates, determined at specific locations.

*Scholz and Cowie* (1990) suggested that only a small percentage of the active deformation occurs off of "large" structures, based on an analysis of displacement – length scaling relationships. *Marrett and Allmendinger* (1992) argued that the fault displacement – length relationship derived from a detailed study of the Viking graben (North Sea) is inconsistent with the *Scholz and Cowie* (1990) result. Both of these studies rely on the definition of fault length, which may not be meaningful in the context of fault systems where all major faults are connected in branching networks. The path integral constraint (e.g., *Weldon and Humphries*, 1986, *Minster and Jordan*, 1987, *Meade and Hager*, 2004a) suggests that all fault networks should be fully connected if there is to be a long-term balance between plate motion and plate boundary zone deformation.



## 5. Regional moment balance

The regional moment balance in Southern California has been debated extensively over the last decade (e.g., *WGCEP*, 1995, *Stein and Hanks*, 1998, *Ward*, 1998). Previous results are summarized in Table 1. All of these authors offered estimates for the average regional moment accumulation and release rates. The length and content of the historical earthquake catalog require some interpretation. Of all the faults in Southern California, only the San Andreas has a recurrence interval comparable to the length of the historical earthquake catalog (*Sieh et al.*, 1989). For a characteristic rupture event with slip,  $s$ , a fault will have an average recurrence time inversely proportional to its slip rate: Thus, the length of the historical earthquake catalog is shorter than the average recurrence interval for maximum size events on all faults in Southern California other than the SAF. The clustering of earthquakes in time (e.g., *Sieh et al.*, 1989, *Friedrich et al.*, 2003) can further increase the time interval over which moment accumulation and release will balance. A clustered earthquake cycle has both an active and quiescent period. The active period is characterized by 2-5 large earthquakes (Chapter 2). The time between earthquakes within the active phase of a cluster is not sufficient for the fault to accumulate the strain released in the next event. However, excess strain accumulates during the quiescent part of the clustered earthquake.

The short length of the historical earthquake catalog precludes us from rigorously determining the regional moment balance over a quasi-periodic or clustered earthquake cycle. However, we can still assess whether or not moment release and accumulation

balance over the last 200 years. This calculation can be thought of as the deviation from some reference quasi-periodic earthquake cycle.

*Ekstrom and England* (1989) demonstrated that short duration earthquake catalogs without large events and sparse fault catalogs are insufficient to assess moment balance. *WGCEP* (1995) reported an approximate release rate of  $8.3 \times 10^{18}$  N·m/yr based on a limited seismic catalog that included a low magnitude for the 1857 Ft. Tejon event,  $M_w = 7.8$ , and did not include the 1873 Owens Valley ( $M_w = 7.2-7.8$ ) earthquake. (It should be noted that *WGCEP* (1995) used a moment-moment magnitude relationship that gives moments approximately 12-25% less than the widely used *Hanks and Kanamori* (1979) relationships.) This value is balanced by an approximately identical moment accumulation rate (table 1) based on the average strain rate across Southern California. Despite this apparent agreement, consistent with no moment deficit, *WGCEP* acknowledge that they have arbitrarily set the locking depth to 11 km to ensure balance between accumulation and release rates. In addition, they acknowledge that they ignore the fault system geometry that accommodates their regional strain rate. The arbitrary locking depth and lack of fault system geometry limit the applicability of the *WGCEP* moment accumulation estimate.

While *WGCEP* (1995) achieved agreement between moment accumulation and release, their study focused more on probabilistic models and *b*-value methods that favored large earthquake deficits. *Stein and Hanks* (1998) responded to the *WGCEP* (1995) study and included a significant discussion of regional moment balance. Using a modified earthquake catalog they suggested  $10.15 \pm 2.25 \times 10^{18}$  N·m/yr for the mean

moment release rate over the last ~100 years. *Stein and Hanks* (1998) also argued that there was no moment deficit in Southern California based on the moment accumulation associated with widely recognized faults (San Andreas, San Jacinto, Elsinore and Garlock). *Wald* (1998) considered similar moment balance arguments and included a release rate similar to that of Stein and Hanks. Like previous authors, he suggested that there is an approximate balance between accumulation and release rate. However, *Wald's* (1998) moment accumulation rate based on the Petersen et al. (1996) slip rate catalog is ~40% greater than the moment release rate (table 1).

The uncertainty for the moment release rate depends on an uncertainty in the magnitude of the  $M_w = 7.9 \pm 0.1$  Ft. Tejon event. Due to the fact that the moment-magnitude relationship is nonlinear, the moment confidence interval is asymmetric. In the case of the moment accumulation rate uncertainties, the asymmetric confidence intervals are the result of the fact that reported slip rate uncertainties are sometimes larger than their magnitudes (e.g.,  $1 \pm 2$  mm/yr). The maximum slip rate that contributes to moment accumulation rate is 3 mm/yr, while the minimum is 0 mm/yr, not -1 mm/yr.

Our moment accumulation rates are about twice as large as previous estimates by *WGCEP* (1995), *Stein and Hanks*, (1998), and *Wald*, (1998), but in rough agreement with the strain rate based calculation of *Shen-Tu et al.*, (1999). The simplest interpretation of this moment imbalance is that Southern California has had a substantial deficit of large earthquakes over the last two centuries.

Reference	Rate ( $10^{18}$ N·m/yr)	Type	Source
<i>Ekstom and England</i> (1989)	2.2	Release	10 year earthquake catalog
<i>WGCEP</i> (1995)	8.3	Release	Earthquake catalog
<i>WGCEP</i> (1995)	8.3	Accumulation	Plate motion (11km)
<i>Stein and Hanks</i> (1998)	$10.15 \pm 2.25$	Release	Earthquake catalog
<i>Stein and Hanks</i> (1998)	$9.75 \pm 1.75$	Accumulation	Selected faults
<i>Ward</i> (1998)	10.6	Release	Earthquake catalog
<i>Ward</i> (1998)	$12.30 \pm 1.70$	Accumulation	Geodesy (11km)
<i>Ward</i> (1998)	$14.20 \pm 2.00$	Accumulation	Geodesy
<i>Ward</i> (1998)	10.2	Accumulation	Selected faults (11km)
<i>Ward</i> (1998)	11.8	Accumulation	Selected faults
<i>Shen-Tu et al.</i> (1998)	$13.6 \pm 5$	Release	Earthquake catalog
<i>Shen-Tu et al.</i> (1999)	19.9	Accumulation	Strain rate
This study	$10.40^{+1.83}_{-1.29}$	Release	Kagan catalog
This study	$18.97^{+12.11}_{-8.79}$	Accumulation	<i>Petersen et al.</i> (1996) catalog
This study	$21.25^{+4.63}_{-4.42}$	Accumulation	Block model
This study	$17.90^{+3.71}_{-3.62}$	Accumulation	Block model (11km)
This study	$18.48^{+3.66}_{-3.65}$	Accumulation	Block model (11km*)

**Table 1.** Summary of regional moment balance parameters for Southern California. The Source column indicates the data used for the calculation. Sources followed by “(11km)” indicate values estimates that have an arbitrary 11 km locking depth for all of Southern California. The last two rows indicate two different slip rate models both with 11 km locking depths. The lower accumulation rate value is obtained by taking the slip rates from our preferred block model (with variable locking depth) and imposing an 11 km locking depth. The last row (11km\*) uses the slip rates from a model where the slip rates were determined using a uniform 11 km locking depth. This model results in a 30% increase in the fit criteria over our preferred model. The moment accumulation rate is higher due the increase in estimated fault slip rates.

### 5.1. Moment balance challenges

Our regional moment deficit calculation suffers from the same problems as previous studies: defining the geographic extent of Southern California is problematic and the uncertainty in the size of the 1857 Ft. Tejon event leads to a large uncertainty in

the moment release rate. These are not problems specific to the Ft. Tejon earthquake or to Southern California. In fact, the same trouble would be faced anywhere due to the nature of the Gutenberg-Richter (G-R) frequency distribution and the definition of the moment-magnitude relationship. The G-R frequency distribution,  $\log_{10}(N) = a - bM_w$ , is an empirical relationship that gives the number of earthquakes per year,  $N$ , larger than a given magnitude,  $M_w$ . Typically  $b \approx 1$ . However, despite the fact that the largest earthquakes are quite rare, they account for most of the deformation in the fault system. The other important moment-magnitude relationship is given by  $M_w = 0.67 \log_{10} M_0 - 10.7$ , where  $M_0$  is in cgs units (*Hanks and Kanamori, 1979*). This means that a  $M_w = 8$  event releases 30 times more moment than does a  $M_w = 7$  event. In short, regional moment balances will always be severely limited by even a small uncertainty in the magnitude of the maximum size events. Some authors (*WGCEP, 1995, Field et al., 1999*) have suggested that G-R distribution may be truncated with a maximum size event  $M_w^{\max}$ . If this were to be the case, the paleoseismic record may provide important information about these events and allow us to better constrain their magnitudes. The short length of the earthquake record in Southern California is insufficient for these purposes.

Another challenge in regional moment balance estimates is the recognition of different geographic boundaries. While all authors agree that the San Andreas Fault System south of Parkfield and north of the Mexican border is part of Southern California, there is disagreement on whether or not to continue south of the international border into

the Gulf of Mexico and Baja California. The inclusion of the ECSZ is also inconsistent. *WGCEP* (1995), *Wald* (1998), and *Stein and Hanks* (1998) all largely ignore the effects of strain accumulation in this region while counting the moment release from the 1872 Owens Valley earthquake in the same area.

A third obstacle for the regional analysis of moment deficit for seismic hazard assessment is the assumption of a uniform elastic locking depth. Both *WGCEP* (1995) and *Stein and Hanks* (1998) achieve a balance between strain accumulation and release by using a relatively shallow elastic locking depth of 11 km. This has the effect of reducing the moment accumulation rates relative to deeper locking depths. As a rationale for this approach, they appeal to rock mechanics models that suggest that the transition from brittle to ductile behavior should occur at this depth. Presumably, the ductile region is not capable of rupturing coseismically. However, an 11 km locking depth is in direct conflict with the maximum depths observed in recent earthquakes and that estimated for historic earthquakes. *Hudnut et al.* (1996) estimated that the  $M_w = 6.8$  1994 Northridge earthquake ruptured to a depth of at least 16.5 km. Empirical scaling relations (*Wells and Coppersmith*, 1994) suggest that the maximum rupture depth should scale with magnitude as well. *Bawden* (2001) used leveling data to estimate that the 1952 Kern County earthquake ruptured to a depth of 27 km. Further, shallow locking depths are inconsistent with models of interseismic strain accumulation constrained by geodetic observations (*Savage and Lisowski*, 1998, *Meade and Hager* 2004a). Thus, we have at least three geophysical constraints that should preclude us from arbitrarily setting a

regional locking depth in Southern California to ensure a balance between moment accumulation and release.

In summary, there are three parameters that must be known to determine whether the moment accumulation and release rates balance: 1) the size of the 1857 Ft. Tejon earthquake 2) the geographic extent of Southern California, and 3) the regional locking depth. A more rigorous estimate of seismic hazard should not be dependant on the “tuning” of these parameters.

## **6. Spatial localization of moment deficit**

Both the historical earthquake catalogs and the fault slip rate catalogs contain spatial information that we can use to localize regions of moment deficit. We have developed a new method for localizing moment deficits spatially based on comparing historical earthquake catalogs with fault slip rate catalogs. We determine the moment balance throughout Southern California locally in order to identify those faults that have accumulated more strain than they are known to have released over the length of the historical earthquake catalog. It is an appropriate method to search for moment deficits along faults with high slip rates where the recurrence time is comparable to or a few times longer than the span of the historical earthquake catalog.

By looking at the moment balance locally, we can assess not only whether or not there is a deficit but also determine where. Instead of directly estimating the slip deficit we compare the total amount of elastic deformation accumulated by interseismic strain and released by coseismic events. This method’s simplicity and flexibility make it a

powerful new tool for examining both seismic hazard potential and the temporal evolution of fault systems.

In some ways, our spatial localization method is less sensitive to limitations that the regional moment balance analysis suffers from. Specifically it is not sensitive to the geographic definition of Southern California, nor is it as sensitive to the determination of the magnitude of the maximum size events. The reason for this is that while the uncertainty in the magnitude of the Ft. Tejon earthquake is large, the uncertainty in its rupture length is not. *Sieh* (1978) documented the rupture length from the partially creeping segment of the San Andreas Fault near Parkfield in the north to the junction of the San Andreas and San Jacinto Faults in the south. We know that this event did not rupture the southernmost San Andreas. In fact, we have epicenter estimates for all of the major earthquakes since 1807 (*Ellsworth, 1989, Kagan, 2002*). This is the spatial information in the earthquake catalog. The fault system geometry provides the same type of spatial information for the fault slip rate catalogs.

To compare the moment release and accumulation information in the earthquake and slip rate catalogs we convert them both to deformation fields,  $D$ . This intermediary step allows us easily visualize the spatial pattern of moment release and accumulation.

$$D_R(\lambda, \theta) = \sum_I^{\text{earthquakes}} O(\bar{s}_I, \bar{g}_I, \lambda, \theta) \quad (3)$$



where  $\vec{s}$  is the coseismic slip vector,  $\vec{g}$  describes the fault system geometry,  $\lambda$  is longitude, and  $\theta$  is latitude. The function,  $O(\dots)$ , is the analytic solution for an arbitrarily inclined dislocation in an elastic half space (Okada, 1985). We sum over all of the earthquakes included in Kagan's (2002) compilation (figure 2).

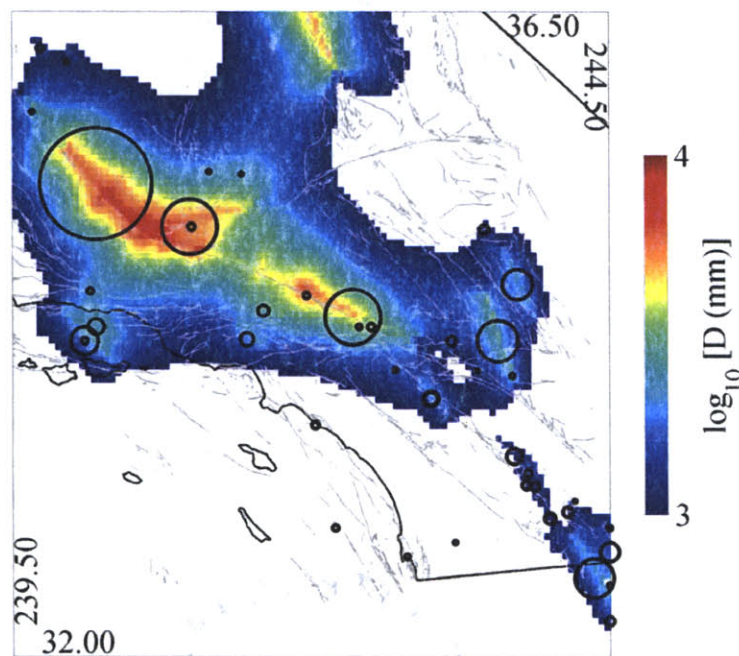


**Figure 2.** Deformation from large earthquakes. The colors show the logarithm of the deformation field. The color map is linear and clipped so that regions with less than 1000 mm of deformation are white. The circles show the location and magnitude of the earthquakes. The area of each circle is proportional to the scalar moment release. The thick dark lines are the coast and state borders for California. The same color map is used for all deformation field figures.

For each earthquake, we convert the focal mechanism estimate to rupture geometry and mean slip using the empirical scaling relations estimated by *Wells and Coppersmith* (1994). The sole exception is the 1857 Ft. Tejon event, for which we use the

geometry and slip distribution detailed by *Sieh* (1978). As the elastic deformation falls off rapidly with distance from the fault ( $d \sim r^{-3}$ ) deformation appears localized around the coseismic events. We plot the base ten logarithm of the deformation in order to show more of a dynamic range. Figure 2 shows the results for our modified version of *Kagan's* (2002) catalog. The areas around the 1812 and 1857 events along the Carrizo and Mojave segments of the SAF have the greatest amount of coseismic deformation. There is a notable lack of deformation along the southern SAF and between the 1872 Owens Valley and the more recent Landers (1992) and Hector Mine (1999) events in the Eastern California Shear Zone.

The total deformation accumulated over the interseismic period is calculated in much the same way as the deformation release.

$$D_A(\lambda, \theta) = \sum_i^{\text{faults}} O(T\bar{v}_i, \vec{g}_i, \lambda, \theta) \quad (4)$$

The difference between equations 3 and 4 is that in the latter the mean earthquake slip,  $\bar{s}$ , has been replaced by the total amount of accumulated slip,  $T\bar{v}$ . The deformation field calculated using the geologically estimated slip rate inventory,  $D_A^{\text{CDMG}}$  (*Petersen et al.* (1996, CDMG)), is shown in figure 3. Figure 4 shows the accumulated deformation field, calculated using the slip rates from the *Meade and Hager* (2004a) block model,  $D_A^{\text{block}}$ .

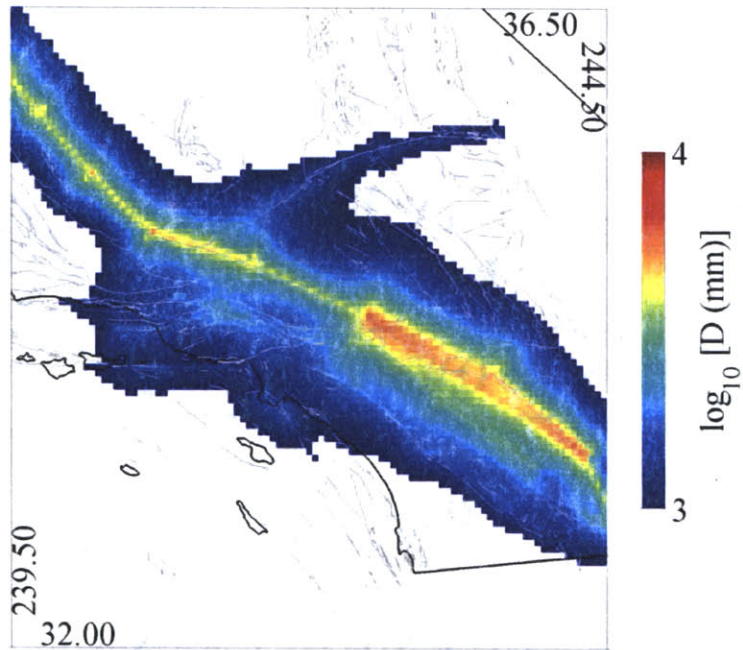


**Figure 3.** Deformation from *Petersen et al.* (1996, CDMG) slip rate catalog. The thin gray lines are the fault traces from *Jennings* (1994). Right lateral shear in the Eastern California Shear Zone is underrepresented compared with the block model slip rate catalog (figure 4).

While deformation is localized along the SAF and SJF in both models, the similarities stop there.  $D_A^{\text{block}}$  shows large amounts of deformation in the ECSZ and along the offshore faults while  $D_A^{\text{CDMG}}$  is devoid any deformation in these regions other than along the Garlock fault at the northern edge of the Mojave Desert. We discuss the differences between the slip rate catalogs in the sections that follow.  $D_A$  is a minimum value, in that we have used a uniform  $T$  that is given by the length of the historical earthquake catalog. Each individual fault segment has been accumulating strain since the time of its last rupture. In certain cases, available paleoseismic data can constrain the

date of the last large event and we discuss the implication of using these refined models where appropriate.

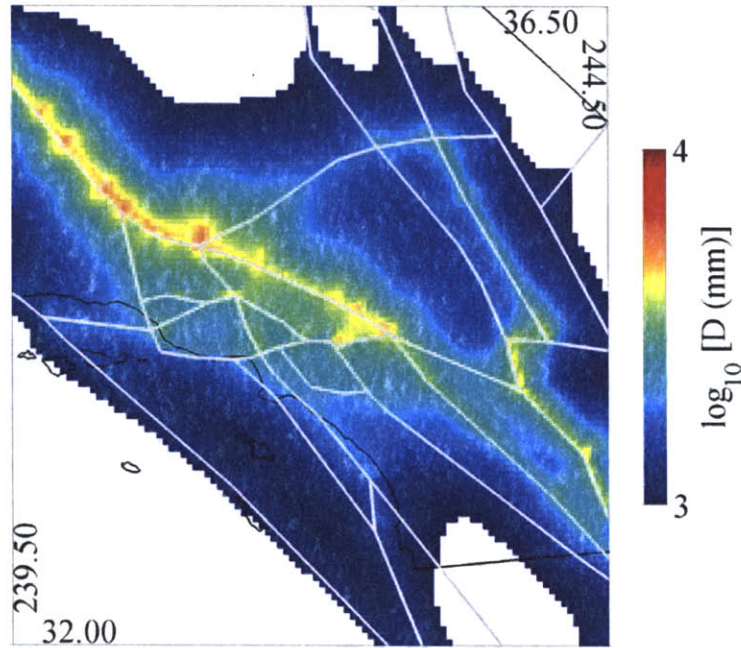


**Figure 4.** Deformation from block model slip rates. The gray lines show the block boundaries from *Meade and Hager (2004a)*. Deformation is localized along the San Andreas Fault, but is non-uniform due to changes in slip rate and locking depth.

Once the deformation release and accumulation fields have been calculated, we difference them to determine those zones that are in balance and those that are not. The difference between the accumulated and released elastic deformation is given by  $\Delta D(\lambda, \theta) = D_A(\lambda, \theta) - D_R(\lambda, \theta)$ .  $\Delta D(\lambda, \theta) < 0$  and  $\Delta D(\lambda, \theta) > 0$  correspond to deformation surplus and deficits respectively. We focus on the areas where deformation deficits,  $\Delta D(\lambda, \theta) > 0$ , are present, as these areas deserved the most attention in terms of our moment balance arguments.

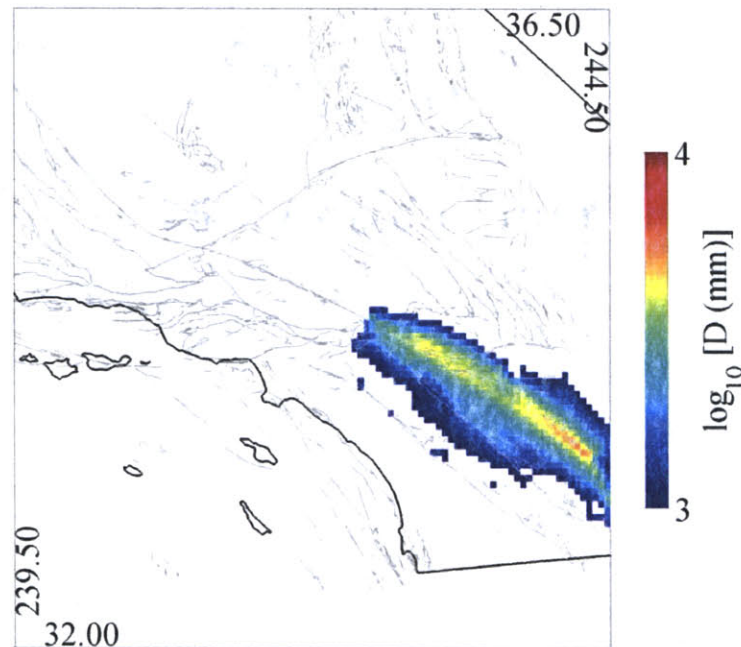


**Figure 5.** Residual deformation (*Petersen et al.* (1996, CDMG) slip rates - Earthquakes). The Southern San Andreas and San Jacinto Faults is the only area of major deformation deficit.

The difference between the *Petersen et al.* (1996) and earthquake deformation fields,  $\Delta D^{\text{CDMG-earthquakes}}$ , (figure 5) is similar with respect to the southern San Andreas Fault System, showing a massive deformation deficit. In fact, the  $\Delta D^{\text{CDMG-earthquakes}}$  shows a larger deformation deficit along the San Bernadino segment of the SAF (SBSAF) due to the fact that the geologically estimated slip rate is four times larger there than that estimated from geodesy (e.g., *Weldon and Sieh*, 1985, *Meade and Hager*; 2004a). The difference in deficit between the block model and earthquake catalogs,  $\Delta D^{\text{blocks-earthquakes}}$ , is shown in figure 6. Three major regions show significant deformation deficits: 1) the

greater Los Angeles area, 2) the Southern San Andreas and San Jacinto Faults and 3) the Northern Mojave Desert. Neither the Mojave nor Carrizo plain segments show any significant moment deficit, as the strain released by the 1812 and 1857 earthquakes outweigh the strain accumulated over the last 200 years. The most important difference between  $\Delta D^{\text{CDMG-earthquakes}}$  and  $\Delta D^{\text{blocks-earthquakes}}$  is lack of deformation deficits in the former around Los Angeles and in the Mojave. The *Petersen et al.* (1996) catalog has much less localized slip in both of these areas than does the block model derived slip rate catalog.

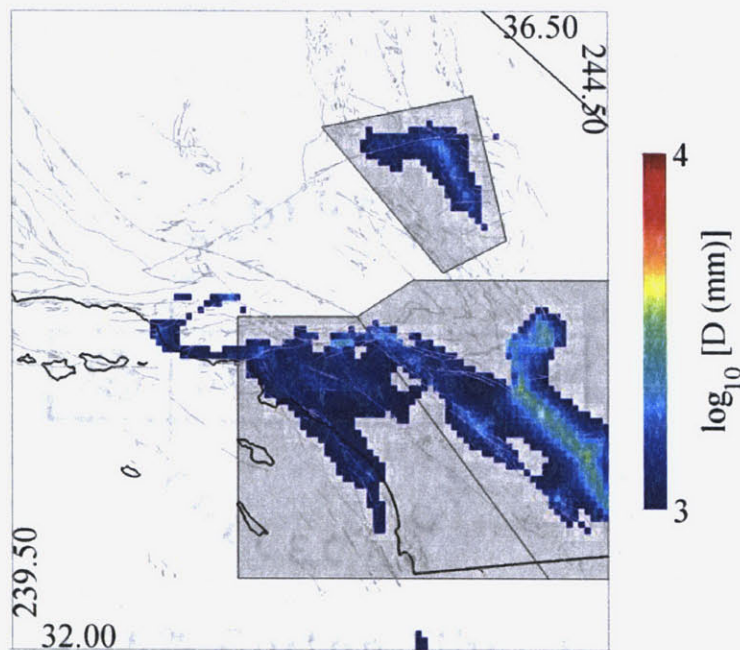


**Figure 6.** Residual deformation (Block model slip rates - Earthquakes). There are three major areas of deformation deficit: Northern Mojave, Los Angeles, and the Southern San Andreas and San Jacinto Faults. The gray shaded regions show the limits of each region as defined for the source estimation procedure.

The deformation field approach to localizing moment deficit has several distinct advantages. First, it allows for a degree of spatial smoothing. That is, we do not have to exactly align the earthquake rupture and fault system geometries. For example the 1952  $M_w = 7.5$  Kern County Earthquake occurred on the south dipping White Wolf fault. This fault is not present in the *Meade and Hager* (2004a) block model, but the shortening associated with it is accommodated on the nearby SAF and Garlock faults to the south. Our deformation field method consists of displacement fields where the effects of neighboring structures may overlap.

We also calculate regions of significant deformation surplus (figure 7). These are regions where the amount of coseismic deformation significantly exceeds the amount of accumulated interseismic deformation. The fraction of Southern California that has a deformation surplus (figure 6) is smaller than the fraction that has a deformation deficit (figure 7). The three largest areas of deformation surplus are the confluence of the 1857 and 1952 rupture zones to the north of the Big Bend, the area around the 1872 earthquake in Owens Valley, and the Mojave SAF, where the 1812 and 1857 events overlap. The deformation surplus around the FTSAF is not surprising as the recurrence interval (e.g., *Sieh et al.*, 1989) is comparable the length of the historical earthquake catalog. The Owens Valley fault slip rate is an order of magnitude lower and has a much longer recurrence interval (e.g., *Beanland and Clark*, 1994). It would take roughly two thousand years to eliminate this deformation deficit. The White Wolf fault (location of the 1952

Kern County earthquake) provides another example of a fault with a long recurrence interval that has ruptured recently (e.g., *Stein and Thatcher, 1981*).

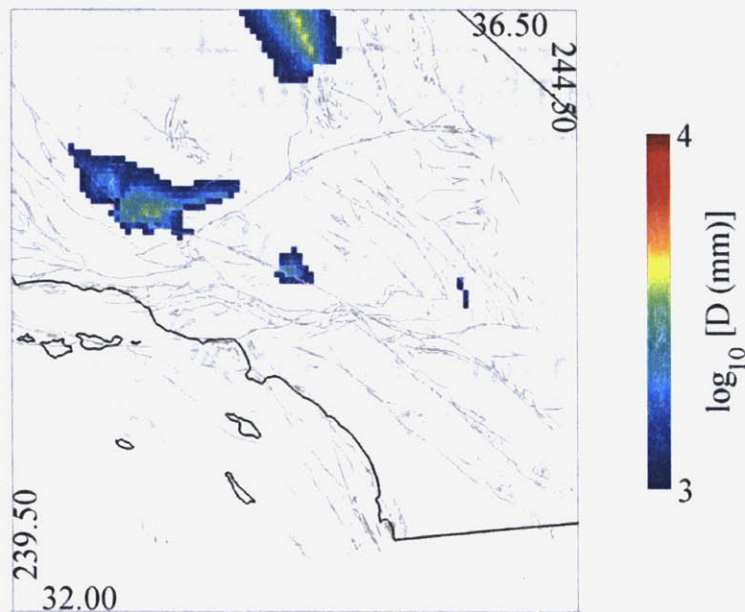


**Figure 7.** Regions of deformation surplus. There three major areas of deformation surplus are localized around the 1812 SAF event, the 1872 Owens Valley epicenter and the high slip regions of the 1857 Ft. Tejon and 1952 Kern County earthquakes.

## 7. Minimum earthquake source estimates

### 7.1. Source estimation method

The regions of deformation deficit in figure 6 show where earthquake activity falls substantially below the estimated interseismic deformation over the last 200 years. If strain has been accumulating regularly, and if there were no moment deficits prior to 1800, then we could interpret the deformation deficit map (figure 6) as the amount of deformation that has not been balanced coseismically. If any of these fault segments



experienced large ( $M_w > 7.5$ ) earthquakes immediately prior to 1800, then they could still be in a state of coseismic deformation surplus. Some of these fault segments may be early in the quiescent period of a clustered seismic cycle. With this type of strain accumulation and release model, moment is balanced over a longer clustered earthquake cycle, not in a single earthquake cycle (e.g., *Meade and Hager, 2004b*).

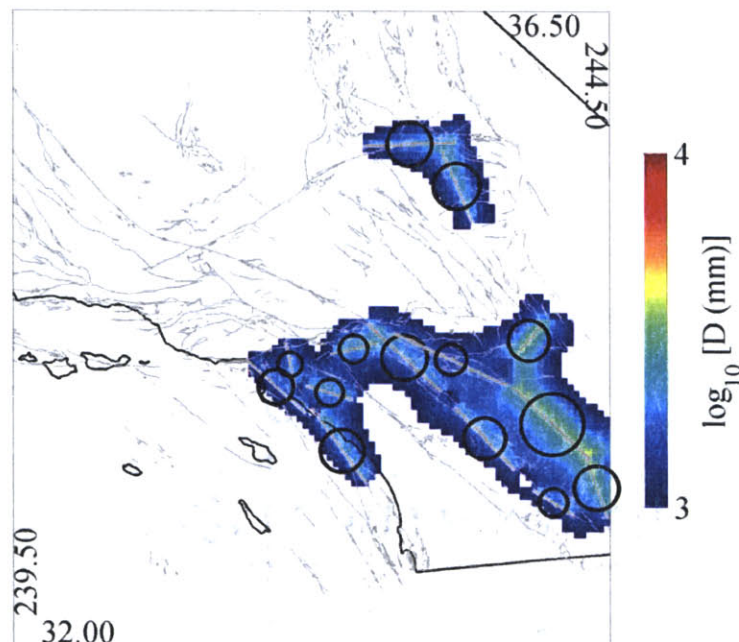


**Figure 8.** Estimated source locations and deformation. There are 14 sources in three regions (Northern Mojave, Los Angeles, and Southern San Andreas and San Jacinto Faults). The source magnitudes are summarized in table 2.

The simplest interpretation of the deformation deficit field is that it is the amount of accumulated deformation that has not been released coseismically. In order to interpret this information in terms of the potential for future earthquakes we must convert

from deformation deficit to moment deficit. To do this we estimate the minimum earthquake sources that could relieve the estimated deformation deficit. This potential source forecast is consistent with the location of known faults, the historical earthquake catalog, modern geodetic data, and simple models of interseismic strain accumulation. We can readily convert the estimated earthquake source parameters into scalar moments and moment magnitudes. The results are summarized in table 2 and figure 8.

*Shen-Tu et al.*, (1999) estimated a set of sources using a moment accumulation model based on integrating strain rate models derived from geologic slip rate estimates. This approach lacks a realistic physical mechanism for strain accumulation and forces the comparison between Quaternary slip rate estimates and seismicity to be done over the last 150 years. This comparison may be inappropriate, as fault slip rates may change substantially over times scales less than a million years long, and possibly as short as the Holocene (e.g., *Sharp*, 1981, *Friedrich et al.*, 2003). Further, the geologically determined slip rate catalog used by *Shen-Tu et al.* (1999) does not satisfy path integral constraints and severely under-represents the amount of active fault system in the Los Angeles region. An additional problem with the *Shen-Tu et al.* (1999) approach is that it suffers from an error in logic concerning strain rate. They equate high strain rates with high moment accumulation rates. This is not necessarily the case, as the highest strain rates are observed around creeping faults where there is a large velocity jump over a very short distance. In fact, there is little or no moment accumulation associated with these creeping sections. As a result, *Shen-Tu et al.* (1999) estimate one of their large potential earthquake sources along the creeping section of the San Andreas Fault north of

Parkfield. Despite these problems, the *Shen-Tu et al. (1999)* source estimates for the Southern San Andreas Fault are somewhat similar to ours, as they also recognize the dearth of coseismic moment release over the last two centuries.

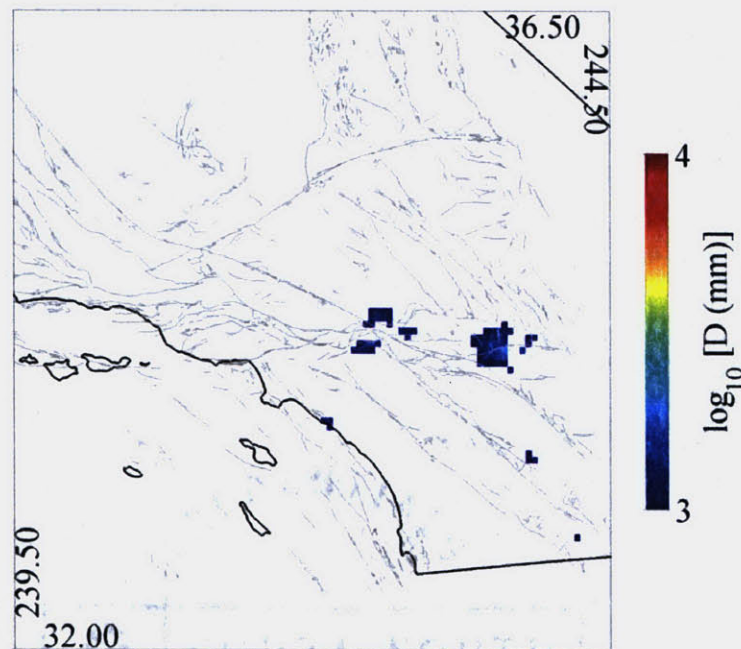


**Figure 9.** Residual deformation (Block model accumulation – (Historical earthquakes + estimated sources). Note that the Ventura deficit disappears despite the fact that we did not model a source there.

In general, we are able to model the deformation deficits quite well with sources that lie on or near the traces of major faults. We use a nonlinear gradient-based search technique (e.g., *Gill et al., 1981*) that allows the source position, length, orientation and slip to vary from an initial set of parameters closely aligned to the major fault zones. The

resulting residual field,  $D'(\lambda, \theta)$ , is calculated by differencing both the historical earthquake catalog and the estimated sources from the fault slip rate catalog (figure 8)

$$D' = D_A^{\text{block model}} - (D_R^{\text{historical earthquakes}} + D_R^{\text{estimated sources}}) \quad (5)$$

The residual deformation field is shown in figure 9. Typical residual deformation magnitudes are less than 2 mm/yr over the last two centuries.

Source	Magnitude	Moment ( $10^{20}$ N·m)
Los Angeles Area (total)	7.6	2.60
Oceanside	7.3	0.92
Newport - Inglewood	7.2	0.59
PHT (east)	7.0	0.38
PHT (west)	7.0	0.31
Sierra Madre (south)	7.0	0.41
Northern Mojave (total)	7.4	1.37
Goldstone	7.2	0.71
Garlock	7.2	0.66
Southern San Andreas & San Jacinto Faults (total)	7.8	5.20
San Bernadino SAF	7.0	0.39
Salton (Indio) SAF	7.4	1.50
Brawley SAF	7.2	0.78
Eureka Peak	7.2	0.66
San Jacinto (north)	7.2	0.81
San Jacinto (central)	7.2	0.69
San Jacinto (south)	7.0	0.32

**Table 2.** Minimum source estimates. The shaded rows give the cumulative magnitude and moment for each of the three major source areas. The source magnitudes and moments are for the source locations shown in figure 8.

We estimate the sources for the three regions identified in figure 6. Each region is defined by a relatively contiguous deformation deficit map. The three regions are: 1) Los Angeles area including the offshore faults 2) the Northern Mojave Desert and Eastern

Garlock, and 3) the Southern San Andreas and San Jacinto Faults. Summing the moment contribution from each of these regions we find  $M_0^{\text{sources}} = 9.2 \times 10^{20}$  N·m. If these hypothetical sources had occurred over the time span covered by the earthquake catalog, they would increase the mean annual moment release rate by  $4.8 \times 10^{18}$  N·m/yr, bringing the total to  $15.2 \times 10^{18}$  N·m/yr. This value overlaps with the moment accumulation estimates within their  $1\text{-}\sigma$  uncertainties. Additional sources in the Southern Ventura Basin and along the offshore fault system (e.g., San Clemente) could account for the rest of the deficit. Due to poor knowledge of the fault system geometry and earthquake record (especially offshore), we do not explicitly estimate sources for these structures. The Southern San Andreas and San Jacinto Faults are clearly the largest sources of moment deficit using both the block model and CMDG slip rate catalogs.

## 7.2. Southern San Andreas and San Jacinto Faults

For the region defined as the Southern San Andreas and San Jacinto Faults, we find a massive moment deficit of  $5.20 \times 10^{20}$  N·m, corresponding to an equivalent moment magnitude of 7.8. The  $\Delta D^{\text{CMDG-earthquakes}}$  field shows an even larger deformation deficit than the  $\Delta D^{\text{blocks-earthquakes}}$  used for the source estimation. Note that the moment deficit we estimate is nearly as large as the moment accumulation and release rates reported by *WGCEP* (1995), *Stein and Hanks* (1998), and *Wald* (1998). Our source model includes 7 segments (San Bernadino SAF ( $M_w = 7.0$ ), Salton SAF ( $M_w = 7.4$ ), Brawley SAF ( $M_w = 7.2$ ), Eureka Peak-Pinto Mountain Fault ( $M_w = 7.2$ ), Northern SJF ( $M_w = 7.2$ ), Central

SJF ( $M_w = 7.2$ ), and Southern SJF ( $M_w = 7.0$ )). Each of the potential sources lies close to a mapped fault trace. It is not clear that any individual segment that we have defined should define the limits of a given rupture. It may be the case that any of our segments will not rupture in a single large earthquake, but instead will accommodate the same deformation through several smaller events. Conversely, very large ruptures might rupture across the segments in cascades (e.g., *WGCEP 1995, Field et al., 1999*)

The largest estimated individual source is the Salton SAF, which we estimate to have  $M_w = 7.5$ , with a mean slip of 5.8 meters. Just to the north, our Eureka Peak source lies near the epicenter of the 1992 Joshua Tree earthquake ( $M_w = 6.1$ ) and is responsible for transferring deformation from the SAF to the ECSZ. We estimate a potential  $M_w = 7.1$  source for the San Bernadino SAF. This is smaller than the  $M_w = 7.4$  estimate from *Meade and Hager (2004a)*, who used a 330 year mean recurrence interval for the last two millennia and a deeper locking depth.

With this massive potential moment release, we should consider alternative explanations. What about the possibility that the Southern San Andreas and San Jacinto Faults are not presently accumulating strain, but are instead creeping? Recent studies have documented active fault creep on both segments using radar interferometry (e.g., *Lyons and Sandwell, 2003, Vincent, 2000*). *Meade and Hager (2004a)* argued that the *Lyons and Sandwell (2003)* partial creep model is incompatible with the GPS-determined velocities north of the Salton Sea. Even if this were not the case, the *Lyons and Sandwell (2003)* model still requires at least 5 km of locked fault that would reduce our moment accumulation estimate by a third on a small segment of the SAF. *Vincent (2000)*

presented interferometric evidence for quiet earthquakes on the southern SJF (Superstition Hills segment), but only enough to account for a few  $M_w = 5.3-5.6$  size events. Extension and elevated heat flow suggest an elevated geotherm south of the Salton Sea (e.g., *Doser and Kanamori, 1986*). One possible consequence of an elevated geotherm would be to raise the depth of the brittle-ductile transition and yield a smaller effective locking depth. While this may be the case, *Doser and Kanamori (1986)* demonstrated that microseismicity is present down to at least 15 km.

Modern GPS data also allow us to constrain how deeply a fault system appears to be locked. *Meade and Hager (2004a)* presented a preferred slip rate and locking depth model for Southern California that included locking depths for the Southern SAF-SJF system that ranged from 10-15 km. We reconsider the possibility of shallower locking depths on these faults by redoing the same calculation over a range of different locking depths. Figure 10 shows the residual fit criteria,  $\chi^2$ , and total moment accumulation rate as a function of the locking depth on the Southern San Andreas and San Jacinto Faults. A 12 km locking depth fits the data best and is in agreement with the mean locking depth used by *Meade and Hager (2004a)* (10 km for the San Jacinto, 15 km for the San Andreas). The case where both the southern SAF and SAF are creeping has the effect of increasing the misfit criteria,  $\chi^2$ , by 120% (1.223 vs. 2.697) and still fails to alleviate the moment deficit imbalance at the regional scale (table 1). Thus, we find that shallow locking depths and large amounts of aseismic creep are highly incompatible with most geodetic observations of interseismic deformation. Paleoseismic evidence also suggests that the Southern SAF has generated large earthquakes over the last two thousand years

(Sieh, 1986, Sieh and Williams, 1987, Yule and Sieh, 2000). Our estimated magnitudes are almost certainly underestimates, in the sense that the estimated time of the last known rupture of the Salton (Indio) segment is nearly 350 years ago (Sieh and Williams, 1990).

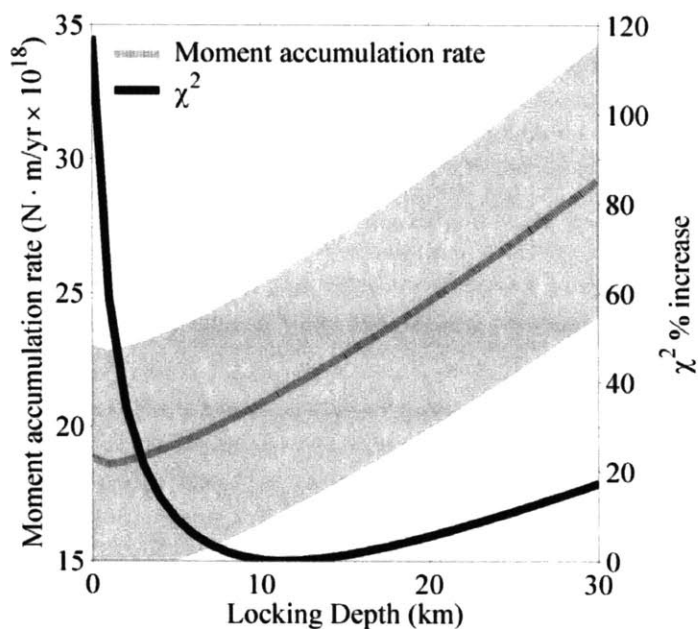


**Figure 10.** Moment accumulation rate variation with locking depth. The locking depths that we vary here are for the San Jacinto and San Andreas Faults. The dashed line shows the moment accumulation rate as a function of locking depth. We calculate the uncertainty interval (shaded region) by propagating the formal slip uncertainty estimates. The Imperial Fault is creeping in all models. The percentage increase in the misfit criteria is shown on the right hand side axis. The minimum mean locking depth for both the San Jacinto and San Andreas Faults is 12 km.

### 7.3. Northern Mojave

The northern Mojave moment deficit region corresponds to the coseismic gap between the 1872 Owens Valley earthquake and the more recent 1992 Landers and 1999 Hector Mine events. Our preferred source estimation also includes two sources: an



eastern Garlock source ( $M_w = 7.2$ ) and a Goldstone Lake Fault source ( $M_w = 7.2$ ). However, it is difficult to deconvolve the right lateral ECSZ shear strain from the left lateral Garlock shear strain, which are oriented nearly normal to each other. *Meade and Hager's* (2004a) slip rate model localizes right lateral deformation on the Blackwater and Goldstone faults with 4 and 13 mm/yr respectively. The strike slip rate for both faults is likely influenced by the suspected presence of postseismic deformation at nearby sites. Note, however, that *Sauber et al.* (1994) analyzed triangulation and VLBI data and found high strain rates in the Mojave Desert prior to the Landers earthquake, suggesting that the more recent deformation rate estimates cannot be explained by postseismic relaxation alone. *Meade and Hager's* (2004a) model ensures that the total slip budget across the eastern Mojave is compatible with the relative motion between the western Mojave block and the North American Plate. *Peltzer et al.'s* (2001) InSAR study of the ECSZ also provides evidence for  $7 \pm 3$  mm/yr of deformation along the Blackwater Fault. In summary, both radar interferometry and block models of GPS determined velocities in the northern Mojave Desert suggest that there is more than 10 mm/yr of deformation that may be localized on either the Blackwater or Goldstone faults. The simplified geometry used in the *Meade and Hager* (2004a) block model may have artificially localized deformation on the Blackstone and Goldstone faults however the region of moment deficit may be larger.

#### 7.4. Los Angeles

We model the differential deformation field,  $\Delta D^{\text{blocks-earthquakes}}$ , in the Los Angeles area using five sources (figure 6): Oceanside ( $M_W = 7.3$ ), Southern Sierra Madre ( $M_W = 7.0$ ), Newport – Inglewood ( $M_W = 7.2$ ), Eastern Puente Hills Thrust ( $M_W = 7.0$ ), and Western Puente Hills Thrust ( $M_W = 7.0$ ). All faults dip to the east – northeast. The modeled differential deformation (figure 8) shows relatively little localization, thus the location of the potential sources is not unique. However, this set of sources is able to account for the moment imbalance with slip on known structures. The magnitudes for the two PHT sources may be over estimated by as much as a third, as the coseismic model assumes that the faults propagate to the surface in contrast to both the geologic evidence (*Shaw et al.*, 2002) and the moment accumulation model (*Meade and Hager*, 2004a). The offshore Oceanside source may have been partially relieved by an earthquake just prior to start of the historical earthquake catalog (*Grant et al.*, 2002, *Grant and Rockwell*, 2002).

*Dolan et al.* (1995) highlighted the seismic hazard potential in the greater Los Angeles area by summarizing the available faults with surface area sufficient to generate large earthquakes. We agree with the *Dolan et al.* (1995) assessment that there has been a lack of earthquakes over the last century, and estimate that the total moment deficit is as large as  $2.60 \times 10^{20}$  N·m (equivalent moment magnitude,  $M_W = 7.6$ ). Paleoseismic work along the Sierra Madre Fault (*Rubin et al.*, 1998) provides evidence for two  $M_W = 7.2 - 7.6$  events over the last two 15,000 years. Our short Sierra Madre-like source is south of the *Rubin et al.* (1998) study area, but our slip estimate is compatible with that observed.

However, we suggest that it slips much more quickly than the paleoseismic slip and recurrence intervals would suggest. The fault may behave differently north of its juncture with the Raymond Hill fault at the northern edge of the Los Angeles Basin. The Meade and Hager (2004a) block model vastly simplifies the complex geometry of the Sierra Madre fault zone. In reality, there may be several low slip rate faults, each with sufficient surface area to accommodate large, yet infrequent earthquakes. Regardless, our results demonstrate that there are at least four faults with sufficient surface area and accumulated strain to presently accommodate  $M_w > 7$  earthquakes underneath metropolitan Los Angeles.

## 8. Discussion

The potential earthquake sources estimated in the previous sections are minimum values in the sense that we have only integrated the moment accumulation rates over only two centuries. Individual fault segments (such as the SBSAF) may have been accumulating strain even longer. A more direct calculation of moment deficit would involve the use of the time since the last known rupture on each fault zone. Paleoseismic investigations often produce these results, as well as mean recurrence intervals (e.g., *Sieh et al.*, 1989, *Rubin et al.*, 1998, *Yule and Sieh*, 2000). However, the magnitudes, extent, and slip distributions of prehistoric events are not well determined.

It may be the case that the present day strain accumulation is relieved by slow or silent earthquakes. That is, events that slip too slowly to radiate energy dynamically as structurally damaging seismic waves. Large,  $M_w = 7$ , oceanic events have been studied

and documented using continuous GPS time series (e.g., *McGuire and Segall, 2003*). Comparable large events have not been discovered in the continental lithosphere. *Linde et al. (1996)* described a  $M_w = 4.8$  event observed in strain meter data along the San Andreas Fault south of San Francisco and *Vincent (1998, 2000)* detailed a  $M_w = 5.3 - 5.6$  creep episode on the southern most portion of the San Jacinto Fault (Superstition Hills).

If there are large silent earthquakes, then how many should we expect to have seen over the last 15 years of high precision GPS measurements capable of recognizing these events? Assuming silent earthquakes follow a G-R style frequency distribution, we would anticipate approximately 2-3 detectable  $M_w = 6.0$  events over the past 15 years ( $a = 5.5/2$ ,  $b = 1$ ,  $M_w = 8.0$  recurs every 315 years whether silent or not). We use an atypically small  $a$  value to account for the fact that perhaps only half of the seismic activity is accommodated through silent earthquakes. We know of no observational evidence for these earthquakes, and we doubt that these events could have passed unnoticed in GPS time series in densely instrumented Southern California. However, if these faults only have large ( $M_w > 7$ ) characteristic events (e.g., *Sieh, 1996*) there is a smaller probability that they have occurred during the instrumented period. The lack of recognized observations of silent continental earthquakes worldwide suggests that this is not a likely mechanism to balance the moment accumulation and release rates. Further, the bulk of the upper crust is thought to be conditionally stable (velocity strengthening) in terms of the temperature dependant rate-state friction models (e.g., *Scholz, 1998*) unlike the conditions inferred for deep silent earthquakes in subduction zones (e.g., *Dragert et al., 2001, McGuire and Segall, 2003*). Thus, the most physically consistent mechanism

for alleviating localized moment deficits in Southern California is through a series  $M_w > 7$  coseismic events.

*Meade and Hager* (2004b; Chapter 2) presented a model for viscoelastic deformation through a clustered earthquake cycle. They showed that during the long quiescent period of a clustered earthquake cycle, the velocity profile across a fault may be faster than the steady state prediction, even a long time after the last active-period earthquake. This might seem to suggest an alternative explanation for high moment accumulation rates predicted from the block model: the slip rates are overestimated due to the effects of viscoelastic relaxation in a clustered earthquake cycle. If the southern San Andreas Fault system and the faults surrounding the Los Angeles basin have all been dormant for a long time, they might be in a quiescent period. However, the block model approach employed by Meade and Hager (2004a) enforces a path integral constraint that minimizes chances of this effect being significant. The path integral constraint ensures that if a slip rate on one fault is high (due to relaxation) then some other fault must be slow to offset this difference. Thus, the slip rate on an individual fault may be affected by long-term relaxation, but the total slip budget will be approximately constant.

## 9. Conclusions

We have shown substantial evidence supporting the hypothesis that there has been a coseismic moment release deficit in Southern California over the last two centuries. Previous estimates have shown ways in which regional moment balance may be achieved at the cost of contradicting geologic and geophysical observations. It seems that this is an inevitable consequence of the lack of large earthquakes along the Southern San Andreas

Fault system and through the Transverse Ranges. We developed a new method for localizing regions of moment deficit by differencing spatial maps of deformation accumulation and release. These deformation maps can be used to estimate the source parameters for future earthquakes that would alleviate the deficit. We find that the Northern Mojave Desert, the greater Los Angeles Area, and the southern San Andreas and San Jacinto Faults show composite moment deficits equivalent to moment magnitude 7.4, 7.6, and 7.8 events, respectively.

Massive amounts of fault creep and large silent earthquakes could balance to moment budget without the need for coseismic deformation. The search for these phenomena will require an abundance of new geodetic data with far greater spatial and temporal density than is currently available.

**References**

- Bawden, G., Source parameters for the 1952 Kern County earthquake, California: A joint inversion of leveling and triangulation observations, *J. Geophys. Res.*, *106*, 771-785, 2001.
- Bawden, G. W., W. Thatcher, R. S. Stein, K. W. Hudnut, and G. Peltzer, Tectonic contraction across Los Angeles after removal of groundwater pumping effects, *Nature*, *412*, 812-815, 2001.
- Beanland, S., and M. M. Clark, The Owens Valley fault zone, eastern California, and surface faulting associated with the 1872 earthquake, *U. S. Geol. Surv. Bull.*, *1982*, p. 29, 1994.
- Ben-Zion, Y., On Quantification of the Earthquake Source, *Seis. Res. Lett.*, *72*, 151-152, 2001.
- Dolan, J. F., K. Sieh, T. K. Rockwell, R. S. Yeats, J. Shaw, J. Suppe, G. J. Huftile, E. M. Gath, Prospects for Larger or More Frequent Earthquakes in the Los Angeles Metropolitan Region, *Science*, *267*, 199-205, 1995.
- Doser, D., and H. Kanamori, Depth of seismicity in the Imperial Valley region (1977-1983) and its relationship to heat flow, crustal structure and the October 15, 1979, earthquake, *J. Geophys. Res.*, *91*, 675-688, 1986.
- Dragert, H., K. Wang, and T. S. James, A silent slip event on the deeper Cascadia subduction interface, *Science*, *292*, 1525-1528, 2001.
- Ekstom, G. and P. England, Seismic Strain Rates in Regions of Distributed Continental Deformation, *J. Geophys. Res.*, *94*, 10,231-10,257, 1989
- Ellsworth, W. L., Earthquake history, 1769-1989, Wallace, R. E. ed., The San Andreas fault system, California, U. S. Geological Survey Professional Paper, P 1515, 153-187, 1990.
- Field, E. H., D. D. Jackson, and J. F. Dolan, A Mutually Consistent Seismic-Hazard Source Model for Southern California, *Bull. Seis. Soc. Am.*, *89* (3), 559-578, 1999.
- Friedrich, A. M., B. P. Wernicke, N. Niemi, R. A. Bennett, and J. L. Davis, Comparison of geodetic and geologic data from the Wasatch region, Utah, and implications for the spectral character of Earth deformation at periods of 10 to 10 million years, *J. Geophys. Res.*, *108*, doi:10.1020/2002JB000682, 2003.

Gill, P.E., W. Murray, and M.H. Wright, *Practical Optimization*, London, Academic Press, 1981.

Grant, L. B., and K. E. Sieh, Paleoseismic evidence of clustered earthquakes on the San Andreas Fault in the Carrizo Plain, California, *J. Geophys. Res.*, *99*, 6819-6841, 1994.

Grant, L. B., and T. K. Rockwell, A Northward-propagating Earthquake Sequence in Coastal Southern California? *Seis. Res. Lett.*, *73*, 461-469, 2002.

Grant, L. B., L. J. Ballenger and E. E. Runnerstrom, Coastal uplift the San Joaquin Hills, southern Los Angeles Basin, California, by a large earthquake since 1635 A.D., *Bull. Seis. Soc. Am.*, *92*, 590-599, 2002.

Hanks, T. C., and H. Kanamori, A moment magnitude scale, *J. Geophys. Res.*, *84*, 2348-2350, 1979.

Hough, S. E., Earthquakes in the Los Angeles Metropolitan Region: A Possible Fractal Distribution of Rupture Size, *Science*, *267*, 211-213, 1995.

Hudnut, K. W., Z. Shen, M. Murray, S. McClusky, R. King, T. Herring, B. Hager, Y. Feng, P. Fang, A. Donnellan, and Y. Bock, Co-seismic displacements of the 1994 Northridge, California, earthquake, *Bull. Seis. Soc. Am.*, *86*, 19-36, 1996.

Linde, A. T., M. T. Gladwin, M. J. S. Johnston, R. L. Gwyther, and R. G. Bilham, A slow earthquake sequence on the San Andreas fault, *Nature*, *383*, 65-68, 1996.

Marratt, R. and R. W. Allmendinger, Amount of extension on "small" faults: An example from the Viking graben, *Geology*, *20*, 47-50, 1992.

Meade, B. J., B. H. Hager, S. C. McClusky, R. E. Reilinger, S. Ergintav, O. Lenk, A. Barka, and H. Ozener, Estimates of Seismic Potential in the Marmara Sea Region from Block Models Secular Deformation Constrained by Global Positioning System Measurements, *Bull. Seis. Soc. Am.*, *92*, 208 - 215, 2002.

Meade, B. J., and B. H. Hager, Block Models of Present Day Deformation in Southern California Constrained by Geodetic Data, in preparation, 2004a.

Meade, B. J., and B. H. Hager, Viscoelastic Deformation for a Clustered Earthquake Cycle, in preparation, 2004b.

McGuire, J. J., and P. Segall, Imaging of aseismic fault slip transients recorded by dense geodetic networks, *Geophys. J. Int.*, *155*, 778-788, 2003.

Minster, B., and T. H. Jordan, Vector constraints on western U.S. deformation from space geodesy, neotectonics, and plate motions, *J. Geophys. Res.*, *92*, 4798 - 4804, 1987.



Murray, J. and P. Segall, Testing the time-predictable earthquake recurrence by direct measurement of strain accumulation and release, *Nature*, 419, 287-291, 2002.

Okada, Y. Surface deformation due to shear and tensile faults in a half space, *Bull. Seis. Soc. Am.*, 75, 1135-1154, 1985.

Peltzer, G., F. Crampe, S. Hensley, and P. Rosen, Transient strain accumulation and fault interaction in the Eastern California shear zone, *Geology*, 29, 975 - 978, 2001.

Petersen, M. D., and S. G. Wesnousky, Fault Slip Rates and Earthquake Histories for Active Faults in Southern California, *Bull. Seis. Soc. Am.*, 84 (5), 1608-1649, 1994.

Petersen, M. D., W. A. Bryant, C. H. Cramer, T. Cao, and M. S. Reichle, A. D. Frankel, J. J. Lienkaemper, P. A. McCrory, and D. P. Schwartz, Probabilistic seismic hazard assessment for the State of California, Calif. Div. Mines and Geol. Open file Rep. 96-08 and U. S. Geol. Surv. Open File Rep. 96-706, <http://www.consrv.ca.gov/CGS/rghm/psha/ofr9608/index.htm>, 1996.

Rubin, C. M., S. C. Lindvall, T. K. Rockwell, Evidence for Large Earthquake in Metropolitan Los Angeles, *Science*, 281, 398 - 402, 1998.

Sauber, J., W. Thatcher, S. C. Solomon, and M. Lisowski, Geodetic slip rate for the Eastern California shear zone and the recurrence time of Mojave Desert earthquakes, *Nature*, 367, 264 - 266, 1994.

Scholz, C. H., Earthquakes and friction laws, *Nature*, 391, 37-42, 1998.

Scholz, C. H., and P. A. Cowie, Determination of total strain from faulting using slip measurements, *Nature*, 346, 837-839, 1990.

Sharp, R. V., Variable Rates of Late Quaternary Strike Slip on the San Jacinto Fault Zone, Southern California, *J. Geophys. Res.*, 86, 1754 - 1762, 1981.

Shaw, J. H., Cracking Los Angeles, *Nature*, 394, 320-321, 1998.

Shaw, J. H., and P. M. Shearer, An Elusive Blind-Thrust Fault Beneath Metropolitan Los Angeles, *Science*, 283, 1516-1518, 1999.

Shaw, J. H., A. Plesch, J. F. Dolan, T. L. Pratt, and P. Fiore, Puente Hills blind-thrust system, Los Angeles, California, *Bull. Seis. Soc. Am.*, 92, 2946-2960, 2002.

Shen-Tu, B., W. E. Holt, and A. J. Haines, Contemporary kinematics of the western United States determined from earthquake moment tensors, very long baseline interferometry, and GPS observations, *J. Geophys. Res.*, 103, 18,087-18,117, 1998.

Shen-Tu, B., W. E. Holt and A. J. Haines, Deformation kinematics in the western United States determined from Quaternary fault slip rates and recent geodetic data, *J. Geophys. Res.*, 104, 28,927-28,955, 1999.

Sieh, K. E., Slip along the San Andreas Fault associated with the great 1857 earthquake, *Bull. Seis. Soc. Am.*, 68 (5), 1421-1447, 1978.

Sieh, K., Slip rate across the San Andreas fault and prehistoric earthquakes at Indio, California, *Eos Trans. AGU*, 67, 1200, 1986.

Sieh, K., The repetition of large-earthquake ruptures, *Proc. Natl. Acad. Sci. USA*, 93, 3764-3771, 1996.

Sieh, K. E., and R. H. Jahns, Holocene activity of the San Andreas Fault at Wallace Creek, California, *Geol. Soc. Am. Bull.*, 95, 883-896, 1984.

Sieh, K. E., and P. L. Williams, Behavior of the Southernmost San Andreas Fault During the Past 300 Years, *J. Geophys. Res.*, 95, 6629-6645, 1990.

Stein, R. S., and T. C. Hanks,  $M \geq 6$  Earthquakes in Southern California during the Twentieth Century: No Evidence for a Seismicity or Moment Deficit, *Bull. Seis. Soc. Am.*, 88, 635-652, 1998.

Stirling, M. W. and S. G. Wesnousky, Do Historical Rates of Seismicity in Southern California Require the Occurrence of Earthquake Magnitudes Greater Than Would be Predicted from Fault Length?, *Bull. Seis. Soc. Am.*, 87 (6), 1662-1666, 1997.

Vincent, P., J.B. Rundle, R. Bilham, and S.M. Buckley, Aseismic creep along the San Andreas and Superstition Hills faults with uplift at Durmid Hill, southernmost San Andreas fault, CA measured by radar interferometry, *EOS Trans., AGU*, 79, 45, 1998.

Vincent, P., Aseismic Slip Events along the Southern San Andreas Fault System Captured by Radar Interferometry, Proceeding of the 3rd Conference on Tectonic Problems of the San Andreas Fault System, <http://pangea.stanford.edu/GP/sanandreas2000>, 2000.

Walls, C., T. Rockwell, K. Mueller, Y. Bock, S. Williams, J. Pfanner, J. Dolan, and P. Fang, Escape tectonics in the Los Angeles metropolitan region and implications for seismic risk, *Nature*, 394, 356-360, 1998.

Ward, S. N., A Multidisciplinary Approach to Seismic Hazard in Southern California, *Bull. Seis. Soc. Am.*, 84 (5), 1293-1309, 1994.

Ward, S. N., On the consistency of earthquake moment rates, geologic fault data, and space geodetic strain: the United States, *Geophys. J. Int.*, 134 (1), 172-186, 1998.

Ward, S. N., A deficit vanished, *Nature*, 394, 827-829, 1998.

Weldon, R. J., and K. E. Sieh, Holocene rate of slip and tentative recurrence interval for large earthquakes on the San Andreas Fault, Cajon Pass, Southern California, *Geol. Soc. Am. Bull.*, 96, 793 - 812, 1985.

Weldon, R. J., and E. D. Humphreys, A Kinematic Model of Southern California, *Tectonics*, 5, 33 - 48, 1986.

Wells, D. L., K. J. Coppersmith, New empirical relationships among magnitude, rupture length, rupture width, rupture area, and surface displacement, *Bull. Seis. Soc. Am.*, 84, 974 - 1002, 1994.

Working Group on California Earthquake Probabilities, Seismic Hazards in Southern California: Probable Earthquakes, 1994 to 2024, *Bull. Seis. Soc. Am.*, 85 (2), 379-439, 1995.

Yule, Doug, and Sieh, Kerry, The paleoseismic record at Burro Flats; evidence for a 300-year average recurrence for large earthquakes on the San Andreas Fault in San Geronio Pass, Southern California, *Abstracts with Programs – Geol. Soc. Am.*, 33, 31, 2000.



## **Appendix A**

### **Software philosophy, design and some interesting algorithms**

#### **1. Introduction**

The block modeling results (Chapter 1) rely heavily on a rather elaborate collection of codes. The purpose of this appendix is to provide some documentation of the critical geometry management algorithms. There is only the briefest mention of most of these algorithms in the block modeling section. Despite such short shrift in the main section these problems and algorithms are extremely interesting. In total, the geometry management issue can be boiled down to one declarative statement; “Make a block model”. The obvious first step is to draw some set of block boundaries. We also need to identify the blocks on either side of each fault segment. Simple as it sounds there are some wonderful challenges involved. Hopefully there’s enough information here to clarify some of the more complicated algorithms that lie at the heart of the block modeling code. A user need not know how any of this works in order to successfully run the code. Most current users are unaware that these calculations even exist!

## 2. Lineage and early work

At least two MIT Ph. D. theses prior to this one included work on aspects related to block modeling. *Bennett* (1995) estimated strike slip rates on the San Andreas, San Jacinto and Elsinore faults from geodetic data with a block model that did not satisfy path integral constraints, as fault normal motion (e.g., shortening) was ignored. *Souter* (1998) built a southern California model that obeyed path integral constraints and used it to predict an interseismic velocity field from *a priori* fault slip rate estimates estimated from an inversion of select geologic slip rate estimates for block motions.

*Souter's* code was primarily GUI driven with external calls to executables for the elastic dislocation (*Okada*, 1985) calculations. I inherited this code when I came to MIT. Using the code as written proved untenable, as the GUI required more graphics power than was readily available. So I set about rewriting the code without this front end. Well of course in MATLAB a GUI is not so much a front end as the heart of your program. Data are stored not in the workspace but in figure handles. In this case flow control ran through the same functions that generated the GUI. Thus rewriting the code GUI-free was somewhat more involved than just ripping out some plotting calls. Eventually the whole code was rewritten to work from the command line with only the I/O routines and dislocation calculation remaining from *Souter's* (1998) work. Once this had been done I added the ability to invert geodetic data for block motions. Previously the code had estimated block motions from *a priori* fault slip rate estimates, generated a forward model of interseismic deformation and then compared that with the observations. Further functionality was added to allow for the batch processing of different models in order to

map out parameter space as a function of the nonlinear parameters (i.e., locking depths). Three papers emerged using some form of this code (*McClusky et al.*, 2001, *Meade and Hager*, 2001, *Meade et al.*, 2002). At this point, the real work began.

As it was, the block modeling code worked just fine, but not well. Setting up a model was incredibly time intensive and difficult. Specifically, fault segments had to be hand labeled according to the internal names of their bounding blocks. All fault and station locations were specified in a projected coordinate system. This proved extremely unnatural, especially when working at large scales. Further, all of the stations had to be hand assigned to blocks. This was a time consuming and error prone procedure. All of this meant that things worked just fine if you had just one velocity field, one fault geometry, and a small study area, but this was a severe limitation.

However, these were all critical failings in terms of the Southern California project that I intended to pursue. This project would require us to test hundreds of different fault system geometry configurations with a large number of velocity fields. While it may have been possible to rework my version of the block modeling code, this seemed to be a poor choice given the design limitations that I had built in previously. I wasn't exactly sure of how I wanted to put it all together so I decided to just give myself a ton of options. I followed a MATLAB tradition and started building a toolbox.

### **3. Philosophy**

When I set about writing a toolbox, I had two things in mind: natural formulations and generality. The latter is a great goal, yet I fell into the trap that so many do. The first

iteration of the code was too closed and the one that followed was too general. This means that, while the current version is quite general, there is also an awful lot of baggage that is not necessary for the majority of common applications.

By natural formulations, I mean that a function or script is written in such a way that the user (mostly me) can work with data in its natural form. For GPS data, this meant specifying station coordinates in longitude and latitude, as well as velocities in east, north and up (ENU). For fault segments, this meant specifying endpoints in longitude and latitude. This may seem trivial yet it was quite a conceptual leap at the time and I know of no other implementation of *Okada's* (1985) dislocation equations with this ease of use. Another example of natural use, more specific to block modeling, is the model geometry specification. Stations must be assigned to the appropriate block, but there is no reason for a user to ever have to do this. Fault labeling is another example of a process that is best left to a clever algorithm.

In the end I hoped that I would be able to build a toolbox for modeling crustal deformation that would allow me to build my block model application by just stringing together a series of function calls. While it wasn't exactly that simple in practice, it turned out to be remarkably close. Thus the current version of the block modeling software is very readable and extensible from the top on down. It also eliminates many complications that most modelers presumably are uninterested in, as they do not bear directly on the physics of the problem. This toolbox and the block model code could be a useful addition to the corpus of crustal deformation modeling software.



#### 4. Block model software structure

The rather unglamorous name of the block modeling software is `blocks_sp1`. This is really just the base name for a number scripts that link together calls to the crustal deformation toolbox. `blocks_sp1_WL2` does the weighted least squares estimate (WL2) of block motions and fault slip rates and `blocks_sp1_apriori` estimates velocities from a given set of block motion Euler poles. Both scripts use the same set of input files with different parameters. The flow control for the inverse problem (`blocks_sp1_WL2`) is linear (shown schematically in Figure A.1). For the *a priori* case the structure is quite similar. Both of the `blocks_sp1` scripts are easy to read once one has a general idea of the structure.

#### 5. Some interesting algorithms

All right, so that sounds great but how do you do it? I'll leave out the most of the detail but I will address a few of the concepts behind the some of the more interesting algorithms. Most of these fall into the category of bookkeeping. I'll detail three such algorithms. The block closure algorithm calculates closed block polygons from collections of fault segments. The blocks labeling algorithm determines which blocks are to the east and west of each fault segment in a consistent manner. A station assignment algorithm takes labeled fault information and uses it to determine which stations are on which blocks. Finally, I present the details of an interesting front end to *Okada's* (1985) dislocation calculation. The significant advance here is that the user can work in longitude and latitude space without having to consider the details of the necessary map

projections. This process is automated in a manner that minimizes the spatial distortion due to the map projection.

### 5.1. Block closure and labeling

Without a doubt, the most interesting and obscure part of this effort was the block geometry management. That is, how do we relate the faults to the blocks that they bound? One way would be to hand label each fault segment with the block names on either side. With lots of faults, this was at best a complicated, tiresome, time consuming and error prone procedure. We proved this after managing to write three papers (*McClusky et al.*, 2001, *Meade and Hager* 2001, *Meade et al.*, 2002). In fact, this was the time limiting factor that minimized the number fault system geometry variations we could study.

The key to automating this process is the separation of block information from fault system geometry information. In practical terms, this means that a user should be able to specify the fault system geometry without indicating what blocks bound each fault. However, we still need that information. We refer to this as the “block closure problem”. The first step in this procedure is to ensure that there are no “hanging segments”. These fault segments have endpoints that do not meet up with any other fault segment. This algorithm also must produce two things. First it must determine how many blocks there are and second it must determine the unique labels for the blocks next to each fault. The basic block closure algorithm is outlined in figure A.2. This algorithm

results in the calculation of the total number of blocks, a list of the faults that bound each block and the labels of the blocks on either side of each fault.

### **5.2. Fault labeling and east - west determination**

Now that we know which blocks bound each fault segment we now have to determine which blocks are on the east and west sides of each segments. This is necessary to insure sign consistency through the elastic dislocation calculations. As written, the block closure algorithm does not give us this information. It tells us which blocks bound each fault segment but not which side they are on. To do this we use a very simple algorithm shown in figure A.3. From each fault midpoint, we introduce a perturbed location just to the east. We then use an `inpolygon` test to determine if the perturbed point is in one of the bounding blocks. The block labels are known at this point from the block closure algorithm. If the perturbed point is in the block we are testing then that block is to the east of the segment, if not to the west.

### **5.3. Station labeling**

Once all of the blocks have been identified, we must also determine which GPS station is on which block. This is necessary for the rotation calculation. This algorithm is straightforward (figure A.4) and relies mostly on a call to MATLAB's `inpolygon` routine. This function takes polygon vertices and returns logicals that indicate whether or not a point is inside, outside or on the polygon boundaries. The only complication is that we are working on a sphere. This means that for long fault segments there is substantial

difference between the rhumb line and great circle path (GCP) between the two endpoints. In order to best represent the implied paths between two points we've had to add an extra step where we chop long segments into smaller pieces along the great circle path. The rest of the algorithm is a straightforward loop over all of the blocks. For each block we test to see which stations are on it. Once we loop over all blocks, any stations that have not yet been labeled are assigned to the exterior block. This is very convenient for large problems where one might want to have a block that represents the "rest of the world".

#### **5.4. Okada with an automatic optimal map projection**

The purpose of this algorithm is to allow the user to carry out a dislocation calculation (*Okada, 1985*) using geodetic data in ENU coordinates with fault and station coordinates specified in longitude and latitude. *Okada's* (1985) formulation is only for a planar elastic halfspace. We know of no equivalent formulation for the deformation associated with an arbitrarily inclined finite source on a sphere. Thus, one typically chooses a map projection for a study area and then projects both the fault geometry and the station coordinates. Over large areas, this is problematic as either the areal or angular distortion grows and the projection ceases to be accurate. Over an area the size of Southern California the distortion is less than 1% in distance. Larger areas present a substantial difficulty because the distortion due to any map projection is significant. It is important to minimize any spatial distortion around faults to ensure the accuracy of the elastic dislocation contribution. In order to deal with this challenge we decided to avoid

trying to determine the best projection for a given study area and instead use multiple map projections. Elastic deformation is only localized around fault zones; therefore these are the areas that require the most accurate projections. For each fault zone, we divide the fault, if necessary, into even smaller sections (e.g., 10 – 100 km). The elastic calculation is done for each sub-fault, and then all of the velocity contributions are summed. We use a separate oblique Mercator map projection for each fault. This projection is locally tangent to the GCP between the two fault endpoints. After the dislocation calculation is carried out in planar space, we rotate the velocities to account for the strike of the fault where they are interpreted as east, north and up. The velocity vectors do not need any further “unprojecting” (see `vinvtran` in the MATLAB Mapping toolbox) due to the fact the Mercator projection is angle preserving (conformal). This algorithm (figure A.5) is useful for three reasons: 1) a user can simply work with station and fault coordinates in longitude and latitude space, 2) spatial distortion is minimized for every fault segment, 3) the block model can be extended to arbitrarily large areas.

**References**

Bennett, R. A. Global Positioning System Measurements of Crustal Deformation Across the Pacific-North America Plate Boundary in Southern California and Northern Baja, Mexico, *Ph. D. Dissertation*, Massachusetts Institute of Technology, 1995.

McClusky, S. C., S. C. Bjornstad, B. H. Hager, R. W. King, B. J. Meade, M. M. Miller, F. C. Monastero, and B. J. Souter, Present Day Kinematics of the Eastern California Shear Zone from a Geodetically Constrained Block Model, *Geophys. Res. Lett.*, 28, 3339 - 3372, 2001.

Meade, B. J., B. H. Hager, S. C. McClusky, R. E. Reilinger, S. Ergintav, O. Lenk, A. Barka, and H. Ozener, Estimates of Seismic Potential in the Marmara Sea Region from Block Models Secular Deformation Constrained by Global Positioning System Measurements, *Bull. Seis. Soc. Am.*, 92, 208 - 215, 2002.

Meade, B. J. and B. H. Hager, The current distribution of deformation in the Western Tien Shan from block models constrained by geodetic data, *Geologia i Geofizika (Russian Geology and Geophysics)*, 42, 1622-1633, 2001,

Okada, Y. Surface deformation due to shear and tensile faults in a half space, *Bull. Seis. Soc. Am.*, 75, 1135-1154, 1985.

Souter, B. J., Comparisons of geological models to GPS observations in Southern California, *Ph. D. Dissertation*, Massachusetts Institute of Technology, 1998.

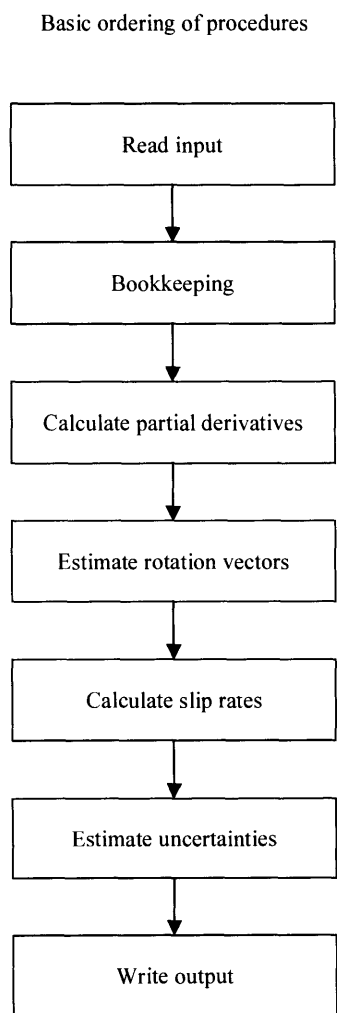


**Figure A.1.** blocks\_sp1\_WL2 flow control

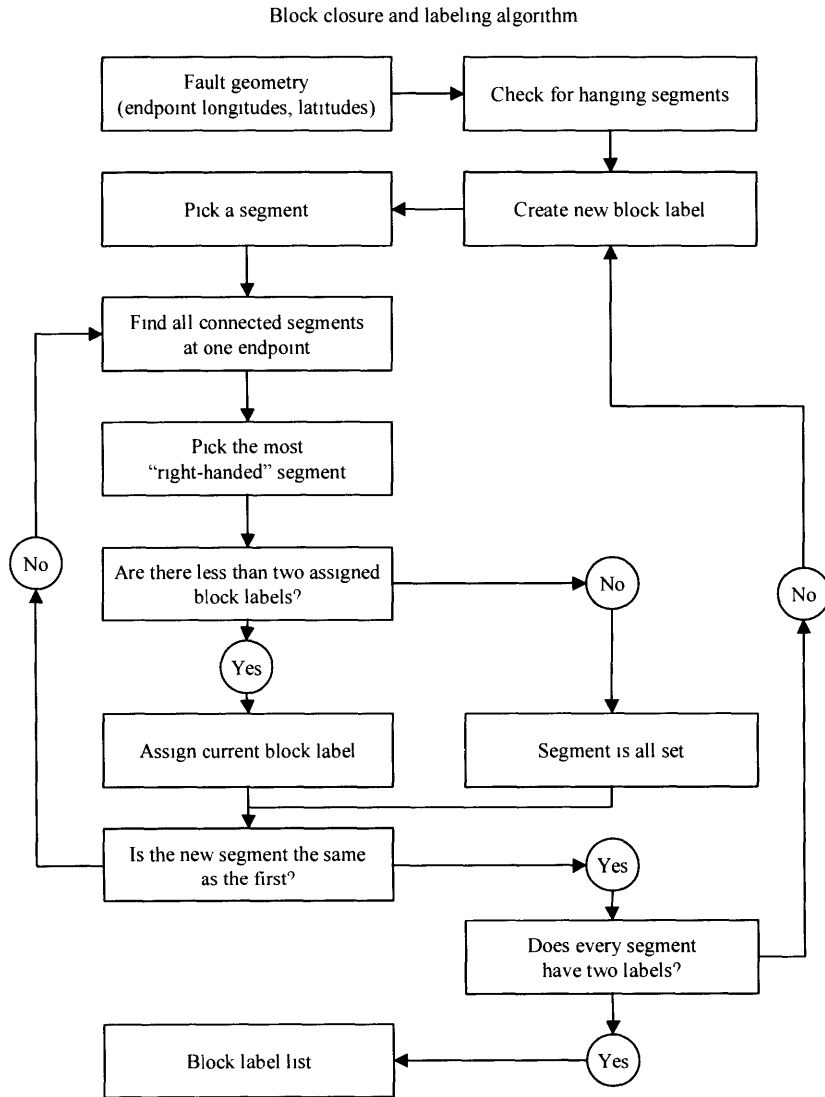
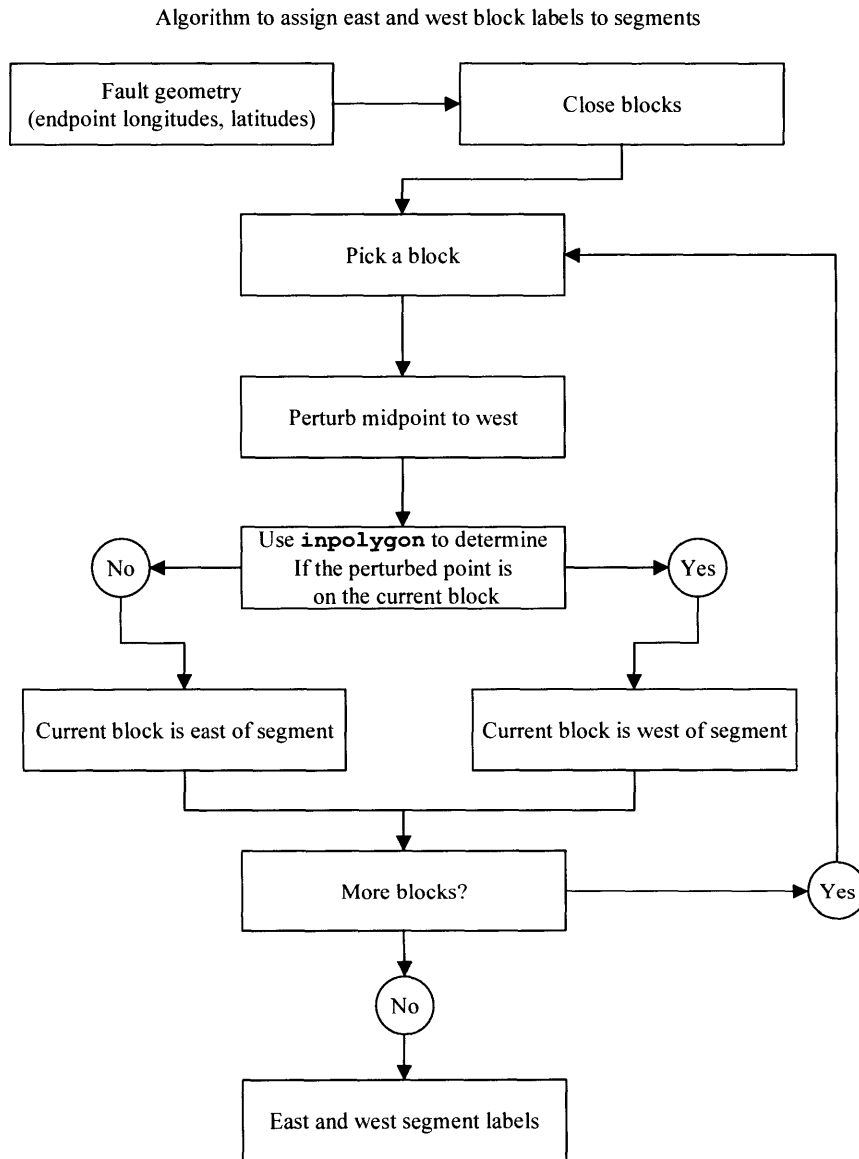
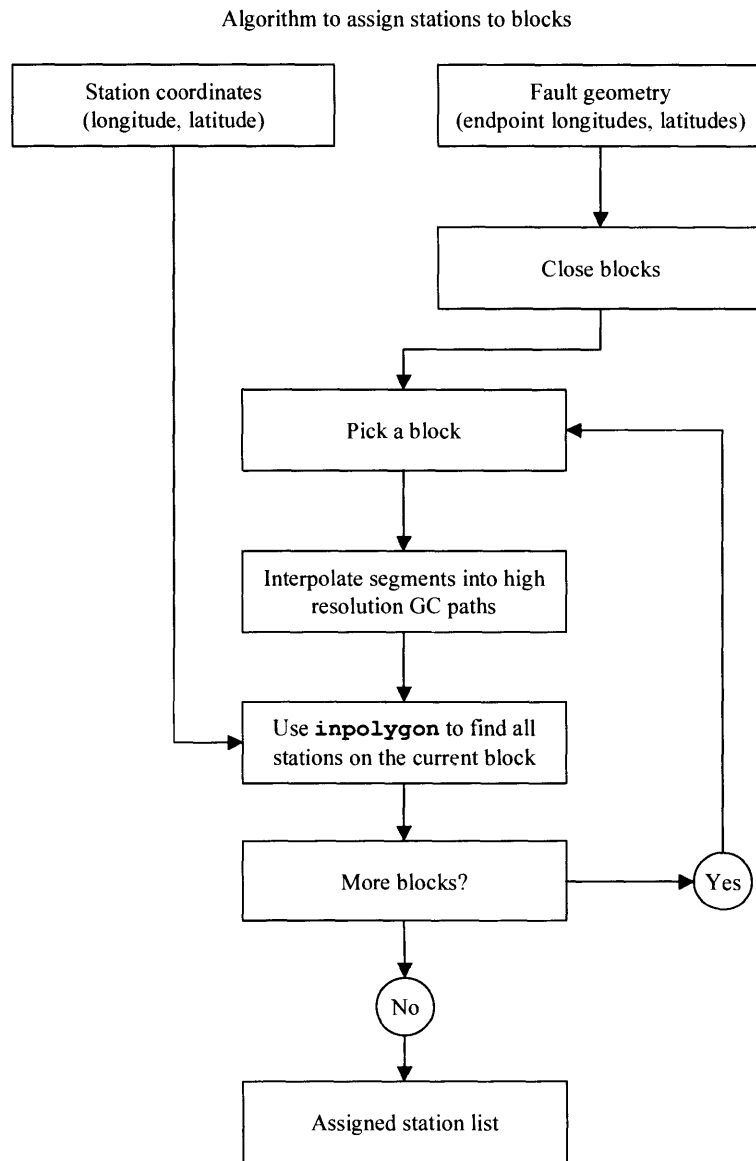


Figure A.2. Block closure algorithm





**Figure A.3.** East-west label determination



**Figure A.4. Station assignment algorithm**

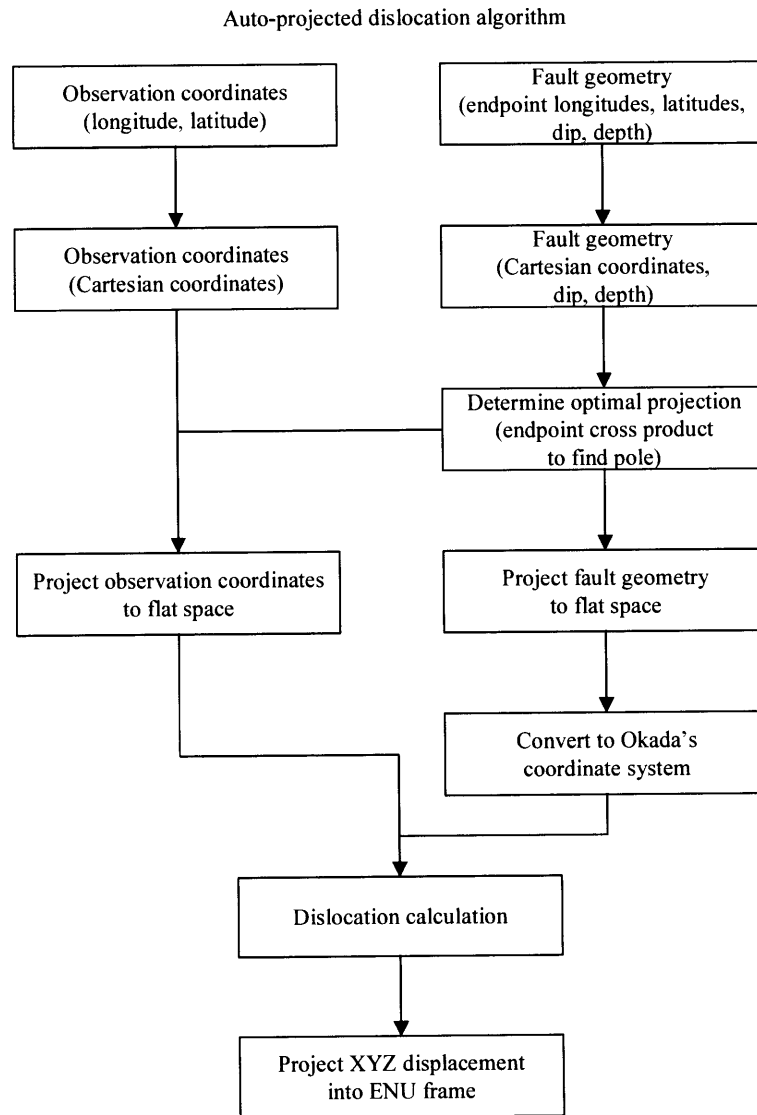


**Figure A.5.** Auto-projected dislocation algorithm